TN TDOT Department of Transportation

U.S. Department of Transportation
Federal Highway Administration

Evaluation of Backfill Aggregate Properties

Research Final Report from The University of Tennessee-Knoxville | Khalid A. Alshibli, Mohamed Elkenawi | December 20, 2025

Sponsored by Tennessee Department of Strategic Planning, Research & Innovation Division

Research Office & Federal Highway Administration

THE UNIVERSITY OF TENNESSEE KNOXVILLE

DISCLAIMER

This research was funded by the Tennessee Department of Transportation and the Federal Highway Administration through the State Planning and Research Program (RES #2024-05: Evaluation of Backfill Aggregate Properties).

Technical Report Documentation Page

1. Report No.	2. Government Accession No.	3. Recipient's Catalog No.
RES2024-05		
4. Title and Subtitle *Evaluation of Backfill Aggregate Properties*		5. Report Date March, 2026 6. Performing Organization Code
7. Author(s) Khalid A. Alshibli, Mohamed Elkenawi		8. Performing Organization Report No.
9. Performing Organization Name and Address University of Tennessee 315 John D. Tickle Building Knoxville, TN, 37996-2313		10. Work Unit No. (TRAIS) 11. Contract or Grant No. 74736
12. Sponsoring Agency Name and Address Tennessee Department of Transportation James K. Polk Bldg, 3rd Floor 505 Deaderick St., Nashville, TN 37243		13. Type of Report and Period Covered Final Report (8/1/23-3/31/26) 14. Sponsoring Agency Code
15. Supplementary Notes		

16. Abstract

Open-graded granular backfill materials are widely used as retaining wall backfill due to their high shear strength, high permeability, ease to handle, and compaction characteristics. However, the current Tennessee Department of Transportation (TDOT) provisions assume a conservative angle of internal friction for backfill materials. The objective of this project was to assess the influence of mineralogy, morphology, and aggregate type on the density and shear strength of fill aggregates from a wide range of supply sources throughout Tennessee. A comprehensive testing program was conducted employing a special large-scale direct shear apparatus to test twenty-six coarse aggregates conforming to the #57 stone gradation, including crushed limestone and river gravel at normal stresses of 35, 70, 105, and 140 kPa and relative densities of 30% and 80%. Particle morphology was quantified using 3D X-ray micro-computed tomography (μCT), enabling the extraction of statistically robust descriptors of roundness, form, and sphericity. The results demonstrate that specific morphology parameters, particularly sphericity location, roundness scale, and form scale, have a measurable and consistent influence on the peak friction angle (ϕ_p), critical state friction angle (ϕ_{cs}), and dilatancy angle (ψ), regardless of the particle size and material origin (mineralogy). Incorporating the 3D morphological indices into linear and nonlinear regression models significantly improved the prediction of ϕ_p, ϕ_{cs}, and ψ across a broad range of granular materials. This report recommends new friction and dilatancy angles for backfill materials depending on the height of the retaining wall and proposes revising current TDOT SP624 provisions for backfill materials compaction and subsequently the backfill zone behind the retaining walls. The percentage reduction in the volume of backfill aggregates for the proposed guidelines is between 24% and 66% depending on the height of the wall and the thickness of its footing.

17. Key Words	18. Distribution Statement		
SHEAR STRENGTH, AGGREGATES, FRICTION ANGLE, WALL BACKFILL, RETAINING WALLS, DIRECT SHEAR.			
19. Security Classif. (of this report)	20. Security Classif. (of this page)	21. No. of Pages	22. Price
Unclassified	Unclassified	94	

Acknowledgement

This research was funded by the State Research and Planning (SPR) Program through the Tennessee Department of Transportation (TDOT) and the Federal Highway Administration (FHWA), State Project RES2024-05. The report reflects the views of the author(s), not those of TDOT or FHWA. Funding for the micro-computed tomography (μCT) scans of aggregates was received from the European Union's Horizon Europe programme under grant agreement No 101131765 (EXCITE2), for Transnational Access at the Centre for X-ray Tomography (UGCT) of Ghent University (BOF.COR.2022.0008) and IOF, project FaCT F2021/IOF-Equip/021.

Executive Summary

Open-graded aggregates are widely used in many civil engineering applications, including backfill material behind retaining walls, embankments, slopes, and highway base material. Current TDOT SP624 provisions assume a very restrictive angle of internal friction for select backfill aggregates, which results in a conservative design. This project characterized the shear strength of #57 stone for samples collected from twenty-six quarries including crushed limestone and river gravel from four regions across Tennessee, as well as adjacent areas along the state borders (Region 5). A comprehensive experimental program was conducted on samples of #57 crushed limestone and river gravel utilizing a large direct shear apparatus to investigate their shear strength behavior under varying loose and dense states and normal stress levels.

The morphological characteristics of the tested aggregates were quantified using 3D X-ray micro-computed tomography (μCT), which enabled accurate measurement of particle shape descriptors. The resulting morphology indices were statistically characterized by fitting them to appropriate probability density functions (PDFs) and the extracted statistical parameters were subsequently used to develop linear and nonlinear regression models.

The finite element (FE) method was employed to identify the failure surface of active aggregate mass behind a cantilever retaining wall. Additionally, a concrete retaining wall was instrumented with four earth pressure cells, a deformation meter, and a tiltmeter to provide field measurements of earth pressure.

1.1 Key Findings

The main findings of the paper can be summarized as follows:

- The mineralogical composition of granular materials has a relatively limited influence on both peak friction angle (ϕ_p) and critical state friction angle (ϕ_{cs}) whereas particle angularity plays a more significant role in governing these shear strength parameters. Although quartz is inherently stiffer and stronger than calcite and dolomite with respect to individual mineral properties, the crushed limestone, composed primarily of calcite and dolomite, exhibited higher shear strength than the more rounded river gravel. This behavior is attributed to the higher angularity of the crushed limestone particles, which enhances interlocking and resistance to shear deformation.
- The morphology statistical parameters, especially the scale parameter of the generalized extreme value (GEV) distribution (σ_R), shape parameter of the Gamma distribution (κ), and the location parameter of GEV distribution (μ_1) have a significant influence on the ϕ_p, ϕ_{cs}, ψ for aggregates.
- Simplified, yet powerful predictive models are proposed for estimating ϕ_p, ϕ_{CS}, ψ for aggregates based on particle morphology, relative density (D_r), and normal stress. These models can serve as valuable inputs for constitutive models or practice, enabling the accurate prediction of the shear strength behavior of granular materials. By leveraging these models, it becomes possible to reduce the need for extensive experimental testing across a range of confining pressures and densities, thereby streamlining the geotechnical characterization process.

1.2 Key Recommendations

- Several gaps were identified in Section B of SP624: “Cast-In-Place (CIP) Concrete Cantilever and Counterfort Retaining Walls”. New guidelines and provisions are proposed within this report. The updated provisions address compaction activities for these wall types, clearly defining compaction procedures and lift thicknesses for both loaded and unloaded zones.
- The report recommends adopting new values of the critical state friction angle and dilatancy angle of crushed limestone and river gravel as a function of wall height, outside of the restrictive angles previously seen.
- The Finite element (FE) results demonstrated that the 1:1 slope of the backfill material behind cast-in-place cantilever concrete wall according to the current TDOT guidelines is very conservative and a steeper slope of 0.75H:1V will achieve a safe and economical design and complies with OSHA requirements (Subpart P-Appendix B-(OSHA)). For in situ materials classified as intermediate geomaterials, adopting steeper slopes eliminates the need for costly excavation of stable and hard geomaterial.
- New guidelines for estimating the required volume of backfill material behind the retaining wall are proposed, which will result in substantial savings in aggregates’ volume, construction time, and cost.

Table of Contents

List of Tables

List of Figures

Glossary of Key Terms and Acronyms

TDOT	Tennessee Department of Transportation
UTK	University of Tennessee-Knoxville
OGA	Open-graded aggregate
LSDS	Large-scale direct shear
LTX	Large triaxial compression
σ_3	Confining pressure
σ_n	Normal stress
D_r	Relative density
ϕ	Angle of internal friction
ϕ_o	Secant angle of internal friction
τ_f	Shear strength
δ	Wall-soil friction angle
F_a	Resultant active earth pressure force
USCS	Unified soil classification system
XRD	X-ray diffraction
XRF	X-ray fluorescence
MPE	Malvern panalytical epsilon 1
IAMM	Institute for Advanced Materials & Manufacturing
ICDD	International Center for Diffraction Data
GOF	Goodness of fit
C_c	Coefficient of curvature
C_u	Uniformity coefficient
G_s	Specific gravity of solids
e_{max}	Maximum void ratio
e_{min}	Minimum void ratio
d_{50}	Mean particle size
µCT	3D X-ray micro-computed tomography
UGCT	Ghent university, belgium
I_{sph}	Sphericity index
I_R	Roundness index
F	Form
d_S	Shortest length of a particle
d_I	Intermediate length of a particle
d_L	Longest length of a particle
Vs	Volume of sphere with a diameter equal to d_S
V_p	Actual volume of a particle
A_p	Actual surface area of a particle
ϕ_p	Peak friction angle
ϕ_{cs}	Critical state friction angle
ψ	Dilatancy angle
AIC	Akaike information criterion
PDF	Probability density function

GEV	Generalized extreme value
ξ	Shape parameter of GEV distribution
μ_1	Location parameter of GEV distribution
σ_1	Scale parameter of GEV distribution
κ	Shape parameter of Gamma distribution
θ	Scale parameter of Gamma distribution
μ_2	Location parameter of
GA	Genetic algorithm
MSE	Mean squared error
k	Optimal regularization parameter for ridge regression
R^2	Coefficient of determination
FEM	The finite element method
MC	Mohr-Coulomb constitutive model
α	Angle of the active failure wedge

Chapter 1 Review of Literature Studies and Current Practices

1.1 Problem Description

For retaining walls construction, the Tennessee Department of Transportation (TDOT) often allows contractors to excavate behind the retaining wall and replace the existing in-situ soils with "a select backfill" that has a higher friction angle (ϕ) and permeability, which reduces the active earth pressure on the wall. TDOT currently requires that the active zone be excavated at 45° (1:1 slope) from two feet behind the heel of the wall or reinforced soil zone up to the finished grade. Although a 1:1 slope is considered an acceptable temporary slope for average soils in TN, it can be a very conservative approach, and costly, especially when a rock formation crosses the 1:1 slope. According to TDOT retaining wall provisions, a maximum friction angle of 34° can be assumed for the select backfill aggregates that are not tested but meet the requirements stated in Special Provision 624 regarding retaining walls. For select backfill aggregates that are tested independently, TDOT sets the maximum friction angle (ϕ) to a value of 40° if demonstrated by the test results. Both values are conservative, as the independent test results often exceed both stated ϕ valuesThe shear strength of open-graded aggregate (OGA) is represented by a ϕ value, which is used to calculate the active earth pressure on retaining walls. The shear behavior of OGA is influenced by many factors such as mineralogy, morphology (roundness, sphericity, and surface texture), gradation, relative density (D_r), and fabric (particle-to-particle association). There are different laboratory tests commonly used to measure ϕ of OGA, where the large-scale direct shear apparatus (LSDS), large triaxial compression (LTX) apparatus, and prismatic wedge are the most common procedures. The value of ϕ varies depending on the type of test (loading condition), strain rate, and the protocol of the test procedure.

1.2 Factors affecting the angle of internal friction (ϕ)

This section summarizes the literature related to the factors that affect the value of ϕ as well as the common tests used to measure ϕ. Nicks et al. (2023) investigated five different geologic conditions and mineralogy (i.e., basalt, diabase, granite-gneiss, limestone, and siltstone) for samples with similar gradation. Based on the results of six different laboratories, mineralogy showed no influence the shear strength of OGA and aggregate gradation affects the shear strength of OGA. Nicks et al. (2015); Varadarajan et al. (2003); Honkanadavar and Sharma (2014) reported that ϕ decreases as aggregate size decreases. Recently, Nicks et al. (2023) reported that aggregate grain size has a minor effect on the measured ϕ. Indraratna et al. (1998) found that aggregates with a narrow gradation exhibit a faster decline in ϕ as compared to rockfill materials with a broader gradation, and well-graded aggregates have a denser packing state which yields larger values of ϕ for similar confining pressures (σ_3) or normal stress (σ_n).

The morphology of OGA is another important parameter to consider. Generally, OGA with angular particles has a higher value of ϕ when compared with OGA composed of rounded particles (Varadarajan et al. 2003). Additionally, the degree of saturation has a minor effect on the values of ϕ (Nicks 2013; Yamaguchi et al. 2008). However, relative density (D_r) is one of the most crucial

parameters that affect the shear strength of OGA. Honkanadavar and Sharma (2014) found a slight rise in ϕ with the increase in aggregate density. Based on the LSDS results reported by Nicks (2013), ϕ grew by an average value of 23% due to increasing D_r from 30% to 95%. Furthermore, ϕ increased by an average value of 16% when D_r icreased from 30% to 95% based on the results of LTX.

Finally, the loading condition (i.e., direct shear, plane strain, or triaxial) influences the shear strength of aggregate. Indraratna et al. (1998) investigated different load conditions that affected the value of ϕ based on the results of the large triaxial apparatus. The tests were performed on two different aggregate gradations at multiple σ_3 that ranged from 1 kPa to 240 kPa. The results showed that specimens displayed a significant radial strain expansion at low σ_3 (less than 30 kPa) and a positive correlation as the axial strain at the peak deviator stress increased as the σ_3 increased. Furthermore, ϕ decreased as σ_3 increased for LTX or as σ_n increased for the direct shear test. The reduction in ϕ was small when σ_3 is increased and the effects of particle sizes and their gradation were negligible.

1.3 Influence of Laboratory Procedure on the angle of internal friction (ϕ)

Direct shear and triaxial shear tests are considered the most common procedures to measure the strength of aggregates. According to the American Association of Testing Materials (ASTM) standards, the maximum particle sizes for direct shear and triaxial shear testing are 1/10th and 1/6th of the width or diameter of the specimen, respectively. For OGA, LSDS and LTX are widely used to avoid the problems of parallel gradation or scaling, which have a significant influence on test results. Nicks (2013) investigated five different aggregates with different gradations using LSDS with a shear box size of 12 in x 12 in x 8 in, LTX with a diameter of 6 in and a height of 12 in, and a D_r of 30% and 95%. The results displayed a variation in the values of ϕ based on the test loading condition. The ratio of the output from LSDS to LTX is 1.2 to 1.5. The dilatancy angle based on LSDS is larger than the one based on LTX. Finally, LTX yielded a small difference of about 7 degrees between loose and dense specimens for a constant volume friction angle based on the zero dilatancy angle, whereas the difference is about 10% to 20% for LSDS results. Another comparison is reported by Yamaguchi et al. (2008), who investigated two types of aggregates (dacite rock material (A) and crushed stone and crushed sand (B). Large specimens with a diameter of 300 mm and a height of 600 mm were tested using LTX apparatus under σ_3 of 49, 98, 196, and 294 kPa at D_r of 90%. The remaining specimens were tested using LSDS using a large shear box that measures 400 mm x 400 mm x 400 mm and a normal stress (σ_n) of 25, 49, 98, and 196 kPa. The specimens were tested at both saturated and air-dried conditions at D_r of 90% using a shear strain rate of 1.3 mm/min. Based upon the results of LTX, the secant friction angle (ϕ_o) values at each applied σ_n for air dried specimens are similar to ϕ_o values for saturated specimens at σ_3 of 49 kPa. At high σ_3, the values of ϕ_o for air-dried specimens are larger than ϕ_o values for saturated specimens by 3° to 5° for Material A and 1° to 2° for Material B. Contingent on the LSDS results, the ϕ value based on Mohr-Coulomb failure criterion for both Materials A and B is larger for air dried specimens than saturated specimens by nearly 3°. Finally, Yamaguchi et al. (2008) proposed a statistical power relationship between σ_n and the shear strength at failure (τ_f) ($\tau_f = a\,\sigma_n{}^b$) for both LSDS and LTX results for saturated and air-dried specimens.

1.4 Parameters affecting the angle of internal friction (ϕ) based on LSDS results

A comparative study between six different laboratories was conducted to assess the influence of contrasting test parameters on ϕ using the direct shear test with a focus on the shear box shape, shear box mobility, the roughness of the base of the loading platen, and application of normal load. The study revealed that the shape of the shear box (circular, rectangular. or square), the method to apply and measure the normal load (dead weight, an airbag, hydraulic load, or a micro stepper motor), and the roughness of the base of the loading platen (smooth, grooved or textured) had no effect on the the variability of the results. Box mobility refers to the ability of the upper half of the shear box to move vertically, and Nicks et al. (2023) reported that LSDS systems with a fixed upper half of the shear box gave a higher ϕ than apparatuses with a mobile upper box.

1.5 Methods to calculate the angle of internal friction

There are different methods to calculate ϕ for the direct shear test experiments; they are as follows:

- Tangent friction angle and undrained shear strength (*c*) assuming a linear Mohr-Coulomb failure envelope (MC method).
- Residual tangent friction angle at 20% shear strain assuming a linear Mohr-Coulomb failure envelope.
- Constant volume friction angle assuming a zero dilatancy angle (ZDA) based on the critical state at ZDA = 0.
- Secant friction angle calculated for each applied σ_n (ϕ is calculated for each experiment).

Nicks (2013) reported that the linear MC method gives a value for apparent cohesion as it assumes a linear failure envelope with intercept (cohesion). There is a significant difference between the highest and lowest ϕ for the same aggregate for saturated and dry conditions. On the contrary, the ZDA method is much more suitable for calculating ϕ as it yields a narrow variation between the highest and lowest ϕ for the same aggregate. Nicks (2013) reported that the difference between MC and ZDA is less than 20%.

1.6 Theoretical models to estimate active earth pressure

The major concern in retaining walls analysis and design is to calculate the magnitude and distribution of both active and passive lateral earth pressures on the retaining wall. An overdesign of a retaining wall will result in a gross waste of construction materials, high cost, and longer construction time, whereas an underdesign will lead to a higher risk of failure. Rankine and Coulomb theories are the classical theories that have been widely accepted and used by designers. The Rankine active earth pressure theory, in spite of its major shortcomings, is vastly utilized in this area. It was developed on pure static analysis of soil mass, assuming perfect plastic failure without consideration of the soil volume change. Both Coulomb and Rankine theories assume a triangular distribution of active earth pressure. However, many experimental studies reported that the distribution of active earth pressure behind a rough yielding wall is nonlinear, and is dependant on

the mode of movement of the wall (i.e., rotation about the top, rotation about the base, or translation (Fang and Ishibashi 1986; Matsuo et al. 1978; Paik and Salgado 2003). The nonlinearity of the active earth pressure is caused by soil arching (Handy 1985). Other factors such as fill material friction angle, greatly influences the coefficient active earth pressure (K_a) even when using Rankine or Coulomb theories as illustrated in Figure 1-1 where Rankine K_a decreases from 0.282 to 0.147 (about 50% reduction) when ϕ increases from 34° to 48°, respectively.

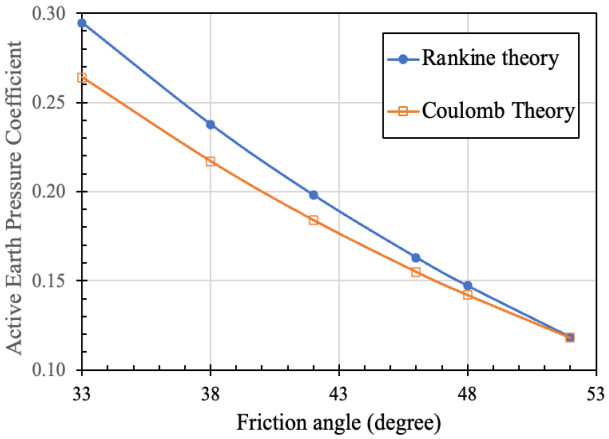

Figure 1-1. Influence of friction angle on coefficient of active earth pressure.

Various theories have been used to estimate the lateral earth pressure. Coulomb's theory. which was proposed in 1776, applies the limit equilibrium principle and assumes a planar failure surface. It defines a soil wedge and assumes the soil as a granular material (i.e., it does not account for the cohesion effect) that applies lateral pressure on a wall and applies equilibrium equations to the wedge. Coulomb's theory offers a straightforward equation for the lateral earth pressure, derived from the soil's angle of internal friction (Bowles 1988; Coulomb 1773). Rankine's theory (1857) is considered to be an extension of Coulomb's theory based upon the limiting equilibrium approach with an assumed planar failure surface. Consequently, Rankine theory then takes into consideration the effect of soil cohesion and wall inclination and it offers simple equations to determine both the active and passive earth pressures (Bowles 1988; Das 2011). Terzaghi (1936) presented a theory that adopts the principle of effective stress and takes into consideration the influence of soil consolidation on earth pressure. Terzaghi assumed a logarithmic failure surface and proposed equations to determine both active, passive, and at-rest earth pressures. Dubrova (1963) introduced her theory by considering the arching influence on the distribution of active earth pressure, and assumed that the wall rotates about its mid-height. Due to this, Dubrova's method can be used only for a level ground surface, and it is not appropriate for an inclined group surface.

Wang (2000) presented a new model based on Coulomb's concept that defines the unit active earth pressure and the limiting equilibrium of the forces on an element of a sliding wedge, as well as assuming that the active earth pressure has curvilinear distribution. The resultant active earth pressure calculated by Wang (2000) equals the resultant active earth pressure force (F_a) calculated by Coulomb (1773). The height of application of F_a calculated by Wang (2000) model depends on the value of the active lateral pressure and it is shown to be higher than that of the one calculated using Coulomb (1773). As a result, Paik and Salgado (2003) presented a new relationship to determine the active earth pressure distribution on a rigid retaining wall undergoing horizontal translation. To do so, they assumed a nonlinear distribution of active earth pressure on a translating retaining wall considering the arching effect. Paik and Salgado (2003) checked the accuracy of their model by comparing the active earth pressure predicted by their model with the results of an existing full-scale prototype. A new modified coefficient of active earth pressure was proposed by Paik and Salgado (2003) and an effective height of application of F_a are depending on ϕ and the

wall-soil friction angle (δ).

Goel and Patra (2008) proposed a new relationship to calculate the active earth pressure on a rigid retaining wall undergoing a horizontal translation. They assessed the influence of the geometry of the slip surface and the shape of the arch on the value of the coefficient of active earth pressure for a rigid retaining wall in a translation mode. Goel and Patra (2008) then considered two configurations of the geometry of critical failure surface and arch shape (a planar failure surface with a parabolic arch and a parabolic failure surface with a parabolic arch). Lastly, they compared their results with field results and those predicted by other theories. Thus, Goel and Patra (2008) concluded that the wall with a planar failure surface with a parabolic arch shape results are the closest to the field values.

Yap et al. (2012) compared the calculated values of the active earth pressure based on different theoretical solutions, such as (Coulomb 1773; Dubrova 1963; Paik and Salgado 2003; Terzaghi 1936; Wang 2000), with those obtained from finite element (FE) analysis using PLAXIS software. The FE model of the retaining wall has a height of 5 m that was fixed at the toe. The Mohr-Coulomb failure criterion was adopted as a form of differentiating between the elastic and plastic behavior when a permanent slip develops. The results of the comparison showed that the distribution of active earth pressure was non-linear and the maximum active lateral pressure failed to occur at the bottom of the wall which aligns with the findings of Goel and Patra (2008). Yap et al. (2012) found that the distribution of active earth pressure was linear at the upper half of the wall, which agrees with the results from all of the cited theoretical studies except those of Goel and Patra (2008). The distribution of the active earth pressure at the lower part of the retaining wall was nonlinear and matches Rankine's theory at a height percentage ranging from 50% to 80% of the wall height. After 80% of the wall height, the distribution of active earth pressure becomes parabolic extending to the bottom of the wall, and matches Rankine's theory, whereas all other theories instead underestimated the value of the active pressure. In addition, PLAXIS FE analysis demonstrated that the compatibility of Rankine's active earth pressure magnitude with FE has affirmed FE effectiveness in predicting the behavior of retaining walls. Finally, the Wang (2000) model yielded the closest results to the FE solution for the maximum active earth pressure, within a height range of 80% to 90% of the wall height.

Yap et al. (2012) conducted a parametric study to investigate the effects of ϕ, soil unit weight (γ), wall height (H), and wall friction on the distribution of active earth pressure. The results of the study revealed the relationship between the two: as ϕ increases, the active pressure decreases, and the height of application of the maximum active earth pressure (towards the top of the wall) increases. Furthermore, the variation in the distribution of active earth pressure is less pronounced with changes in ϕ when ϕ exceeds 30^o in contrast to cases where ϕ is less than 30^o as observed in the study reported by Paik and Salgado (2003).

The influence of γ on earth pressure is clear where an increase in γ leads to a corresponding increase of both active and passive earth pressure values. The height of application of the maximum active earth pressure force does not change significantly in response to the change γ. While the height of the wall is considered a significant parameter, it does not significantly affect the shape of the distribution of the active earth pressure; however, it does have an effect on its magnitude. In the last bottom half meter of the wall height, the distribution of the active earth pressure has a parabolic shape and its magnitude increases as the wall height increases, which lines up with the

findings of Paik and Salgado (2003). Finally, the active earth pressure magnitude remains nearly constant with minimal deviation as wall friction increases at the upper zone of the wall. However, the increase in the wall friction leads to an increase in the maximum active earth pressure in the lower zone of the wall (0.5 m from the bottom of the wall) as well. Furthermore, the location of the maximum active earth pressure moves towards the top of the wall.

1.7 Field measurements of lateral earth pressure

There are few studies that have focused on field measurements of lateral earth pressure as a result of the challenges associated with acquiring the data from sensors for months, and due to environmental conditions, such as the effect of temperature on the accuracy of the readings of load cells. Matsuo et al. (1978) measured the distribution of lateral earth pressure on a large-scale 10 m concrete wall. Three different materials were used as backfills: silty sand with a maximum dry unit weight (γ) of 1940 kg/m^3 and ϕ of 27^o, and two slags (A, B) with different gradations produced from the process of iron manufacture. The slags had a maximum dry unit weight of 1900 kg/m^3 and ϕ of 40^o. The field readings included measurements at rest, active, and passive lateral earth pressures. The measurements continued for about 4 months, and one of the main results found from the Matsuo et al. (1978) study is that the active earth pressure condition was reached at a horizontal displacement of 6H/1000 to 8H/1000 for silty sand soil and 3H/1000 to 5H/1000 for the slags. The actual angle of wall friction was larger than the expected value before the test. Finally, Matsuo et al. (1978) recommended that the retaining wall should be designed assuming at rest condition in lieu of an active earth pressure condition.

Schulze et al. (1980) studied the active lateral earth pressure distribution on an 11 ft high cantilever wall supported by a 2-ft thick spread footing featuring a mid-base key. The backfill consisted of fine-grained silica sand, with an average unit weight (γ) of 117 pcf and a friction angle (ϕ) of 39^o. Field active earth pressure values were measured over a 380-day period, utilizing four pressure cells on the stem. The Culmann graphical solution based on Coulomb's theory, was employed to compute the theoretical active earth pressure. Schulze et al. (1980) reported that the field-measured active earth pressure exceeded the predicted theoretical pressure, calculated using the Culmann procedure, by approximately 3.5 times for both cases with and without a clay surcharge.

Coyle et al. (1974) investigated the lateral earth pressure distribution on a 16-ft cantilever wall supported by a spread footing with a thickness of 2.25 ft. Field earth pressure values were measured using four pressure cells on the back face of the stem during a 14-month observation period. The backfill comprised of fine sand with a small percentage of silt possessing a wet unit weight of 110 pcf, a moisture content of 0.204, and ϕ of 32^o. Wall movement due to rotation was meticulously recorded. The measured active earth pressure exhibited a consistent rate of increase of 0.40 psi/ft up to a depth of 7 ft, after which the active earth pressure increased significantly to 1.0 psi/ft. The majority of wall displacement occurred within the first month. The ratio between average field active pressure values and the theoretical active earth pressure based on Rankine's and Coulomb's theories was approximately 2.7 (Figure 1-2). Coyle et al. (1974) divided the retaining wall into three zones according to soil with pure active pressure within the top 7 ft, soil behavior transitioning between active and at-rest conditions from 7 ft to 13 ft, and behavior similar to at-rest conditions in the bottom 3 ft of the wall.

Patel and Deb (2020) studied the magnitude and stress distribution behind a small rigid retaining wall roatating about its base. Their laboratory wall model consists of a 10-mm-thick mild steel retaining wall with a height of 600 mm and a width of 1,400 mm. The length of the soil mass behind the wall was 670 mm. Particle Image Velocimetry (PIV); an image analysis technique, was employed to monitor soil movement, and full-field displacement vectors were calculated. Additionally, an analytical model was developed based on limiting equilibrium assuming a curvilinear failure surface based on PIV results and accounting for the arching phenomenon. A parametric study was then conducted to assess the influence of ϕ and δ on active earth pressure and the shape of the failure wedge. The backfill soil had a γ of 15.9 KN/m^3 and a D_r of 58%. Six strain-gauge-type soil pressure cells were strategically placed in the central zone of the model wall. ϕ and δ were measured by implementing a direct shear box and have values of 36° and 22°, respectively. Results from the experimental investigation of Patel and Deb (2020) revealed that the active stage is achieved at a wall rotation of 10×10^{-4} rad. Contrary to prior beliefs regarding hydrostatic pressure distribution, the test data negates this assumption and affirms the nonlinear distribution of active earth pressure. Notably, beyond 400 mm from the wall (67% of the wall height), soil deformation becomes nearly negligible, indicating the intersection of the failure wedge with the ground surface.

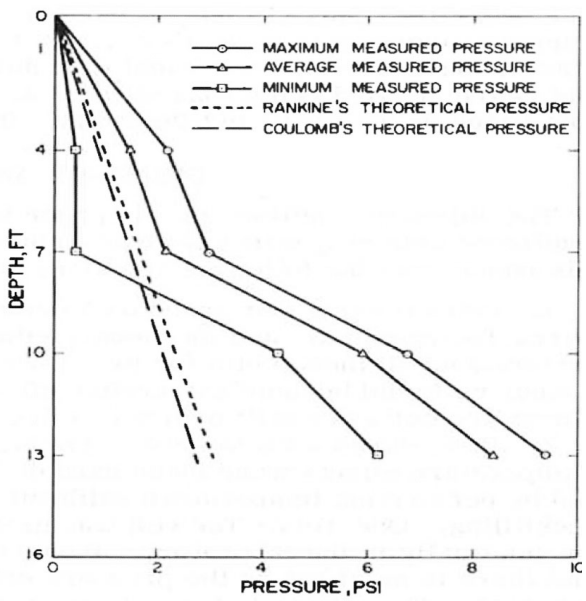

Figure 1-2. Field measuremens and theoretical active earth pressure distribution (Coyle et al. 1974).

The main outcomes of the parametric study of Patel and Deb (2020) were that the normalized active earth pressure decreases as ϕ increases and it decreases as δ increases until δ/ϕ is more than 0.67. Furthermore, the failure surface becomes almost linear and closely matches the predicted slip angle according to Coulomb's theory for a smooth wall. Patel and Deb (2020) recommended that a curvilinear failure surface is a good approximation for the potential failure surface for soil backfill with $\delta/\phi > 0.33$. Finally, the normalized active force shows a decreasing trend with the increase of the value of ϕ irrespective of δ/ϕ ratio.

Chapter 2 Material and Test Program

2.1 Material

2.1.1 Coarse granular materials

Twenty-six coarse granular aggregate samples (A01 to A26) were collected from different quarries across the State of Tennessee, USA, to represent different sources for the material within Tennessee. Six samples were collected from quarries within Region 1, Tennessee Department of Transportation (TDOT), eight samples from Region 2, six samples from Region 3, four samples from Region 4, and two samples from Region 5 (Tennessee Department of Transportation (TDOT)). Twenty-two samples are limestone aggregates, and the remaining four samples (A19, A22, A23, A24), are river gravel. Gravel is defined as the grain size ranging from 4.75 mm (U.S. Sieve #4) to 76.2 mm (3 inches), according to the Unified Soil Classification System (USCS), or from 2 mm to 76.2 mm (3 inches) according to the AASHTO classification system. Although the four gravel types are reported in this report and classified as river gravel, the particles' morphology alters where the particles of A19 and A23 are generally more angular, whereas A22 and A24 tend to be more rounded materials. Both the limestone aggregate and the river gravel were selected to meet the gradation specifications of #57 stone gradation, which are commonly used as backfill for retaining structures. Approximately one cubic yard of the material was collected from each quarry for laboratory testing. Appendix A presented photos of tested OGA.

2.1.2 Fine granular materials

Three different silica sands with varying morphologies (#1 Dry Glass Sand, GS#40 Columbia Sand, and F-35 Ottawa Sand) and glass beads were selected to represent the fine angular material, enriching the fidelity of the proposed statistical models to predict the shear strength of granular material.

2.1.3 Materials Mineralogy

The mineralogy of the gravel specimens was determined using X-ray fluorescence (XRF) analysis and powder X-ray diffraction (XRD). However, the mineralogy of the limestone aggregate was determined using XRD only. The XRF was conducted according to ASTM E1621 (2022) on gravel powder samples for element identification. The samples utilized for this study were prepared by grinding dry representative particles to a powder size smaller than the US sieve #200 (75 μm). The XRF tests were performed using the Malvern Panalytical Epsilon 1 (MPE) apparatus housed at the Institute for Advanced Materials & Manufacturing (IAMM) at the University of Tennessee-Knoxville (UTK). It is equipped with a silver (Ag) anode X-ray tube, making it particularly effective to excite heavier elements. This device can analyze a variety of sample types, including loose powders, pressed pellets, and solid chunks; however, it cannot detect elements lighter than fluorine (F). The powder specimens were filled in sample cups covered with a 3.6 μm Mylar film. The Mylar film prevented contamination and minimized interference, making it an ideal choice for fine powder analysis with high precision and reliability. MPE works by exciting atoms in the sample using high-energy X-rays, detecting the emitted secondary X-rays, and matching them to known element signatures for element identification.

The second analysis on coarse granular materials was performed using powder X-ray diffraction (XRD) according to (ASTM E3294), which is an effective method to identify unknown crystalline phases. The analysis involves comparing the positions and intensities of diffraction peaks within a library of known crystalline materials to identify the analyzed material composition. Furthermore, various phases within a sample can be identified and quantified. XRD is able to quantify the relative amounts of each phase, even when one of the phases is amorphous. The physical identification of the tested aggregates was conducted using powder X-ray diffraction at IAMM. The XRD data were acquired using a PANalytical EMPYREAN diffractometer in scan mode (reflection) with a reflection-transmission spinner sample stage. The X-ray source was a Copper (Cu) anode tube, operating at 45 kV and 40 mA, with a take-off angle of 6.0°. The wavelength components included K- (1.54 Å), K- (1.54 Å), and K- (1.39 Å), with a K- / K- ratio of 0.5. The incident beam path included a programmable divergence slit (0.5°), a fixed anti-scatter slit (1.52 mm), and a 0.04 rad Soller slit, while the diffracted beam path had a programmable anti-scatter slit (0.5°) and a PIXcel3D-Medipix3 1 × 1 detector in scanning mode, and a Nickel (Ni) beta filter (0.02 mm thick) was implemented. The scan covered a range of 5.013° to 89.992°, with a step size set by the instrument and a counting time of 46.665 seconds per step. The system was controlled using EMPYREAN v8.1j, and the data was recorded with Data Collector v6.1b. The mineralogical composition of each material was assessed through Rietveld refinement analysis of X-ray powder diffraction patterns. The Rietveld method involves generating a calculated diffraction pattern from the International Center for Diffraction Data (ICDD) databases and comparing it to the saved pattern from XRD analysis. Subsequently, phase quantification is performed automatically using default Rietveld refinement in High Score-Plus software. Quality measures such as the weighted profile R-value (Rwp) and goodness of fit (GOF) are additionally computed by the software. An Rwp value of less than 15% is considered a good pattern, and a GOF value of less than 2 is accepted as a good fit and refinement for complex patterns, which include three or more phases.

XRF analysis revealed that silicon (Si) is the dominant element present in the river gravel specimens only. In addition to silicon, a notable concentration of iron (Fe) was detected, along with trace amounts of aluminum (Al), nickel (Ni), and zinc (Zn). However, minor and insignificant quantities of sulfur (S), manganese (Mn), strontium (Sr), and zirconium (Zr) were also identified. Complementary X-ray diffraction (XRD) analysis confirmed that the primary mineralogical component of the four river gravel samples is silicon dioxide (quartz, SiO_2), comprising more than 90% of the mineral composition. The secondary mineral phase identified was iron (III) oxyhydroxide (goethite, FeO(OH)). Despite its presence, goethite occurred in small percentages that did not have an effect on the gravel's shear strength characteristics. However, in sample A24, goethite content was approximately 7%, which noticeably influenced the color of particles. Table 2-1 summarizes the percentage of each component of the river gravel. R_{wp} is weight profile R-value.

XRD results of limestone aggregate revealed that the three main components of aggregate minerology were Calcium Carbonate ($CaCo_3$), Calcium Magnesium Carbonate (Dolomite) ($CaMg(Co_3)_2$) and Silicon Oxide (Quartz) (SiO_2). Table 2-2 summarizes the percentage of each component of the limestone aggregate. The primary component with a percentage of more than 99% of #1 Dry Glass Sand, GS#40 Columbia Sand, and F-35 Ottawa Sand was Silicon dioxide (Quartz) (SiO_2), while the primary component of glass beads was soda-lime glass, derived from a mixture of silica, sodium oxide, and calcium oxide (Alshibli and Cil 2018)

Table 2-1. Mineralogy results of the tested gravel.

Material	Silicon Oxide (Quartz) (SiO_2)	Iron (III) oxyhydroxide (Goethite) (FeO(OH))	R_{wp}
A19	94.50%	5.50%	9.8797
A22	96.40%	3.60%	8.6412
A23	96.30%	3.70%	8.9776
A24	93.10%	6.90%	9.8797

Table 2-2. Mineralogy results of the tested limestone aggregate.

Material	Calcite Percentage (%) Calcium Carbonate ($CaCo_3$)	Dolomite Percentage (%) Calcium Magnesium Carbonate ($CaMg(Co_3)_2$)	Quartz Percentage (%) Silicon Oxide (SiO_2)	R_{wp}
A01	98.62	0.52	0.86	9.7772
A02	16.15	80.66	3.19	10.2017
A03	0.43	98.35	1.22	11.5382
A04	45.48	53.27	1.25	6.7896
A05	1.21	91.69	7.10	8.8684
A06	2.97	88.27	8.77	10.432
A07	74.04	25.26	0.70	7.2239
A08	51.20	44.73	4.07	7.0371
A09	71.99	26.06	1.95	8.3904
A10	63.44	32.78	3.77	7.4028
A11	61.49	35.93	2.58	9.4416
A12	71.67	21.33	7.00	7.0179
A13	39.7	57.20	3.10	6.7805
A14	65.12	31.35	3.53	7.2018
A15	7.20	82.66	10.14	9.2142
A16	78.06	17.31	4.62	8.3357
A17	69.71	22.35	7.94	7.9947
A18	15.77	50.02	34.21	7.6087
A20	79.39	14.96	5.64	7.4424
A21	86.43	8.51	5.06	9.9894
A25	57.09	36.09	6.82	6.5433
A26	85.10	12.40	2.50	8.3264

2.2 Testing Program

2.2.1 Routine tests

Sieve analysis was conducted in accordance with ASTM C136/C136M (2014), utilizing oven-dried samples and a full range of sieves (25 mm to 2.36 mm) to establish smooth gradation curves, which were then compared to the upper and lower limits of AASHTO M43 (2021) for #57 stone gradation specifications. The minimum and maximum dry unit weights, corresponding to maximum and minimum void ratios, were determined using ASTM D4254 (2016) (Method A), and ASTM 4253 (2006) (Method 1A) using a 14,159.1 cm³ cylindrical mold. Minimum density was obtained by loosely filling the mold using a short free fall, whereas maximum density was established by vibrating the mold at 60 Hz under a 14 kPa surcharge for 10 minutes and measuring the resulting specimen height. The specific gravity and absorption of coarse aggregates were measured according to ASTM C127 (2015) for particle size retained on sieve#4 and ASTM 854 (2023) Method B for finer particles, wherein oven-dry aggregates were soaked for 24 hours, surface-dried, and weighed in air and submerged to determine specific gravity and water absorption. Table 2-3 summarizes gradation properties of the coarse and fine angular materials, including factors such as mean particle size (d_{50}), coefficient of curvature (C_c), uniformity coefficient (C_u), as well as specific gravity (G_s), maximum void ratio (e_{max}), and minimum void ratio (e_{min}). Appendix B presented the grain distribution curves of tested OGA.

Table 2-3. Characteristics of granular materials

Material	C_u	C_c	d_{50} (mm)	G_s	e_{max}	e_{min}
A01	2.40	0.80	13.20	2.700	0.849	0.609
A02	1.96	0.91	11.70	2.795	0.893	0.632
A03	2.54	0.81	13.50	2.825	0.881	0.621
A04	2.26	1.11	14.15	2.751	0.933	0.629
A05	1.97	0.88	10.50	2.800	0.886	0.602
A06	1.89	1.05	15.65	2.766	0.961	0.648
A07	1.94	1.09	11.96	2.724	0.967	0.666
A08	2.04	1.11	13.10	2.738	0.919	0.642
A09	2.01	1.15	14.50	2.648	0.879	0.627
A10	2.25	1.36	16.00	2.688	0.917	0.688
A11	2.29	1.17	13.80	2.642	0.883	0.611
A12	3.16	1.19	13.75	2.676	0.818	0.533
A13	1.84	1.13	13.65	2.662	0.894	0.644
A14	2.32	0.95	11.10	2.691	0.855	0.581
A15	1.64	0.98	15.45	2.761	0.893	0.658
A16	1.98	1.08	12.09	2.590	0.924	0.636
A17	1.86	1.16	15.00	2.610	0.959	0.686
A18	2.33	1.04	13.80	2.535	0.950	0.627
A19	1.58	1.01	15.10	2.314	0.776	0.571
A20	1.63	1.03	14.95	2.667	0.944	0.648
A21	1.70	1.063	16.70	2.633	0.941	0.676

A22	2.04	1.02	12.70	2.383	0.695	0.516
A23	1.48	0.92	13.05	2.283	0.796	0.543
A24	2.14	0.94	15.60	2.408	0.755	0.576
A25	1.48	1.05	18.45	2.687	0.942	0.684
A26	2.01	1.21	14.70	2.687	0.911	0.641
#1 Dry Glass Sand	1.00	1.00	0.36	2.650	0.947	0.626
GS#40 Columbia Sand	1.00	1.00	0.36	2.650	0.946	0.643
F-35 Ottawa Sand	1.00	1.00	0.36	2.650	0.763	0.490
Glass Beads	1.00	1.00	0.36	2.550	0.800	0.565

2.2.2 Direct shear tests

A special large-scale direct shear (LSDS) apparatus was employed to determine the shear strength properties of coarse granular specimens (aggregates and gravel samples; Figure 2-1). The apparatus is equipped with both vertical and horizontal actuators. The actuator features a load cell with a capacity of 1000 kN (~225 kip) and a linear variable differential transformer (LVDT) with a range of 254 mm (~10 in.). The shear box has a square cross-section measuring 0.50 m × 0.50 m and 0.40 m in height. A fixed gap of 20 mm separates the upper and lower sections of the shear box. The upper half of the shear box is rigidly connected to a vertical steel column, while the bottom half is designed to move horizontally during shearing. A series of direct shear tests was conducted on the tested samples at a D_r of 30% to represent a loose state and D_r of 80% to represent a dense state. Each aggregate type was tested under normal stresses of 35, 70, 105, and 140 kPa (~5, 10, 15, and 20 psi), to represent typical stress ranges encountered in backfill applications behind retaining walls.

Dense specimens were prepared by placing the aggregate into six individual layers, with compaction applied at each respective layer to achieve the target D_r, resulting in a specimen height of 0.35 m. The loose specimens were prepared by pouring the aggregate in three layers utilizing a funnel, with minimal compaction effort to maintain the loose state of the aggregate. For each test, the vertical load was applied over a short duration (15–90 seconds). Once the target load was reached, horizontal shearing was initiated at a constant displacement rate of 1 mm/min until achieving a total shear strain of 20%. All displacement and load measurements were recorded utilizing a data acquisition system (DAC), and the data were automatically saved on the computer at 5-second intervals. Direct shear tests of fine granular soil were conducted by Lee (2017).

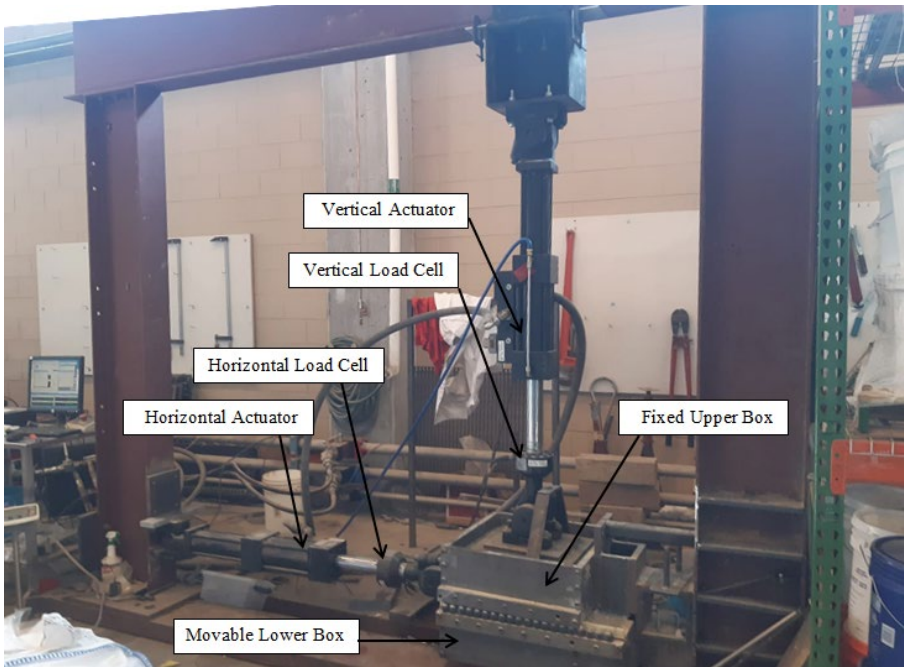

Figure 2-1. Components of Large-Scale Direct Shear Apparatus

2.2.3 Large Triaxial compression (LTX) test

Large triaxial compression tests were conducted on A26 as a representative of crushed limestone and were additionally used as backfill for the retaining wall (See Section 2.3). The test was performed at a target relative density (Dr) of 80%. To achieve this density, the required mass of oven-dry aggregate was calculated and prepared. Prior to the specimen assembly, a thin layer of vacuum grease was applied to the vertical surfaces of the pedestal to ensure proper sealing, and a latex membrane was secured to the base using an O-ring. The membrane was then pulled over a split mold under a vacuum of approximately 12 psi to maintain a uniform cylindrical shape during specimen preparation. The aggregate was deposited and compacted into the mold in six layers to achieve the target relative density. A vacuum of 12 psi was then switched to the pore space to prevent specimen collapse during the removal of the split mold and subsequent assembly of the triaxial cell. After finishing filling the mold, the top end plate was placed, and the membrane was sealed using two additional O-rings. To minimize the risk of membrane puncture from the angular aggregate particles, a secondary latex membrane was applied as a protective layer. The specimen dimensions (height and diameter) were measured using the ImageJ digital image analysis software. The step-by-step specimen preparation process is illustrated in Figure 2-2.

The triaxial tests were performed under confining pressures of 50, 100, and 200 kPa. Axial loading was applied at a constant displacement rate of 1 mm/min until a total axial displacement of 45 mm was reached (equivalent to 15% axial strain based on the initial specimen height). To provide more reliable estimates of the elastic modulus (E), unloading-reloading cycles were performed at axial strain levels of approximately 2% and 5%. As shown in Figure 2-3, the axial load was measured using a vertical load cell with a capacity of 44.48 kN (~100,000 lbf), while axial deformation was recorded using an LVDT with a travel range of 76.2 mm (~3 in.). All signals from the load cell, LVDTs, and confining pressure transducer were transmitted to a data acquisition control (DAC) system.

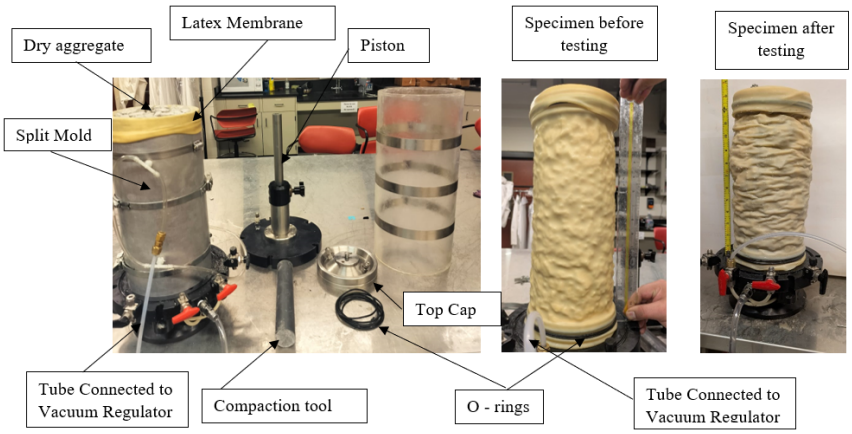

Figure 2-2. Procedure of Sample Preparation

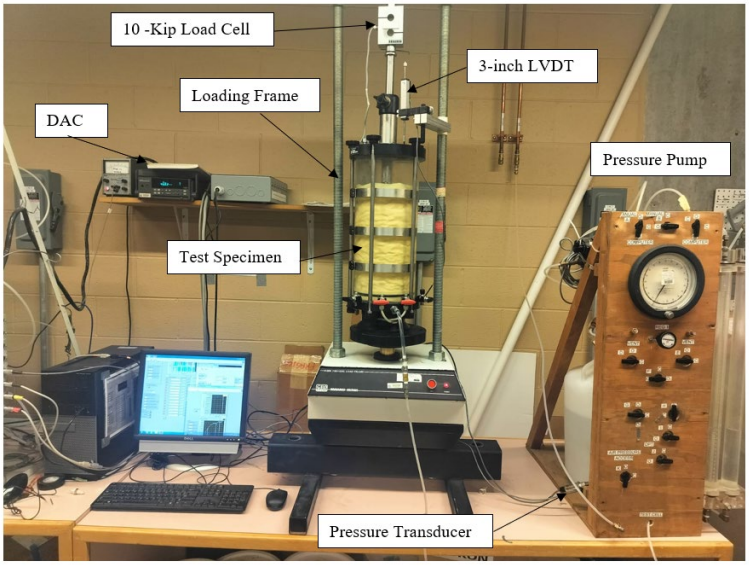

Figure 2-3. Components of Large Triaxial Compression (LTX) Apparatus

2.2.4 3D X-Ray Computed Tomography Image Collection and Processing

3D X-ray micro-computed tomography (μCT) scans were acquired for representative samples of coarse granular material using the TESCAN CoreTOM scanner at UGCT Core Facility, Ghent University, Belgium, optimized for high-quality imaging of a wide range of samples. The scanner is equipped with a 180 kV X-ray tube and a large 2856 x 2856 pixel flat-panel detector, allowing for detailed imaging at a spatial resolution down to 3 μm/pixel. It accommodates various sample sizes, supporting a scannable height of up to 1 m and a maximum sample weight of 45 kg. With nine motorized axes, the system enables multi-scale imaging using a global coordinate system integrated into both the acquisition and reconstruction software. It supports (stacked) circular and helical scan trajectories, as well as time-lapse and continuous imaging of dynamic processes, with scan times as short as five seconds per 360° rotation.

The coarse granular specimens were placed inside acrylic tubes that had a diameter of 63.5 mm (2.5 in.) and a height of approximately 254 mm (10 in.). The scans were conducted at an energy of 180 keV and a power of 55 W. Each projection was captured with an exposure time of

approximately 450 milliseconds, ensuring sufficient signal accumulation for high image quality. The scans were taken with a binning of 2 and comprised 2,142 individual radiographs acquired over a full 360° rotation. Additionally, a 0.5-mm copper (Cu) filter was used to attenuate low-energy X-rays from the beam, a common practice to reduce image noise and beam-hardening artifacts while enhancing the penetration of higher-energy X-rays through dense materials. The μCT scans had a voxel size of 55 μm sufficient for accurate morphology analysis. Five scans were taken to cover the entire height of the specimens, requiring approximately 85-90 minutes. The raw data were reconstructed using PANTHERA (TESCAN XRE), during which beam-hardening corrections and ring filters were applied. During this stage, the multiple scans of each specimen were merged, resulting in a stack of 16-bit cross-sections capturing nearly the full height of the specimen.

The reconstructed images of aggregate specimens were processed to generate binary images and were then converted into labeled images to identify each particle with a unique identification number. These labeled images formed the basis for calculating the morphological properties of the aggregate particles where PerGeos software of Thermo Scientific (2022) was employed to process the reconstructed images (Figure 2-4a). To enhance image quality, an anisotropic diffusion filter was applied to the grayscale images. This filtering technique reduced image noise, enhanced particle boundaries, and improved contrast while preserving edge definition. The filter algorithm operates by diffusing voxel values only when the intensity difference between neighboring voxels remains below a predefined diffusion threshold. The threshold process was optimized through parametric studies and error analysis, resulting in smoothed grayscale images with sharply defined interfaces between solid particles and the surrounding void space (Figure 2-4b).

Following noise reduction, segmentation was carried out to separate solid particles from the background medium. An interactive thresholding approach was used to convert the grayscale images into binary format, assigning voxels with high X-ray attenuation (representing solid aggregate particles) a value of 1 and voxels with low attenuation (representing voids or the surrounding medium) a value of 0. This process produced binary images that accurately depicted particle boundaries and contact points at the image resolution scale (Figure 2-4c). For further refinement of the binary images, morphological image processing techniques were applied. First, a fill-holes algorithm was used to eliminate internal voids enclosed within particles without altering their surfaces. Next, the opening operation was applied to remove residual noise in the surrounding medium while preserving the overall particle geometry. These steps produced a clean binary image (Figure 2-4d), which served as a mask for the subsequent labeling process. In preparation for particle labeling, it was necessary to separate touching particles. This was accomplished using PerGeos' Separate Objects module, which combines distance transform, watershed segmentation, and numerical reconstruction algorithms. This step isolated individual particles by removing minor contact bridges between them, resulting in a fully separated binary image. After segmentation, particles were uniquely labeled using the Labeling command, and their physical contacts were restored for analysis while preserving the distinct labels (Figure 2-4e). The labeled image provided an accurate depiction of in-contact, uniquely indexed particles. PerGeos' Label Analysis and Filter Analysis modules were then employed to identify and remove mislabeled noise particles. Filtering was performed based on parameters such as particle volume, mean intensity, 3D area, spatial location, and proximity to image boundaries. Noise particles were filtered out using the mean filter module, which isolated their specific labels for exclusion from further analysis.

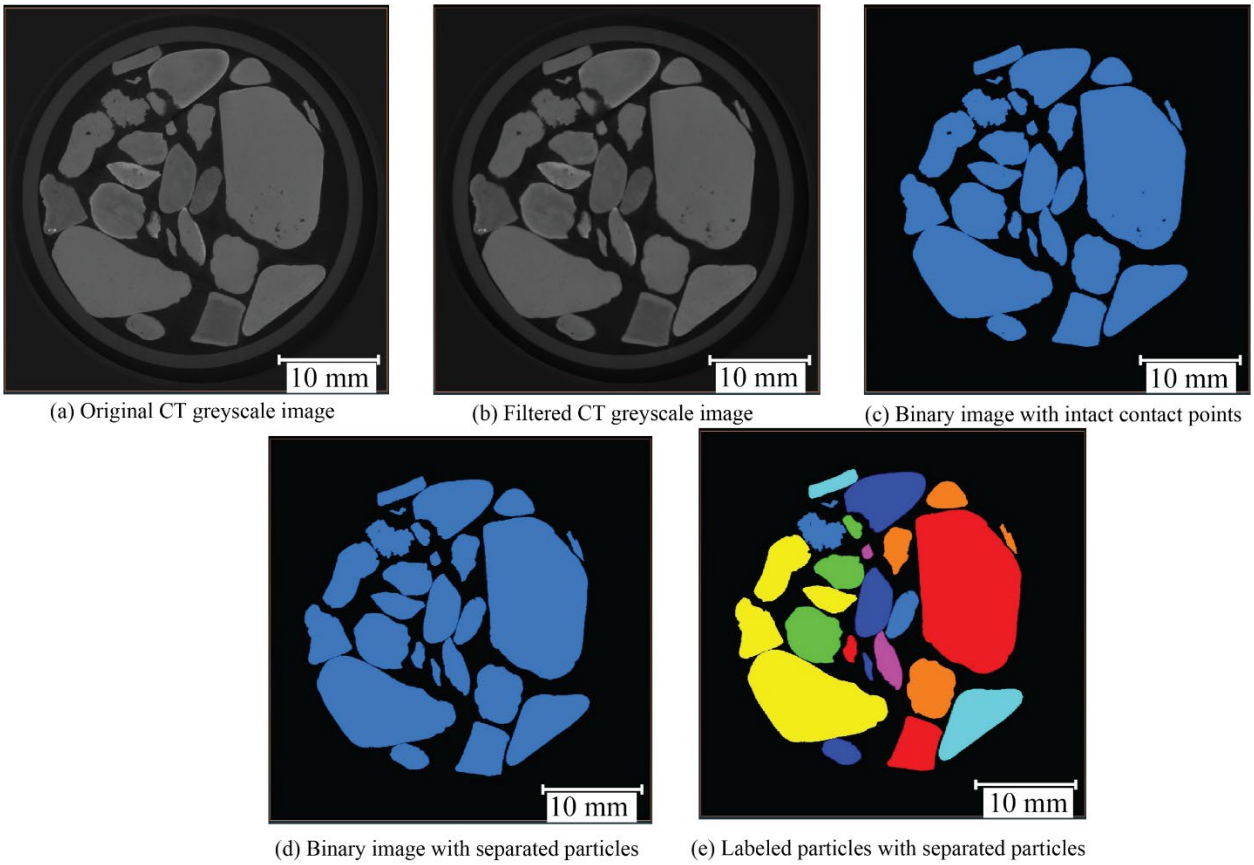

(a) Original CT greyscale image (b) Filtered CT greyscale image (c) Binary image with intact contact points

(d) Binary image with separated particles (e) Labeled particles with separated particles

Figure 2-4. Steps of the particle identification process.

The PerGeos output of the aggregate particles was processed using a special computer code that was developed by Druckrey et al. (2016). Initially, the labeled image was imported into memory as a 3D matrix, and each particle-labeled voxel was identified during the first iteration. During each iteration of the loop, the spatial coordinates of each particle's voxels were recorded in an n x 3 matrix, where n represents the number of voxels associated with a particular particle in that iteration. The three columns of the particle matrix represent the x-, y-, and z-coordinates of the voxels comprising the particle, facilitating the calculation of the particle's physical attributes. The volume of each particle was determined by summing all voxels within the particle, equivalent to measuring the length of the n x 3 matrix. After each iteration of the loop, the particle volume was appended to a vector containing all particle volumes from previous iterations.

The morphology of the aggregate is represented by three Indices; they are the sphericity index (I_{sph}), roundness index (I_R), and form (F). Alshibli et al. (2015) defined these morphology indices as:

$$I_{sph} = \frac{V_p}{Vs} \qquad (2-1)$$

$$I_R = \frac{A_p}{4\pi\left(\frac{d_L+d_I+d_S}{6}\right)^2} \qquad (2-2)$$

$$F = d_S/d_L \qquad (2-3)$$

$$I_R = \frac{A_p}{4\pi\left(\frac{d_L+d_I+d_S}{6}\right)^2} \qquad (2-2)$$

$$F = d_S/d_L \qquad (2-3)$$

While $V_p, and\ A_p$ are the actual volume and surface area of the particles, respectively. The denominator in Eq. (2-2) represents the surface area of a sphere with a diameter equal to the average of the shortest (d_S), intermediate (d_I), and longest (d_L) lengths of the particle that pass through its center of mass. Vs is the volume of sphere with a diameter equal to d_S. I_{sph} equals unity for a spherical particle, representing maximum sphericity. Similarly, I_R reaches a value of unity for particles that exhibit smooth surfaces with no corners, characteristic of an ideal sphere. The form factor (F) quantifies particle elongation, ranging from values close to zero for highly platy or elongated particles to 1 for perfectly equant, spherical particles. I_{sph} , I_R, and F are essential for characterizing particle geometry, which directly affects the packing behavior, shear resistance, and the overall shear strength of granular materials. The particle morphology indices of the fine granular material were reported by Alshibli and Cil (2018).

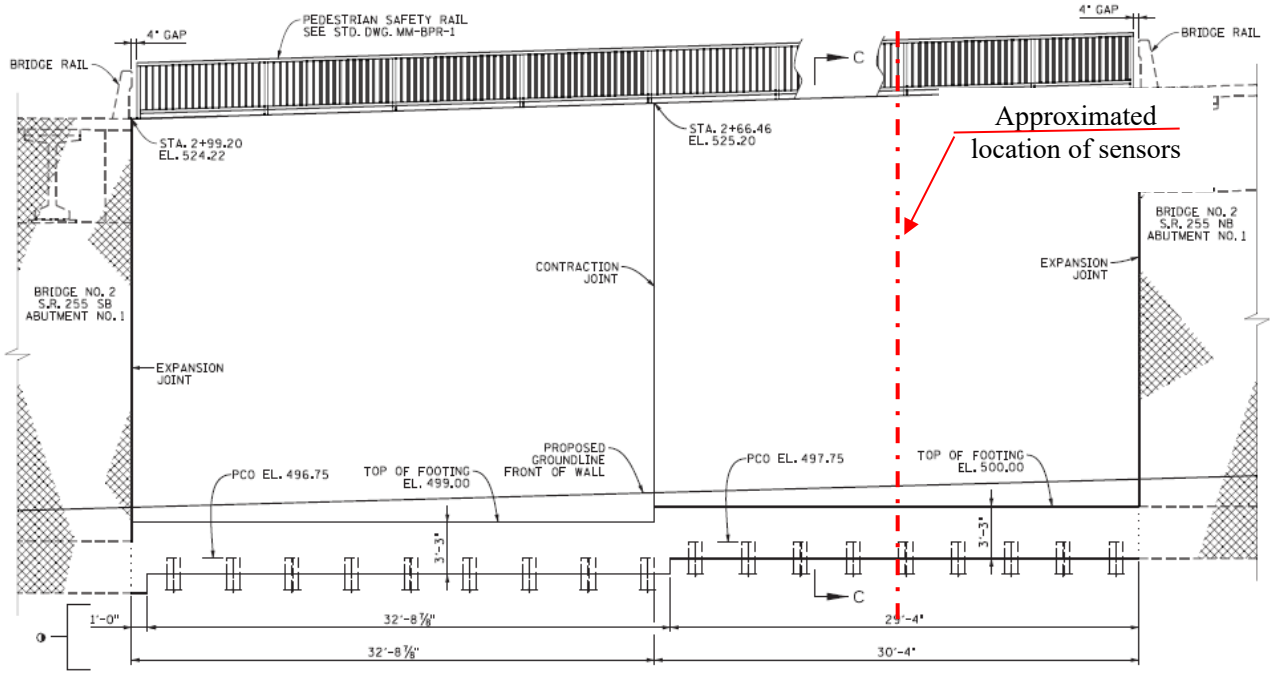

Figure 2-5. Elevation view of wall No.6 from wall STA. 2 +97.18 to wall STA. 3 + 61.84 (Source: TDOT Drawings).

2.3 Field measurement of Active lateral Earth pressure on a cantilever wall

The field data to measure the active earth pressure was performed on cantilever retaining wall No.6 from wall STA. 2+97.18 to wall STA. 3+61.84, close to Nashville airport. Figure 2-5 shows the elevation profile of the wall with the approximate location of all sensors. The top elevation of the footing and the wall stem are ~493 ft and ~528 ft, respectively. The height of the wall's stem is ~33 ft (10.18 m).

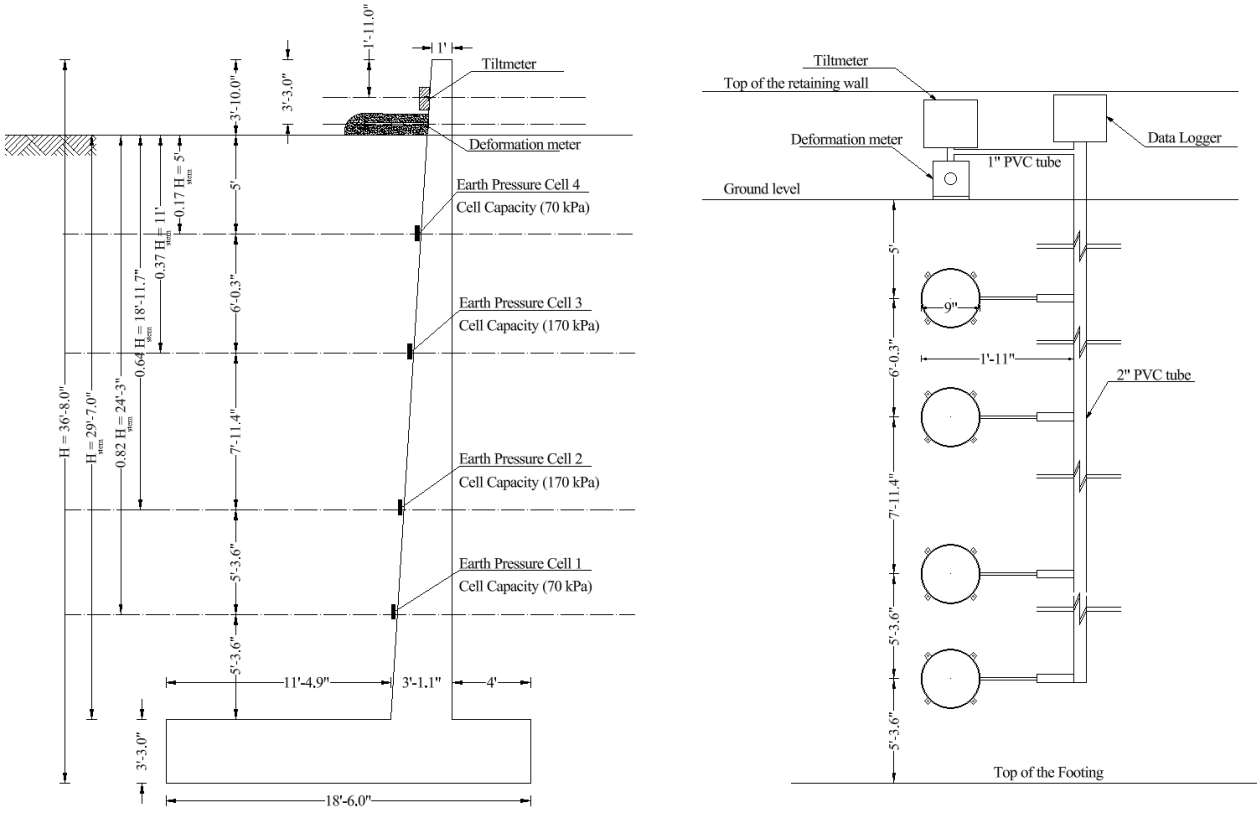

Figure 2-6. Schematic diagrams showing the location of all sensors on the back of the wall (a) Cross-section of the retaining wall with sensors, (b) view of the back of the wall with sensors

2.3.1 Earth pressure cells

Four earth pressure cells were used to measure the lateral earth pressure at multiple locations. The stainless-steel pressure cells consist of a thick base plate and a thin diaphragm welded along the edges to form a 230-mm-diameter thin circular cavity. In profile, each stress cell is approximately 6 mm thick. The thin circular cavity contains an incompressible, deaired glycol fluid of low freezing temperature (Figure 2-7). A stiff stainless-steel tube connects the fluid to a VW transducer located away from the cell edge ensuring that the presence of the transducer housing does not affect the pressure registered by the stress cell. Changes in contact pressure over the flexible face of the cell induce movement of a diaphragm in the VW transducer. The frequency response of the vibrating wire attached to the diaphragm changes in response to the applied pressure. The pressure cell has temperature measurements for accurate calibration.

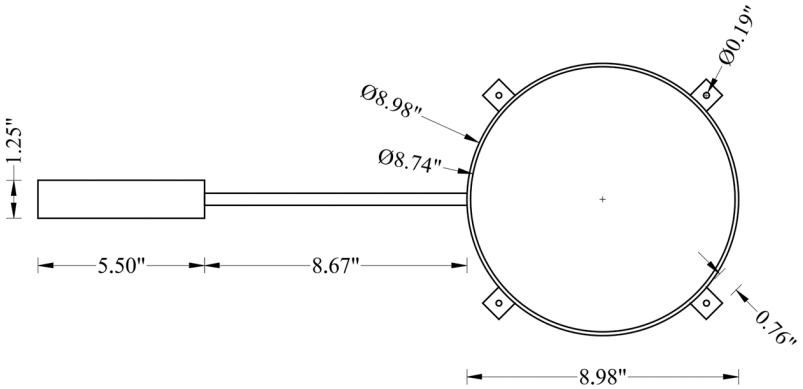

(a) Dimensions of the VW Earth Pressure Cell.

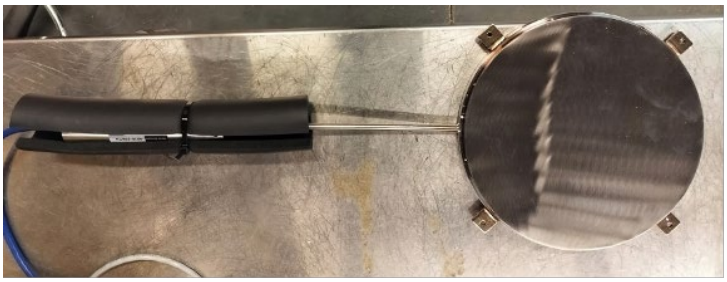

(b) Photo of the VW Earth Pressure Cell.

(c) Field installation of pressure cell.

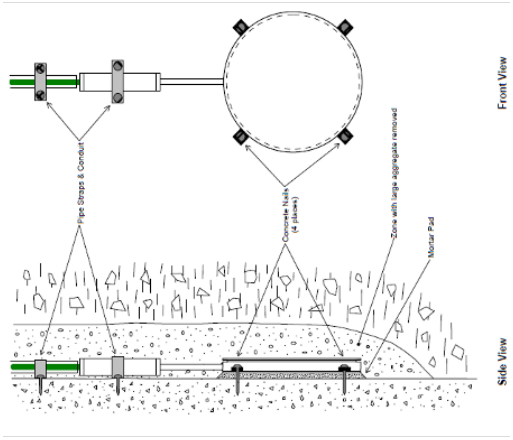

(d) Schematic of the installation.

Figure 2-7. Photo and installation of the VW Earth Pressure Cell.

The following are the specifications of the pressure cells:

- The model of the VW Earth Pressure Cells No. 1 and No. 4 is 4800 series and has a capacity of 70 kPa with a resolution of ± 0.025% FSR and an accuracy of ± 0.5% FSR with linear expression and ± 0.1 % FSR with polynomial expression.
- The model of the VW Earth Pressure Cell No. 2 and No. 3 is 4800 series and has a capacity of 170 kPa with a resolution of ± 0.025 % FSR and an accuracy of ± 0.5 % FSR with linear expression and ± 0.1 % FSR with polynomial expression. Figure 2-7 shows the approximate dimensions, installation method, and a photo of VW Earth Pressure.

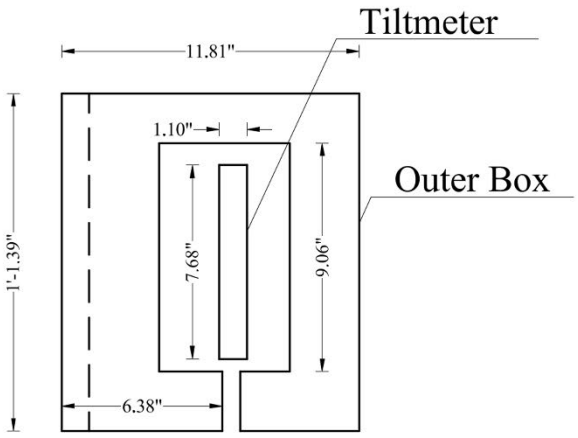

(a) Dimensions of the VW tiltmeter with the protection box.

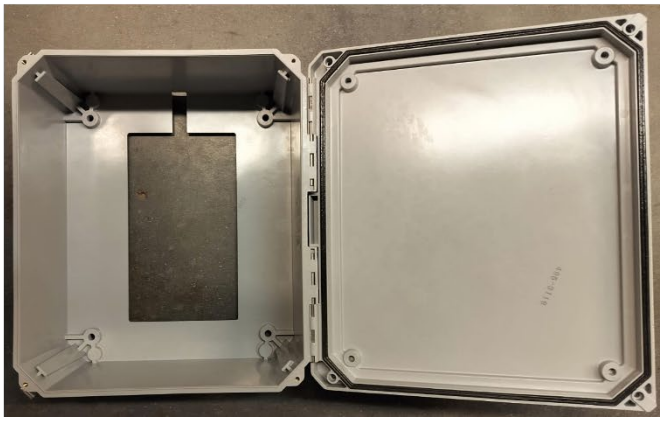

(b) Photo of the protective box for the tiltmeter.

(c) Photo of the tiltmeter.

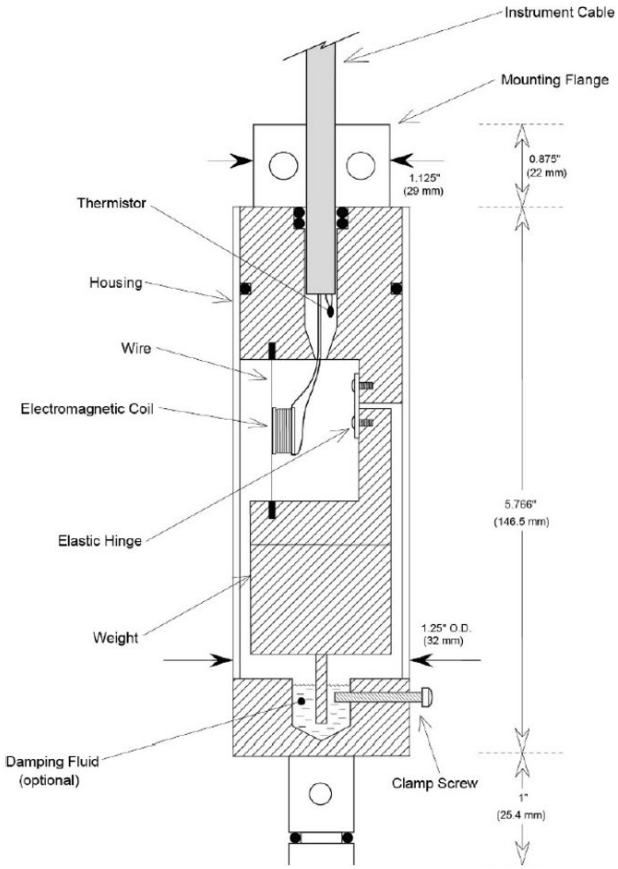

(d) Schematic cross section of the tiltmeter.

Figure 2-8. Photo and installation details of the VW tiltmeter.

2.3.2 Tiltmeter

The VW tiltmeter (Figure 2-8) measured the rotation of the wall, and was installed at approximately 1.1 ft below the top of the wall on the back face of the stem. The tiltmeter is Model 6350 and has a range of ± 10° with a resolution of ± 0.50 mm/m and an accuracy of ± 0.3 % FSR

utilizing linear expression and ± 0.1 % FSR with polynomial expression. The VW tiltmeter is protected inside a box to ensure free rotation.

2.3.3 Data Logger

All sensor wires were connected to the GEOKON GeoNet 8940 datalogger (Figure 2-9). A GeoNet Model 8940 datalogger (GEOKON, USA) was used to record field measurements during the monitoring program. The 8940 is a compact, low-power geotechnical datalogger designed for vibrating-wire and thermistor-based sensors, providing reliable data acquisition in remote and harsh environments. A grounding rod was installed in the field and connected to the datalogger.

(a) Photo of the datalogger

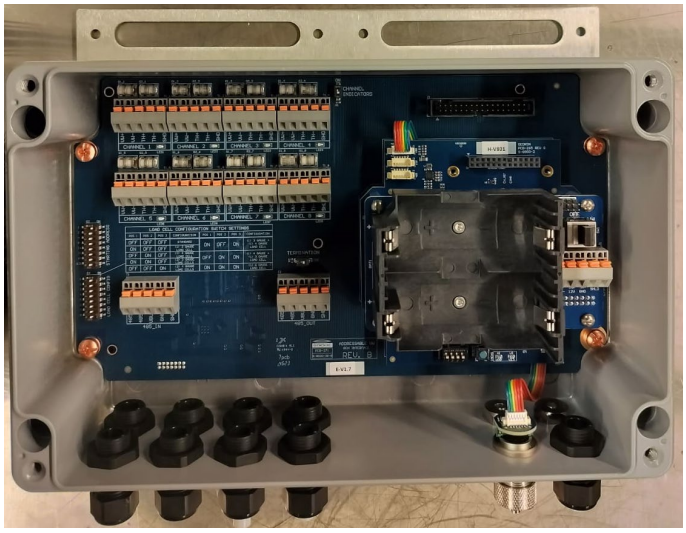

(b) Photo of the inside of the datalogger

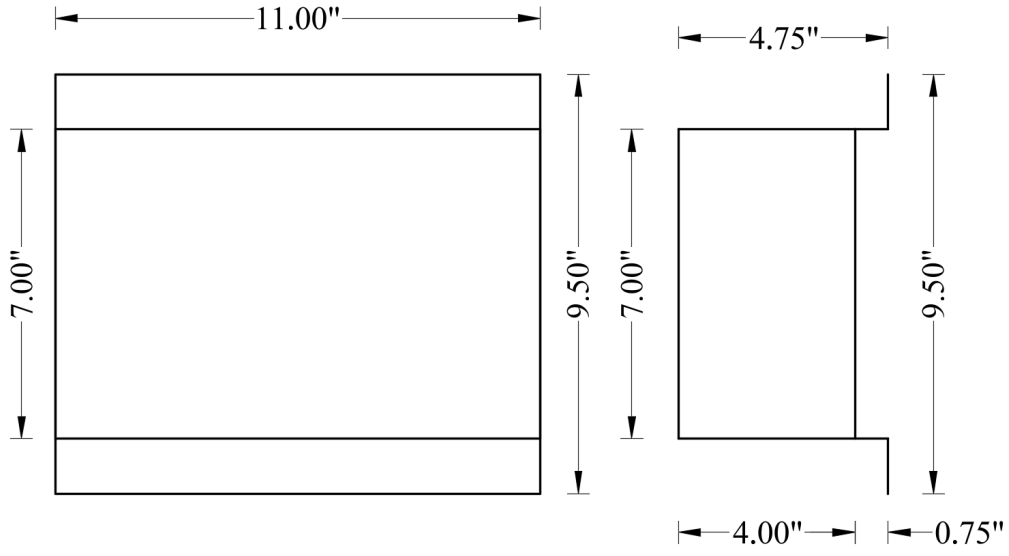

(c) Dimensions of the datalogger

Figure 2-9. Photos and dimensions of the data logger

2.3.4 Deformation meter

The wall stem may translate in the lateral direction. A VW deformation meter was bolted to the back face of the wall stem near the top of the wall stem (3.25 ft below the top) to measure the relative deformation between the two flanges of the deformation meter (Figure 2-10). The second flange of the deformation meter was secured within the backfill using two anchors, each with a length of 1 ft, embedded in the backfill material to ensure stable fixation and accurate deformation measurements. Fine sand was used around the sensor. Figure 2-11 depicts the final layout of the sensors and the GeoNet datalogger in the field. The instrumentation was installed in two stages. The first stage was completed on August 13–14, 2024 and included the installation of the four earth pressure cells, the tiltmeter, and the datalogger. The deformation meter was installed later during the second stage on February 17, 2025, after the backfill material had reached the required elevation for its placement. Sensor readings were subsequently downloaded during site visits on May 5, 2025, July 16, 2025, and October 20, 2025.

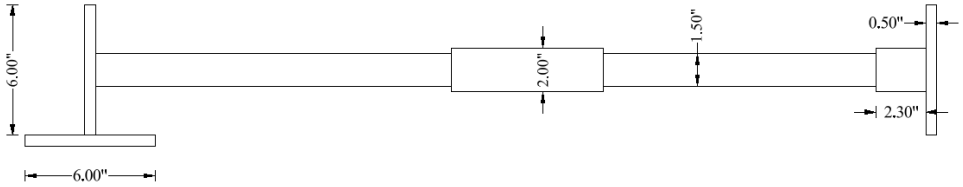

(a) Schematic of VW deformation meter.

(b) Photo of VW deformation meter.

Figure 2-10. (a) Schematic of VW deformation meter; (b) Photo of Model 4430 VW deformation sensor.

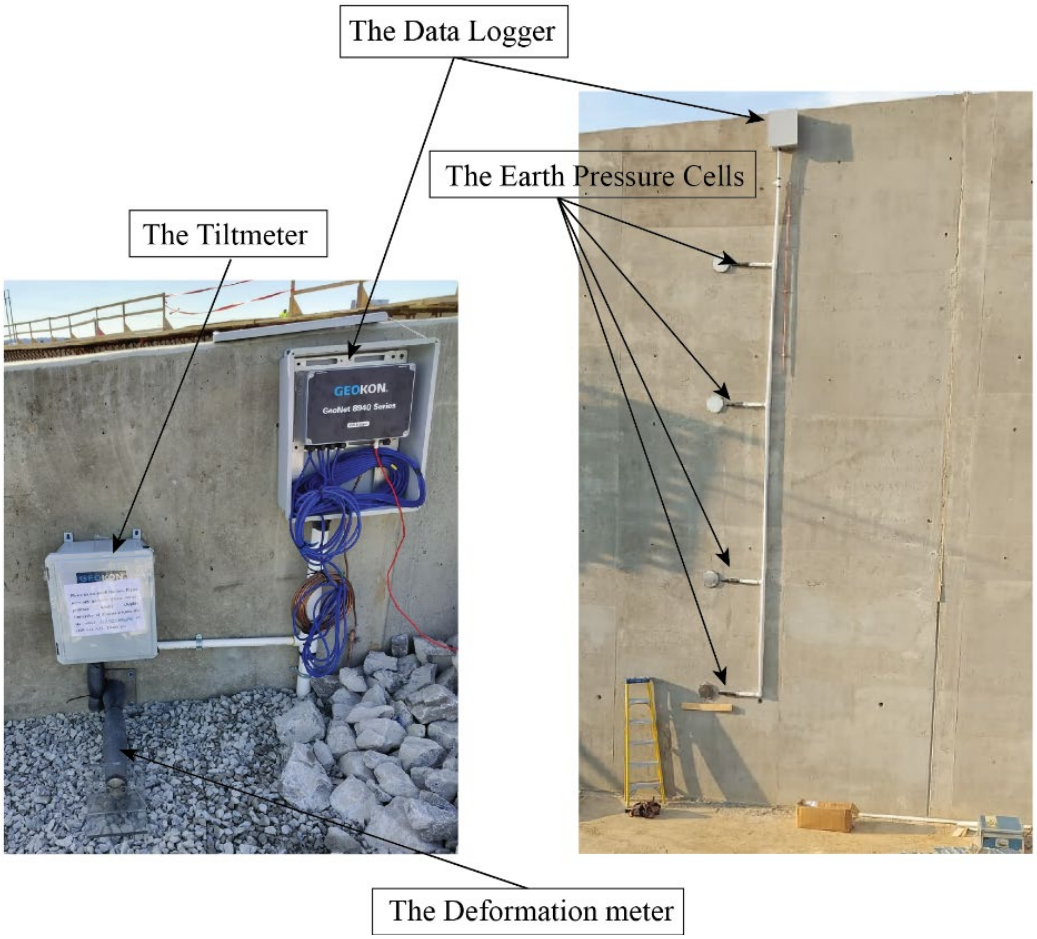

Figure 2-11. Construction of the sensors, and the datalogger at wall No.6 from wall STA. 2+97.18 to wall STA. 3+61.84.

Chapter 3 Test Results

3.1 Direct shear tests results

The normalized shear strength with respect to the normal stress ($\frac{\tau}{\sigma_N}$) versus the shear strain is shown in Figure 8-3 (a) - Appendix (C). The normal displacement versus the shear displacement for coarse and fine granular materials is shown in Figure 8-3 (b) and Appendix (C). The volume expansion is considered to be positive. The $\frac{\tau}{\sigma_N}$ of dense specimens exhibits a distinct peak shear strength occurring at a shear strain ranging from approximately 6% to 10% for coarse granular materials and approximately from 1.3% to 4% for fine granular materials. In contrast, loose specimens show a gradual increase in shear stress that eventually reaches the critical state (CS) shear strength of the dense specimens. A higher initial density combined with low confining pressure leads to an elevated peak $\frac{\tau}{\sigma_N}$, followed by more pronounced post-peak softening. Figure 8-3(A01-a), and (A18-a), show similar behavior of two crushed limestone aggregates with similar gradation properties but different mineral compositions, confirming that mineralogy has negligible influence on the shear strength of granular materials. Figure 8-3 (a) shows that crushed limestone aggregates have a higher shear strength than river gravel specimens [(Figure 8-3 (A19-a), (A22-a), (A23-a), and (A24-a)]. This behavior is attributed to the interlocking effect caused by the particles' angularity of limestone specimens. Additionally, $\frac{\tau}{\sigma_N}$ of river gravel specimens exhibited oscillatory behavior either during the post-peak regime (when a peak state is present) or upon reaching the critical state [Figure 8-3 (A19-a), (A22-a), (A23-a), and (A24-a)]. This response is attributed to slip-stick interactions between particles as they shear against one another due to their smoother surface (Alshibli and Roussel 2006).

Figure 8-3 (b) illustrates that dense specimens exhibit a dilative behavior after a brief initial contraction across all normal stresses. Volume expansion is more pronounced in very dense specimens, while the value of dilation decreases as the normal stress increases. Furthermore, loose specimens exhibit slight dilative behavior at low σ_N. Within dense specimens, the dilation rate was initially high and gradually decreased at large strains approaching the critical state. In contrast, the loose specimens displayed an initial contractive response, followed by a modest dilation rate that persisted until the end of the experiment. Figure 8-3 (b) demonstrates that crushed limestone aggregates reach the critical state condition at a higher shear displacements than river gravels. Although both of them have convergent values of the dilatancy angles *(ψ)* at different levels of σ_N, this behavior has been supported by several studies in the literature. For instance, Cho et al. (2006) demonstrated that natural sands with angular particle shapes, such as crushed limestone, display higher shear strength and require greater strain to reach critical conditions compared to rounded sands like river gravel. Wood (1990) also emphasized that the evolution of fabric and dilatancy associated with angular particles contributes to a delayed approach to the critical state.

The critical state friction angle (ϕ_{cs}) of both crushed limestone and river gravel demonstrates a pronounced dependency on the level of applied σ_N. For crushed limestone, ϕ_{cs} increased from 44° at the highest σ_N of 140 kPa to 66.9° at the lowest stress level of 15 kPa. A similar trend was observed for river gravel, where ϕ_{cs} rose from 44° at 140 kPa to 60.6° at 15 kPa. The peak friction angle (ϕ_p) followed a similar trend but exhibited higher values overall. For crushed limestone, ϕ_p

increased from 54.8° at 140 kPa to 73° at 15 kPa, while river gravel showed an increase from 52.8° to 69.2° across the same stress range. Furthermore, ψ for both materials showed a consistent converging trend, increasing from 5.3° at 140 kPa to 15.9° at 15 kPa. These results collectively highlight the inverse relationship between σ_N and the shear strength parameters of granular materials, wherein higher normal stress reduces particle dilation, thereby lowering both ϕ_p and ϕ_{cs}. The higher friction angles observed in crushed limestone compared to river gravel at similar stress levels can be attributed to its more angular particle shape, which enhances interparticle interlocking and resistance to shear. In contrast, the increased rounded morphology of river gravel leads to reduced mechanical interlocking, thereby slightly lowering ϕ_p and ϕ_{cs} under similar test conditions.

The shear strength characteristics of the tested materials are summarized in Appendix E, and Appendix F. Figure 8-3(c) illustrates the relationship between peak shear resistance, critical state shear strength and the applied normal stress σ_N. The Figure also presents the corresponding dilatancy angle (ψ) values evaluated at various normal stress levels. A higher-order regression model was employed to describe the relationship between ϕ_p and σ_N. ϕ_{cs} was evaluated for both loose and dense specimens at each applied normal stress level. To characterize the critical state envelope, a linear regression forced to pass through the origin was fitted to the critical state shear stresses, enabling the estimation of an average ϕ_{cs}. A higher-order model was similarly used to represent the relationship between critical state shear stress and normal stress. ψ exhibited a systematic decrease with increasing normal stress for all tested aggregates, and this trend was also captured using a higher-order regression formulation.

3.2 Large triaxial compression test

Figure 3-1 presents the relationship between axial strain and the Principal Stress Ratio (PSR) for the tested specimens of A26 aggregate under different confining pressures. As shown, the specimens exhibited a higher peak PSR value of approximately 8.25 at the lowest confining pressure (50 kPa), while a reduced peak PSR of about 5.60 was observed at the highest confining pressure (200 kPa). Using Equation (3-1), ϕ_{cs} was found to decrease from 51.6° at 50 kPa to 44.2° at 200 kPa, indicating a stress-dependent frictional response typical of granular materials.

The volumetric behavior also varied with confinement. At lower confining pressures (50 and 100 kPa), the specimens demonstrated dilation, characterized by an increase in volume during shearing. In contrast, a contractive behavior was observed at the higher confining pressure of 200 kPa. The dilatancy angles (ψ); calculated using Equation (3-2), ranged from 12.1° at 50 kPa to 8.9° at 100 kPa, reflecting the reduction in particle interlocking with increasing confinement. A summary of specimen properties and the corresponding strength parameters is provided in

Table 3-1.

$$\sin(\phi_{CS}) = \frac{PSR-1}{PSR+1} \qquad (3-1)$$

$$\sin(\psi) = \frac{\frac{\varepsilon_v^p}{\varepsilon_a^p}}{2+\frac{\varepsilon_v^p}{\varepsilon_a^p}} \qquad (3-2)$$

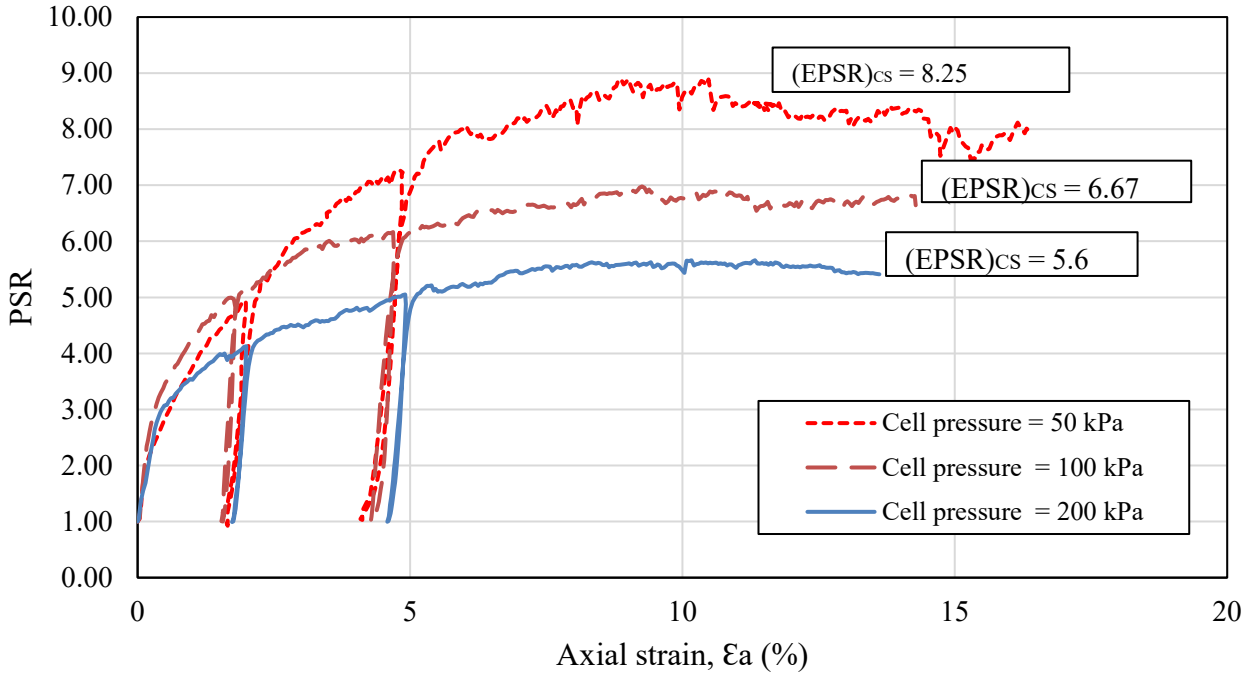

(a)

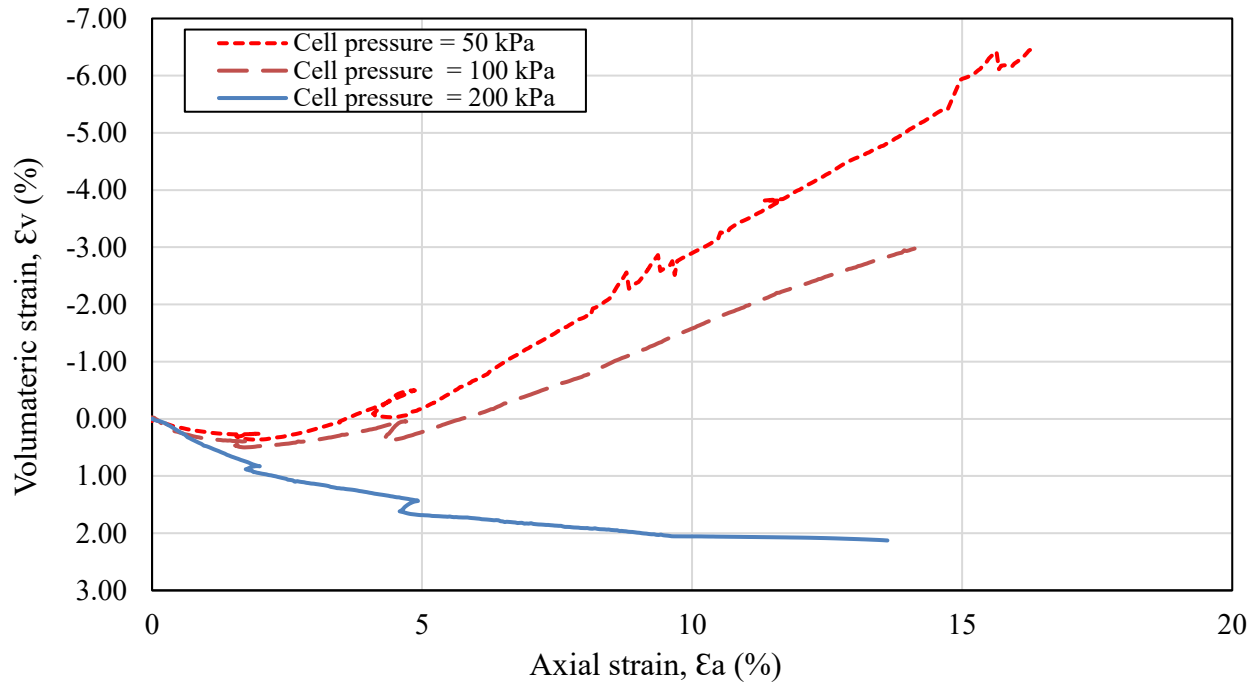

(b)

Figure 3-1. Results of LTX on A26: (a) EPSR versus Axial Strain at Different Confining Pressure; (b) Volumetric Strain versus Axial Strain at Different Confining Pressure.

Table 3-1. Physical and strength properties of triaxial experiments on A26 aggregate.

Property	Test 1	Test 2	Test 3
H_o (mm)	310.00	313.00	307.60
Perimeter (mm)	467.33	471.67	480.33
D_o (mm)	148.76	150.14	152.89
D_o actual	147.49	147.60	150.35
H_o/D_o	2.10	2.12	2.05
A_o (mm2)	1.71E+04	1.71E+04	1.78E+04
V_o (mm3)	5.30E+06	5.36E+06	5.46E+06
Membrane thickness (mm)	1.27	1.27	1.27
Membrane young modulus (kPa)	1400	1400	1400
dry weight (g)	8707	8547	8707
dry unit weight (g/cc)	1.64	1.60	1.59
specific gravity of solids (G_s)	2.69	2.69	2.69
max. void ratio (e_{max})	0.91	0.91	0.91
min. void ratio (e_{min})	0.64	0.64	0.64
specimen void ratio (e)	0.63	0.68	0.69
Relative Density	102.35	84.18	83.50
Deviator stress at CS (kPa)	378.00	579.00	915.00
Slope of volumetric strain (ε_v) Vs axial strain (ε_a)	0.54	0.37	-----
PSR at the critical state (CS)	8.25	6.67	5.60
critical friction angle (degree)	51.61	47.67	44.18
Dilatancy angle (degree)	12.05	8.90	-----
Modulus of Elasticity (E_1) (kPa)	3.89E+04	8.89E+04	1.07E+05
Modulus of Elasticity (E_2) (kPa)	4.07E+04	1.60E+05	2.42E+05
Modulus of Elasticity (E_3) (kPa)	4.61E+04	1.18E+05	2.11E+05
Deviator stress at the end of the elastic zone	50	170	360
Poisson's ratio	0.23	0.22	0.22
Elastic Volumetric Strain	0.29	0.30	0.51
Plastic Volumetric Strain	3.75	2.04	-2.57

3.3 Morphology data analysis

Particle size was determined based on the average of the shortest (d_S) and intermediate lengths (d_I) of the particle providing a more accurate comparison to mechanical sieving. This averaging method better reflects the physical behavior during sieving, where a particle may pass through a mesh opening along its smallest axis, but be retained due to its orthogonal intermediate dimension (Druckrey et al. 2016). As a result, a small number of particles appear larger than what mechanical sieving alone would predict. Figure 8-4 in Appendix (D-1) exhibits the particle size distribution of fine and coarse angular materials.

The probability histograms of morphology indices were analyzed to determine the most suitable probability distribution. Various distributions, including normal, lognormal, Weibull, gamma, generalized extreme value (GEV), exponential, and non-standardized Student's t-distribution, were tested, and the best fit was selected based on the Akaike information criterion (AIC). The AIC is a widely used statistical metric for model selection, providing a measure of the trade-off between the goodness of fit of a model and its complexity. When applied in the context of regression models with normally distributed errors, AIC can be approximated using the following relationship:

$$AIC \approx n\,log\left(\frac{SSE}{n}\right) + 2k \qquad (3-3)$$

where n is the number of observations, SSE is the sum of squared errors of the model, and k is the number of estimated parameters (including the intercept). The results indicated that sphericity histograms were best fitted by the GEV distribution. The probability density function (PDF) of the GEV distribution is defined as:

$$f(x,\xi,\mu_1,\sigma_1) = \begin{cases} \frac{1}{\sigma_1}\left(1+\xi\frac{x-\mu_1}{\sigma_1}\right)^{-\frac{1}{\xi}-1} exp\left(-\left(1+\xi\frac{x-\mu_1}{\sigma_1}\right)^{-\frac{1}{\xi}}\right), if\ \xi \neq 0, and\ 1+\xi\frac{x-\mu_1}{\sigma_1} > 0 \\ \frac{1}{\sigma_1} exp\left(-exp\left(-\frac{x-\mu_1}{\sigma_1}\right) - \frac{x-\mu_1}{\sigma_1}\right), \qquad if\ \xi = 0 \end{cases} \qquad (3-4)$$

where ξ is the shape parameter that controls the tail behavior of the distribution, μ_1 is a location parameter that is the central location of the distribution, and σ_1 is the scale parameter, which controls the spread of the distribution. The GEV curve shifts based on μ_1, and its spread is controlled by σ_1. Larger σ_1 values stretch the distribution wider, making it more spread out, while smaller values make it more concentrated. The overall shape of the curve depends primarily on ξ, which determines whether the tail behavior is heavy, exponential, or bounded. Figure 8-5 in Appendix (D-2) presents the probability histograms of the sphericity of all tested specimens, along with the fitted GEV distribution curves.

The values of Form histograms are best fitted with the Gamma distribution. The PDF of the Gamma distribution is defined as:

$$f(x,\kappa,\theta) = \frac{x^{\kappa-1}e^{-x/\theta}}{\theta^{\kappa}\Gamma(\kappa)} \quad for\ x > 0,\ \ \kappa > 0,\ \ \theta > 0 \qquad (3-5)$$

where κ and θ are the shape and scale parameters that control the shape and the spread of the distribution, respectively. The shape of the Gamma distribution varies significantly depending on κ; when $\kappa > 1$, the distribution exhibits right skewness with a peak, approaching the Normal

distribution for high values of κ. When $\kappa = 1$, it simplifies to the Exponential distribution, exhibiting a monotonic falling curve. For $0 < \kappa < 1$, the curve exhibits significant skewness, characterized by a pronounced ascent at zero and an extended right tail. The scale parameter θ controls the distribution's spread, with larger values of θ resulting in greater dispersion and smaller values leading to increased concentration. Figure 8-7, Appendix (D-4) shows the probability histograms of all tested specimens with the fitted Gamma distribution curves.

Roundness histograms were best fitted with the non-standardized Student's t-distribution. The PDF of the distribution is defined as:

$$f(x, \upsilon, \mu_2, \sigma_2) = \frac{\Gamma\left(\frac{\upsilon+1}{2}\right)}{\Gamma\left(\frac{\upsilon}{2}\right)\ \sigma_2\ \sqrt{\pi\,\upsilon}}\ \left(1 + \frac{1}{\upsilon}\left(\frac{x-\mu_2}{\sigma_2}\right)^2\right)^{-\frac{\upsilon+1}{2}} \qquad (3-6)$$

where μ_2 is the location parameter, which shifts the distribution along the x-axis; the scale parameter σ_2 determines the spread of the distribution; and the degrees of freedom υ controls the heaviness of the tails. As υ increases, the distribution's tails become thinner and the distribution approaches the normal distribution; while lower υ values result in heavier tails, indicating a higher likelihood of extreme values. With larger values of σ_2 causing broader curves and smaller values of σ_2 leading to a more concentrated peak. Figure 8-6 in Appendix (D-3) depicts the probability histograms of four representative specimens' Form with the fitted Gamma distribution curves. Table 3-2. Summarizes the morphology distribution parameters for the tested materials.

Table 3-2. Summary of statistical analyses of morphology of tested materials.

Material	Nth	Sphericity Parameters			Form Parameters		Roundness Parameters		
		μ_1	σ_1	ξ	κ	θ	υ	μ_2	σ_2
A01	356	2.18	1.11	0.27	10.57	0.04	60.07	0.91	0.13
A02	493	1.82	0.82	0.33	14.75	0.03	23.16	0.89	0.12
A03	685	2.60	1.64	0.46	8.26	0.05	27.52	0.90	0.14
A04	985	2.04	1.00	0.34	12.55	0.04	341.89	0.88	0.13
A05	1021	2.35	1.42	0.42	8.15	0.05	15.47	0.88	0.13
A06	466	2.10	1.15	0.50	9.25	0.05	11.63	0.91	0.12
A07	999	2.13	1.22	0.50	8.94	0.05	206.45	0.88	0.13
A08	532	2.08	1.18	0.53	8.32	0.05	7.10	0.90	0.12
A09	448	2.03	1.03	0.42	11.02	0.04	12.11	0.93	0.12
A10	266	2.24	1.17	0.39	10.64	0.04	14.50	0.92	0.12
A11	1184	2.11	1.11	0.35	11.08	0.04	7.70	0.90	0.11
A12	1907	2.21	1.12	0.32	12.06	0.04	341.89	0.89	0.12
A13	962	1.74	0.75	0.33	15.37	0.03	41.22	0.91	0.10
A14	1426	2.35	1.34	0.41	9.27	0.04	207.06	0.86	0.13
A15	180	1.63	0.69	0.42	14.39	0.04	18.79	0.93	0.12
A16	706	2.22	1.20	0.43	9.11	0.05	13.42	0.91	0.12
A17	431	2.27	1.23	0.41	9.32	0.05	25.46	0.92	0.13
A18	852	2.99	1.89	0.36	8.54	0.04	45.50	0.90	0.14
A19	205	2.12	1.09	0.33	12.90	0.04	3.34	0.95	0.10
A20	330	2.24	1.08	0.41	11.87	0.04	46.76	0.94	0.12

A21	283	2.01	0.95	0.37	11.64	0.04	23.55	0.92	0.12
A22	441	1.93	0.91	0.33	13.67	0.04	3.18	0.96	0.09
A23	281	1.85	0.85	0.34	14.82	0.03	9.00	0.97	0.10
A24	334	2.20	1.11	0.26	12.60	0.04	3.04	0.93	0.10
A25	267	1.62	0.63	0.34	18.03	0.03	20.40	0.93	0.10
A26	456	2.15	1.12	0.35	10.98	0.04	17.67	0.90	0.11
#1 Dry Glass Sand	1063	1.32	0.43	0.24	23.26	0.03	6.08	0.93	0.09
GS#40 Columbia Sand	1069	1.32	0.41	0.23	24.63	0.02	5.63	0.92	0.08
F-35 Ottawa Sand	712	1.55	0.44	0.14	37.71	0.02	9.02	0.96	0.07
Glass Beads	1240	1.32	0.41	0.23	24.63	0.02	2.00	0.97	0.02

3.4 Field Sensors reading results

3.4.1 Cell pressure readings:

The average daily results of the four cell pressures during 431 days (from August 14th, 2024, to October 19th, 2025) are presented in Figure 3-2. Earth pressure cell 1, located at a depth of 24.3 ft from the top of the wall, started reading approximately on the 60th day after installation (October 14th, 2025), whereas the readings of earth pressure cells 2 and 3, located at depths 19 ft and 11 ft respectively from the top of the wall, started recording data during the following 20 days with the progress of backfill placement. Earth pressure cell 4, located at a depth of 5 ft from the top of the wall, started reading during the first week of February 2025. For the first three earth pressure cells (cells 1 through 3), the pressure values initially increased as a result of fill work behind the wall, subsequently decreased, and then gradually increased with the increase of the fill height. On August 1st, 2025, all readings started decreasing. The results show oscillation in earth pressure values. The oscillation observed in the higher-capacity cells (170 kPa; Earth Pressure Cells 2 and 3) is greater than that recorded in the lower-capacity cells (70 kPa; Earth Pressure Cells 1 and 4).

The research team requested information about different stages of bridge construction and backfill placement. TDOT Engineer reported that the right lane deck was poured on April 2nd, 2025, the left lane deck was poured on April 17th, 2025, and both bridges were opened to traffic on June 9th -10th, 2025. The observed oscillation in the results may be attributed to localized point loading on the earth pressure cells, which likely arises from the angularity of the backfill material. As a result of this oscillatory behavior, polynomial fitting lines were applied to represent the earth pressure values for the cells as shown in Figure 3-3.

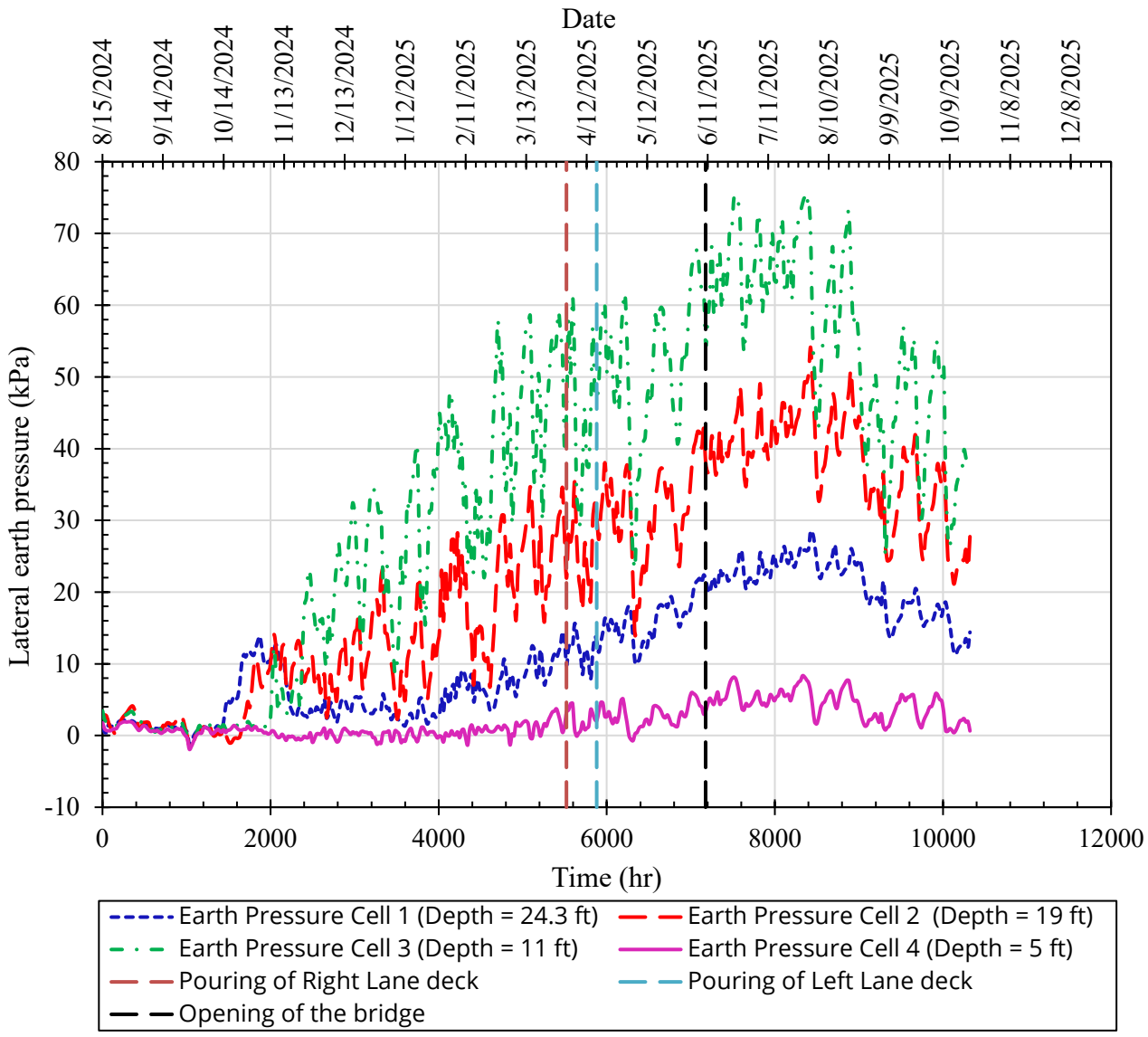

Figure 3-2. Lateral earth pressure versus time for the four earth pressure cells.

Figure 3-4. shows the development of the lateral earth pressure with time. The results indicate that the peak lateral earth pressure occurred at a depth ratio (D/H_{stem}) of approximately 0.37. After 418 days from the installation of the earth pressure cells, the final readings display that the maximum measured earth pressure reached about 3.5 times the theoretical at-rest earth pressure predicted by Rankine (1857) at the peak location. In contrast, the earth pressure near the wall toe showed to have decreased to approximately 0.60 of the theoretical at-rest value according to Rankine's theory.

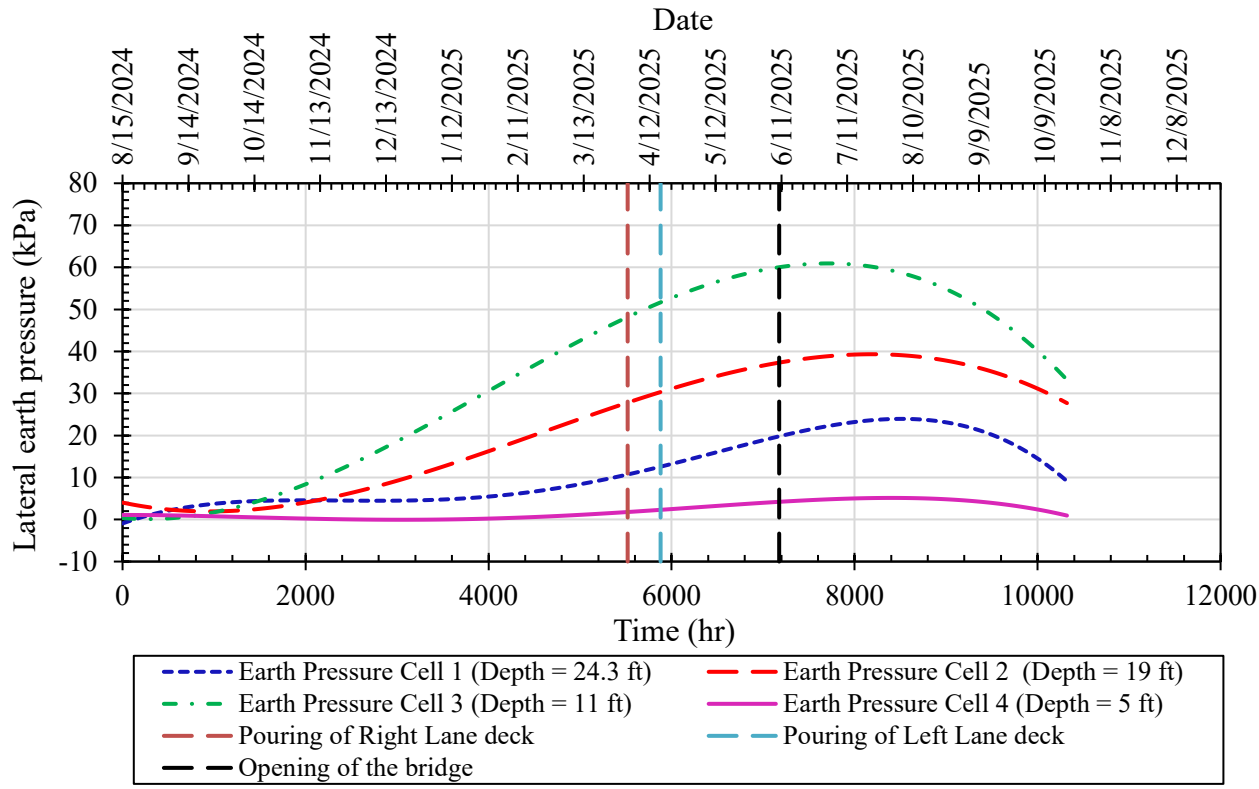

Figure 3-3. Fitted lateral earth pressure versus time for the four earth pressure cells.

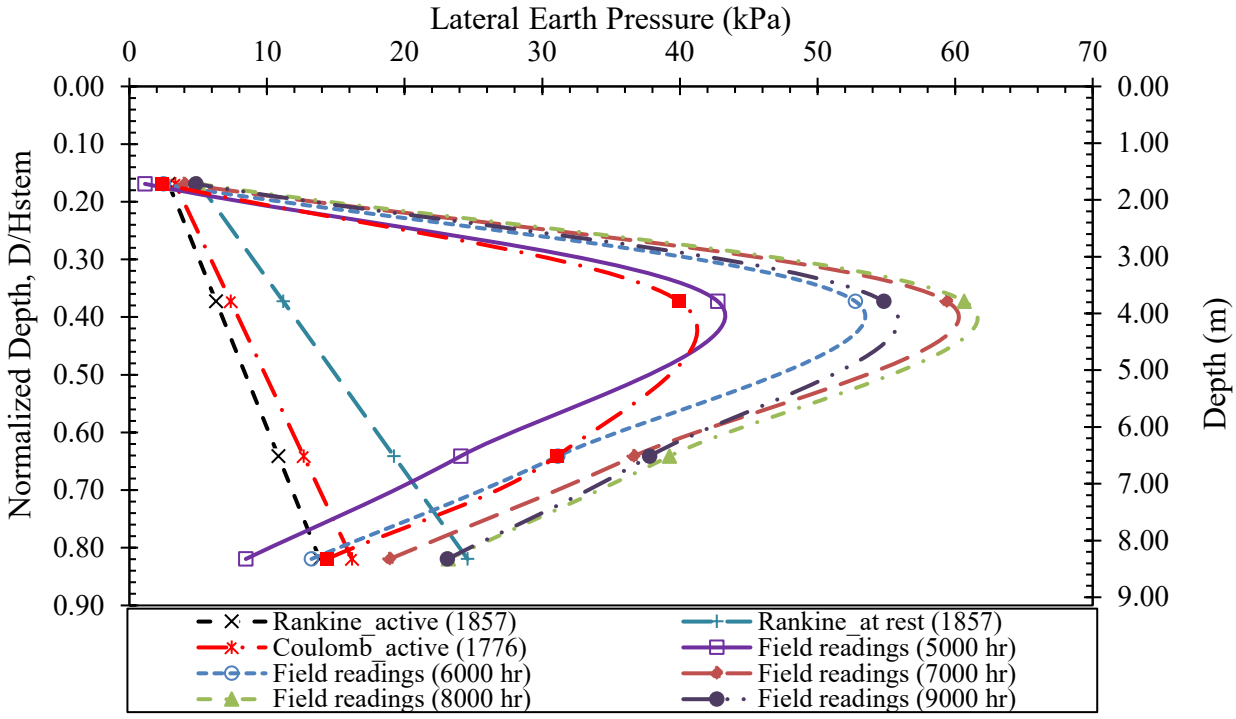

Figure 3-4. Development of the lateral earth pressure and the associated theoretical values along the wall height.

3.4.2 Tiltmeter and deformation-meter readings:

The tiltmeter was installed on August 14th, 2024, and the deformation meter was installed on February 17th, 2025, after reaching the target backfill level. The tiltmeter readings were analyzed utilizing both linear and polynomial fitting methods to calculate the rotation of the retaining wall stem. Referring to Figure 3-5, the results revealed a minimal rotation of the wall stem, suggesting that the backfill remained in an at-rest condition. Starting from the 7th month after construction (Early March 2025, after about 5000 hours), the rotation gradually increased in the active direction and reached an angle of approximately 0.14°. The deformation meter readings steadily increased to approximately 0.60 mm, then temporarily returned to their initial condition—likely due to nearby field activities—before resuming their original trend. The final measurement indicated a horizontal displacement in the active direction of approximately 0.85 mm, after which the readings began to oscillate. The research team believes that the tiltmeter data are more reliable, as the device was directly attached to the wall stem. Conversely, the deformation meter was anchored at both ends within the backfill material itself, which may have contributed to the observed oscillations, particularly given the small magnitude of the lateral displacements.

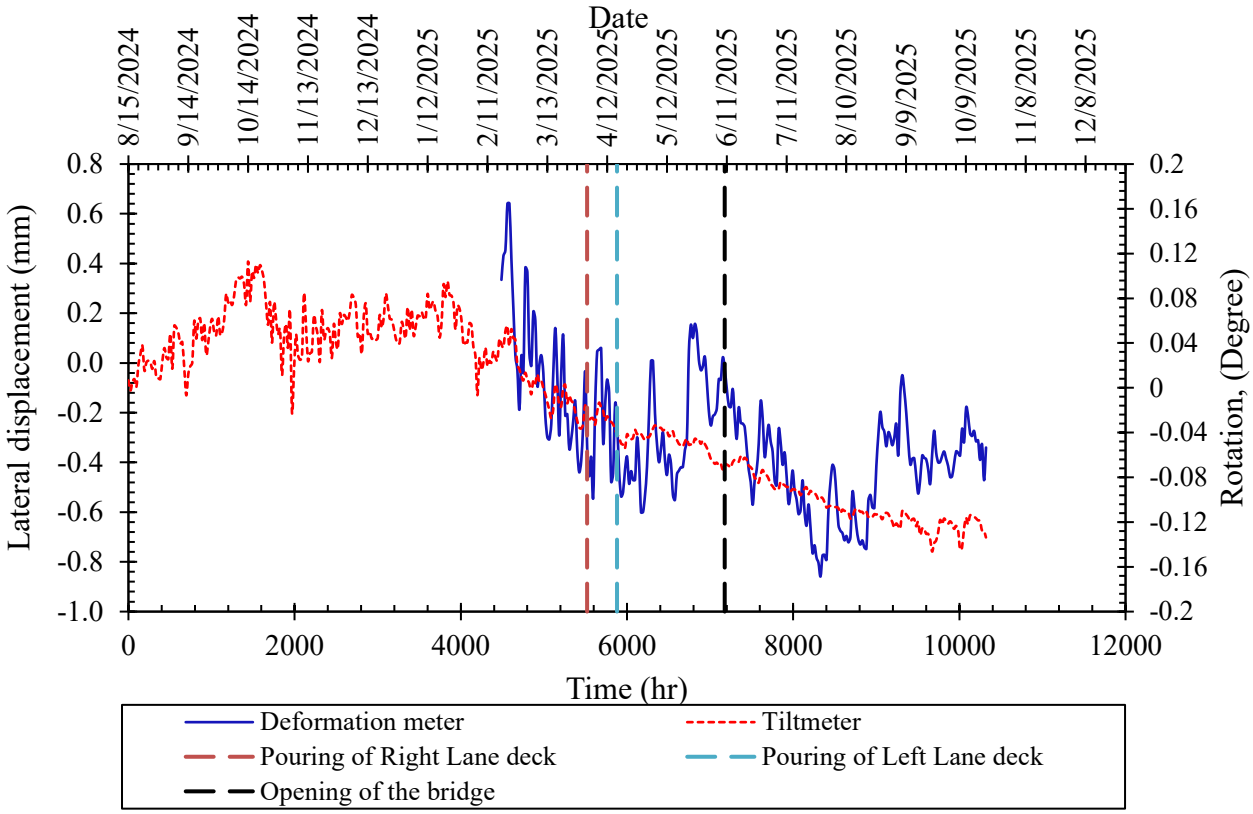

Figure 3-5. Rotation and horizontal displacement of the wall with time.

3.4.3 Interpretation of field measurements:

The field instrument readings were analyzed to evaluate the performance of the backfill material and the soil–structure interaction behavior over the monitoring period. Based on this analysis, the following key findings were identified:

- Oscillation of Earth Pressure Values
  - The earth pressure data exhibit measurable oscillations and the authors question the reliability of these sensors.
  - These fluctuations are more pronounced in the higher-capacity cells (170 kPa; Earth Pressure Cells 2 and 3) compared with the lower-capacity cells (70 kPa; Earth Pressure Cells 1 and 4).
- Effect of Construction Activities
  - There is no clear evidence that post-backfilling construction activities had significant effects on the earth pressure measurements.
- Reduction in Earth Pressure After August 1
  - The decrease in recorded earth pressures after August 1 may be due to the angularity of the backfill material.
  - High angularity increases particle interlocking, restricting relative particle movement.
  - This reduced internal mobility limits the ability of the soil mass to deform or mobilize lateral pressure, resulting in lower measured earth pressure values.
- Reliability of Deformation Measurements
  - The tiltmeter readings are considered more reliable, as the sensor was firmly fixed to the wall stem and directly captured the wall rotation.
  - The deformation meter, anchored within the backfill, is more susceptible to local soil movements, which likely contributed to the observed oscillatory behavior—particularly given the small magnitude of lateral displacements.

Chapter 4 Statistical Models for Shear Strength Parameters

4.1 Feature Selection and Regression Optimization Using Genetic Algorithms

Statistical linear and nonlinear regression models are developed to predict ϕ_p, ϕ_{cs} and ψ for both coarse and fine granular materials. Initially, twelve various predictors, including the eight morphology distribution parameters, σ_N, d_{50}, D_r, G_s were considered to be initial input data for the regression models. In the analysis, a genetic algorithm (GA) was employed to perform feature selection and reduce model overfitting in a regression context using ridge regression. The dataset was first imported from an Excel file with twelve predictor variables. Both the predictors and the response variable were standardized using z-score normalization to ensure that all variables contribute equally to the regression model and to satisfy the assumptions of ridge regression. The core of the analysis involved defining a custom fitness function (mseFitness) for the GA, which evaluates the performance of a subset of predictors by computing the Mean Squared Error (MSE) of the ridge regression model trained on that subset. To determine the optimal regularization parameter (k) for ridge regression, the function iteratively tested values logarithmically spaced between 0.001 and 1000, selecting the value that minimized the MSE. Consequently, to avoid overfitting and promote model simplicity, a complexity penalty proportional to the number of selected predictors was added into the MSE. The GA was configured with a binary selection mechanism, where each individual in the population represents a subset of predictors. Optimization parameters such as population size, crossover rate, and mutation function were carefully selected to ensure efficient convergence. Upon completion, the GA returned the best subset of predictors that yielded the lowest penalized MSE, thereby effectively balancing model accuracy and complexity. This approach not only enhanced the predictive performance of the regression model but also identified the most relevant features contributing to the response variable.

4.2 Statistical model for the critical state friction angle

The GA results identified $d_{50}, \sigma_R, D_r, and\ \sigma_N$ as the most influential predictors affecting the predicted ϕ_{cs}. To model this relationship, various linear and nonlinear regression models were tried, including exponential, power, logarithmic, and polynomial forms. Among these, the power model as presented in Eq. (4-1) demonstrated the highest predictive accuracy, evidenced by the highest coefficient of determination (R^2), indicating a strong correlation between the selected predictors and ϕ_{cs}. Table 4-1 summarizes the results of the multi variable statistical model for ϕ_{cs}, p-value for all variables are less than 5%, signaling that all predictors have a significant effect on the regression model. According to Equation 8, the ϕ_{cs} raised with the increase of d_{50}, σ_R, and D_r, highlighting the significant influence of particle roundness and relative density on shear strength behavior, as well as the positive correlation between them. In contrast, ϕ_{cs} decreases with increasing σ_N, reflecting the typical stress-dependent reduction in interparticle friction under higher confining pressures. Figure 4-1(a) shows a comparison between the experimental and model

prediction of ϕ_{cs} for both fine and coarse granular materials.

$$\phi_{cs} = 20.94 + 91.35 \left[\frac{(d_{50})^{0.26} (\sigma_R)^{0.43} (D_r)^{0.11}}{(\sigma_N)^{0.159}}\right] \quad (4-1)$$

Table 4-1. Results of the multivariable statistical model for ϕ_{cs}.

Predictor	Estimated Coefficients	Standard error (SE)	t-Statistic (tstat)	P value
Statistical constant (1)	20.94	1.42	14.765	6.74×10^{-36}
Statistical constant (2)	91.35	8.146	11.209	6.79×10^{-24}
σ_N	-0.159	0.011	-14.445	8.45×10^{-35}
d_{50}	0.264	0.023	11.398	1.64×10^{-24}
σ_R	0.434	0.047	9.191	1.56×10^{-17}
D_r	0.114	0.010	11.269	4.34×10^{-24}

4.3 Statistical model for the dilatancy angle (ψ)

The ψ values for fine granular materials at loose state were excluded from the development of the regression model, as materials in a loose state are expected to exhibit contraction rather than dilative behavior. The GA results identified θ, D_r, σ_N, and d_{50} as the primary predictors influencing ψ. Among the various models evaluated, the multi-linear regression model incorporating interaction and logarithmic terms; as defined in Eq. (4-2) demonstrated the highest predictive accuracy and achieving the highest R^2.

Table 4-2 summarizes the results of the multi variable statistical model for ψ, p-values for all variables are less than 5% indicating that all predictors have a significant effect on the regression model. Figure 4-1(b) depicts a comparison between the experimental measurements and model prediction for ψ for both fine and coarse granular materials.

$$t\psi = 9.84 - 46.23\,\theta + 19.12\,D_r - 2.5\,Ln\,(\sigma_N) - 0.01\,\sigma_N\,Ln\,(d_{50}) \quad (4-2)$$

Table 4-2. Results of the multivariable statistical model for ψ.

Predictor	Estimated Coefficients	Standard error (SE)	t-Statistic (tstat)	P-value
Statistical constant (1)	9.84	1.138	5.888	3.11×10^{-08}
θ	-46.23	0.018	4.273	3.68×10^{-05}
D_r	19.12	1.112	17.429	6.22×10^{-36}
$Ln(\sigma_N)$	-2.51	0.133	-18.816	4.71×10^{-39}
$\sigma_N\ x\ Ln\ (d_{50})$	-0.011	0.0007	-14.609	2.80×10^{-29}

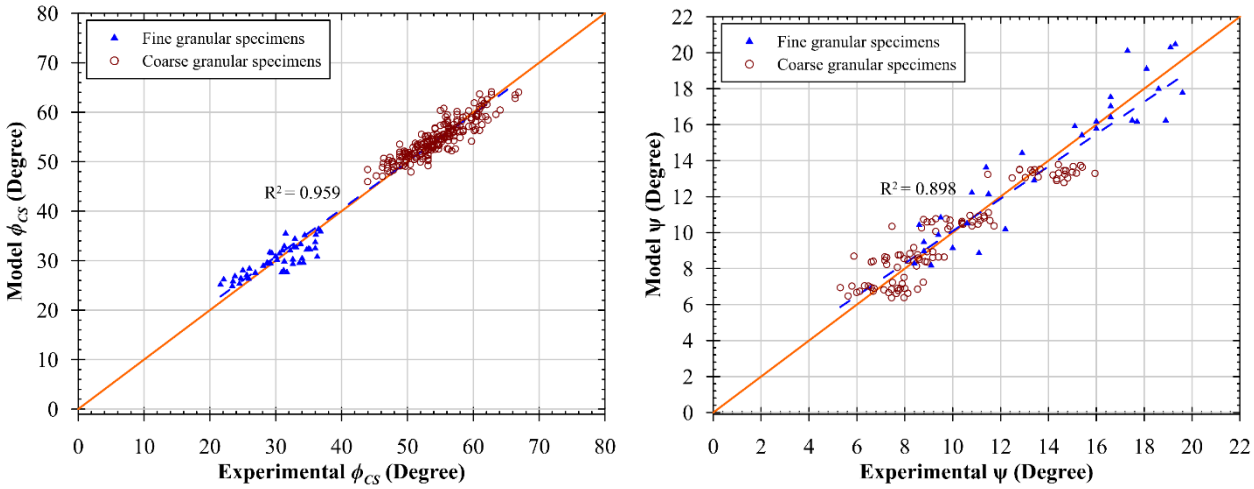

Figure 4-1. Experiments versus model predictions for (a) critical state friction angle (ϕ_{cs}); (b) dilatancy angle (ψ).

4.4 Statistical models for the peak state friction angle

Several studies have examined the relationship between ϕ_{cs} and ϕ_p to better understand the strength properties of granular materials. Wood (1990) emphasized that the difference between ϕ_p and ϕ_{cs} is primarily influenced by dilatancy, which is governed by D_r and confining pressure for triaxial experiments or normal stress for direct shear experiments. Bolton (1986) developed a widely accepted empirical statistical model relating the increase in ϕ_p to a dilatancy index based on D_r and mean effective stress for triaxial experiments. Tatsuoka (1987) criticized Bolton's (1986) model for ignoring the anisotropic behavior of sand caused by preferred deposition direction (fabric effect) during specimen preparation, emphazing the importance of incorporating fabric influence in any model describing friction and dilatancy properties of granular materials. Furthermore, Chakraborty and Salgado (2010) stated that the Bolton (1986) model does not capture sand behavior well for low confining pressure and proposed a modified version of Bolton (1986) model. Hasan and Alshibli (2010) found that Bolton's (1986) model fails to capture the behavior of very angular granular materials tested under very low confining pressure and proposed a new statistical model.

Rothenburg and Kruyt (2004) advanced the understanding of granular shear behavior by implementing digital image correlation and discrete element modeling to investigate particle-scale mechanics. Their study revealed that the evolution of both the peak and critical state friction angles is governed by distinct mechanisms. ϕ_{cs} is closely associated with the development of interparticle contact fabric and coordination number, whereas the peak friction angle ϕ_p , is more sensitive to the initial packing arrangement and boundary constraints. This distinction underscores the significance of micro-structural evolution and stress history in controlling the macroscopic shear response of granular materials. In this report, two different nonlinear regression model for ϕ_p are proposed based on the nonlinear regression model developed by Hasan and Alshibli (2010). In these models (Eq. 4-3& 4-4), the morphology parameters sphericity, location parameter (μ_1), and roundness scale parameter (σ_2) were used to predict ϕ_p and both models yielded higher R^2 values. In the first model (Eq. 4-3), ϕ_p increased with the decrease of μ_1, while in the second model (Eq. 4-4), ϕ_p increased with the increase of σ_2. Figure 4-2 shows a comparison between the experimental

results and the model's prediction for ϕ_p for both models.

$$\phi_p = \phi_{cs} + 16\left[\frac{(D_r)^{0.90}}{(\sigma_N)^{0.10}(\mu_1)^{0.55}}\right] \quad (4-3)$$

$$\phi_p = \phi_{cs} + 16\left[\frac{(D_r)^{0.90}(\sigma_2)^{0.167}}{(\sigma_N)^{0.10}}\right] \quad (4-4)$$

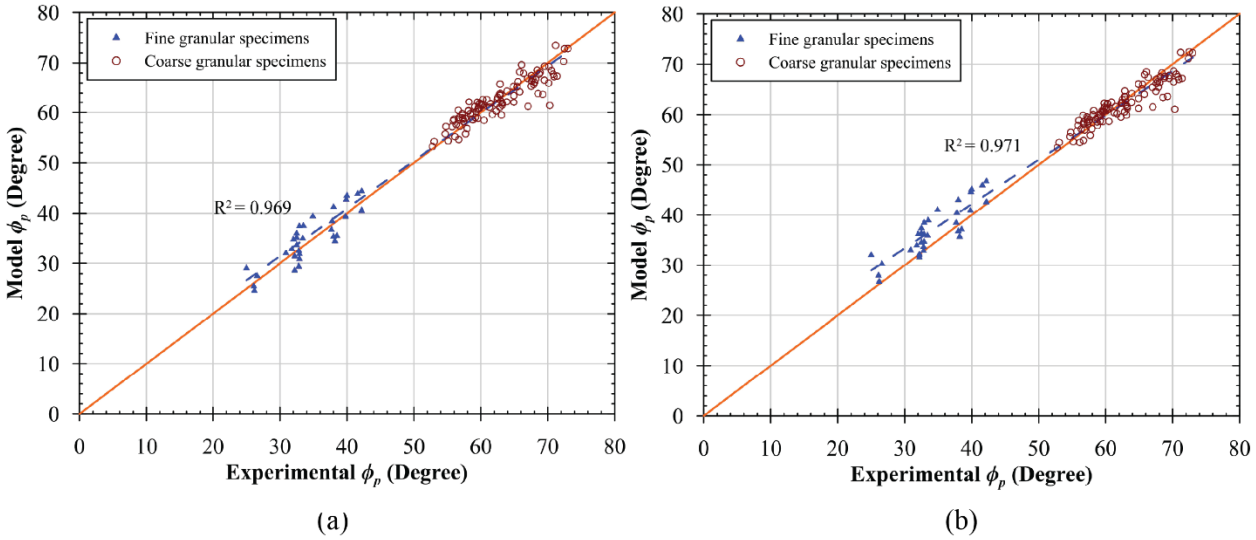

Figure 4-2. Experiments versus model predictions for the peak state friction angle (ϕ_p) (a) model with roundness scale (σ_2); (b) model with sphericity location (μ_1).

Chapter 5 Failure Wedge Behind The Retaining Walls.

The volume of backfill materials behind the retaining wall is determined based upon the active failure wedge behind the retaining wall. The active failure wedge is defined as the active soil mass located behind the retaining wall, that is assumed to move as a rigid body when the wall undergoes sufficient lateral displacement to mobilize shear strength along a planar or curved failure surface. In classical earth pressure theories (e.g., Coulomb and Rankine theories), the soil behind the wall is idealized as a triangular wedge bounded by the following factors: the back face of the wall, the ground surface, and a planar failure surface inclined at an angle determined by the soil's shear strength parameters. When the wall moves away from the backfill, the soil mobilizes active earth pressure, and the wedge tends to slide downward and outward. When the wall moves toward the backfill, the wedge develops passive earth resistance. The geometry and the shear strength along the failure surface govern the magnitude of the lateral earth pressure exerted on the wall.

5.1 Numerical Models

The finite element (FE) method was used to assess the performance of retaining walls and to determine the geometry of the failure wedge. Two constitutive models were used in this study. The first one is the classic Mohr-Coulomb (MC) model, and the second model was originally developed by Lade and Kim (1988) and later extended by Alsaleh et al. (2006), as it offers a more advanced constitutive model for granular materials.

5.1.1 Mohr-Coulomb (MC) constitutive model

The behavior of the aggregate behind the retaining wall was modeled using the Mohr-Coulomb constitutive model. Table 1 summarizes the model parameters based on the previous experimental results and the elastic properties of the concrete. ϕ_{cs} , and ψ derived (LSDS) and (LTX) tests for A26 were fitted to determine the appropriate values for the actual retaining wall. Based on the fitting equations presented in Figure 7, the selected values for ϕ_{cs} and ψ were 50.5° and 8.8°, respectively.

Table 5-1. Fill aggregate and concrete properties used in the FE analysis.

Aggregate Properties	
Soil mass density (kN/m^3)	16.05
Young's Modulus (kPa)	117647
Poisson's ratio	0.22
Angle of internal friction (ϕ)	50.5^o
Dilatancy angle (ψ)	8.8 ^{o}
Concrete Properties	
Mass density (kN/m^3)	24.52

Young's Modulus (kPa)	2.46×10^7
Poisson's ratio	0.20

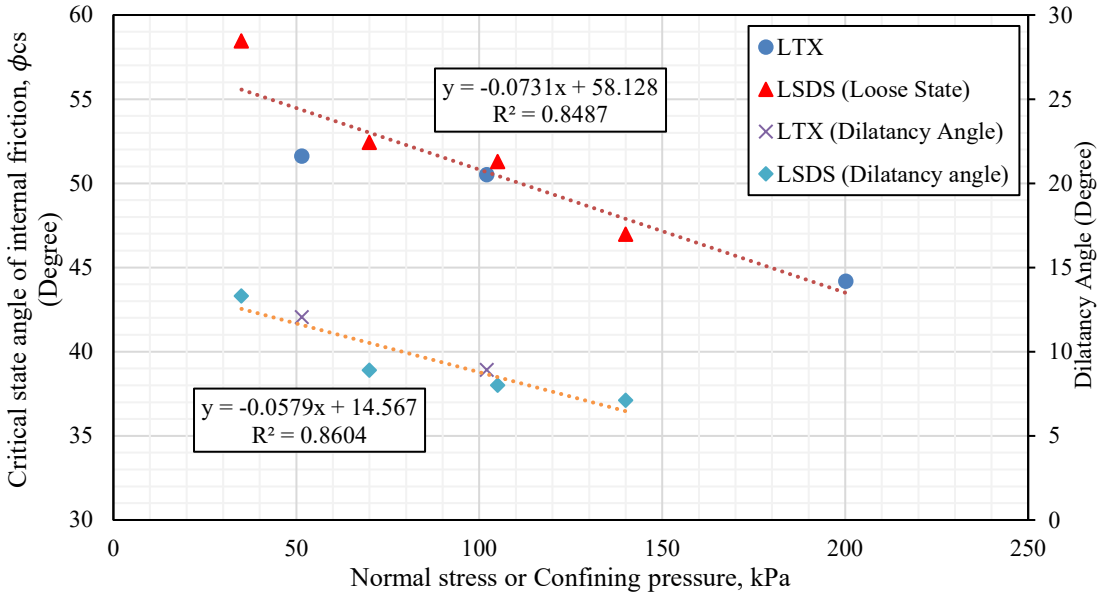

Figure 5-1. Values of critical state internal angle of friction and the dilatancy angle for A26 with both shear tests.

Modes of failure of the cantilever retaining wall

Three different modes of failure were selected to determine the active failure wedge behind the retaining wall (Figure 5-2). In the first mode (Figure 5-2(a)), failure occurs due to translational sliding of the wall. In the second mode ((Figure 5-2(b)), the wall experiences stem rotation about a point above the base. In the third mode ((Figure 5-2(c)), failure is characterized by full rotation of the wall about its toe.

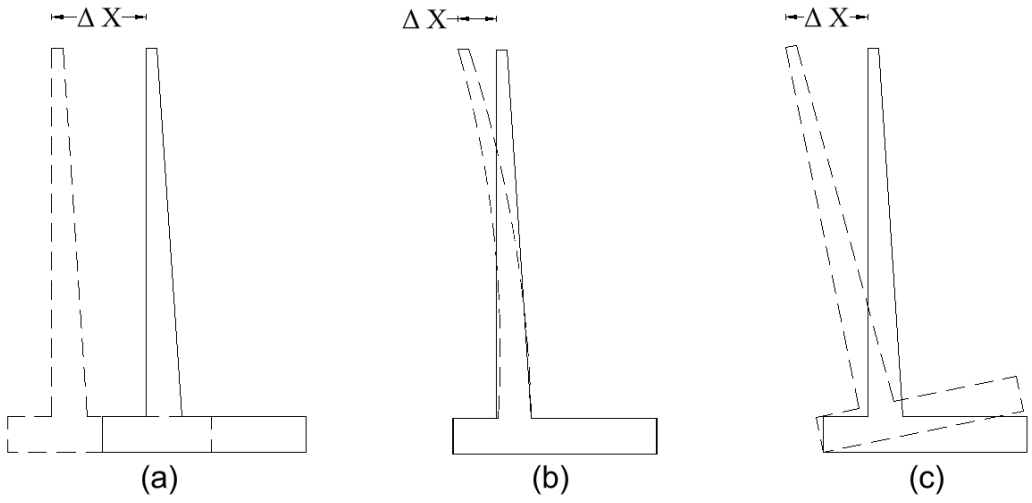

Figure 5-2. The different transition modes of the retaining wall: (a) Horizontal translation mode; (b) stem rotation mode; (c) full rotation mode.

Model geometry, mesh, and boundary conditions

The finite element model was created utilizing ABAQUS software, employing a plane strain geometry to replicate the cantilever retaining wall aformentioned in Section 2.3 **Error! Reference source not found.**. The design has a cantilever retaining wall measuring 11.18 m in height. Figure 5-3 displays the cross-section of the wall. The footing measures 5.64 m in width, and the stem is inclined, with the thickness varying from 0.30 m at the top to 0.98 m at the bottom. An unstructured mesh was generated using 4-node bilinear plane strain quadrilateral (CPE4R) elements with reduced integration, and enhanced mesh refinement was applied along the wall-soil interface to effectively capture stress gradients (CPE3 - A 3-node linear plane strain triangle). The computational domain extended twice the wall height to mitigate boundary effects. The bottom boundary for the soil was fixed to restrict any vertical and horizontal displacements, while the side boundaries were set as rollers to allow vertical movement but to prevent horizontal displacement. The top backfill surface was free to deform to simulate realistic loading conditions, Figure 5-3 shows the model geometry. For the first failure mode ((Figure 5-2(a)), a horizontal displacement of 12.5 mm was applied uniformly along the stem of the retaining wall to induce sliding. For the second failure mode ((Figure 5-2(b)), horizontal displacements of 12.5 mm and 40 mm were applied at the top of the wall to simulate rotation of the stem. Similarly, for the third failure mode ((Figure 5-2(c)), horizontal displacements of 12.5 mm and 40 mm were applied at the top of the wall to represent full rotation about the base. In all cases, a uniform surcharge load of 50 kPa was applied at the backfill surface.

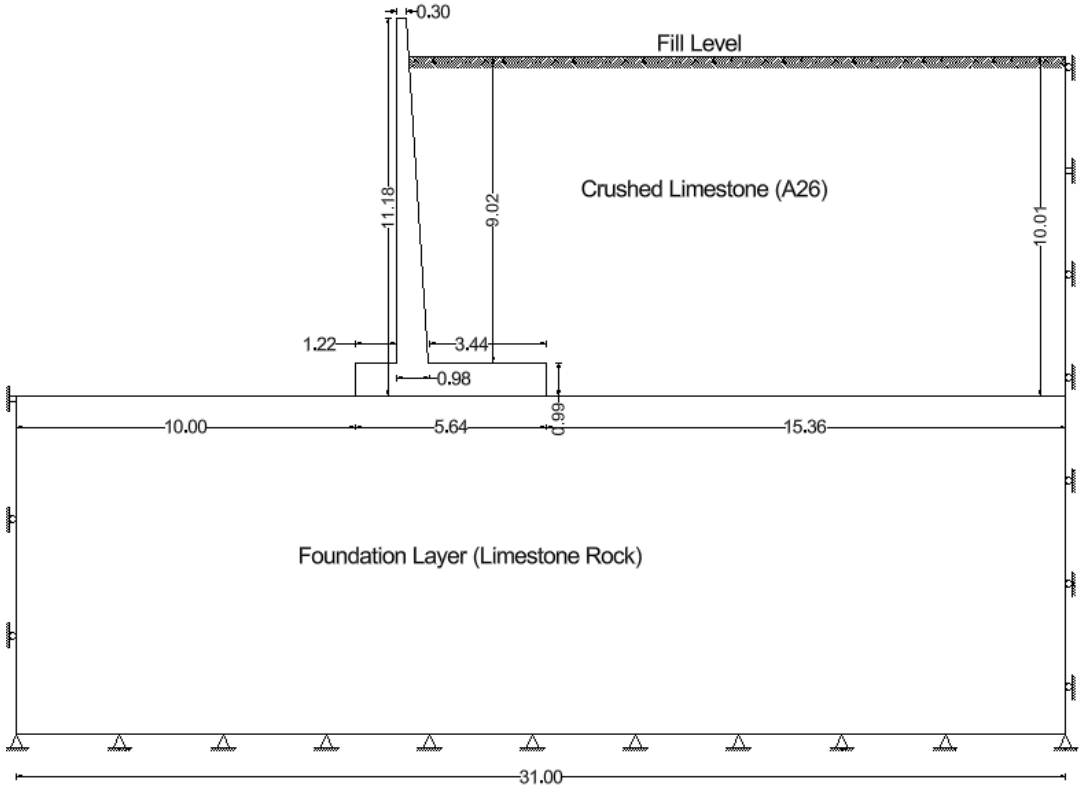

Figure 5-3. The FE Model Geometry and boundary conditions.

Model results and discussion

For the first mode of failure (Figure 5-4 (a)), the results indicate that the shear plane initiates at the bottom corner of the retaining wall heel and propagates upward at an inclination angle of approximately 67°. For the second mode of failure, the initiation point and inclination of the shear plane depend on the magnitude of the applied horizontal displacement, with the inclination angle increasing from about 47° at a displacement of 12.5 mm (Figure 5-4 (b)) to approximately 66° at 40 mm (Figure 5-4 (c)). For the third mode of failure (Figure 5-4 (d)), multiple shear planes develop where the first shear plane originates at the wall–soil interface at the base and propagates nearly vertically, while a second plane forms along the wall stem and extends upward at an inclination angle of about 64°. In addition, part of the soil resting on the heel of the wall rotates together with the wall, reflecting the more complex deformation pattern associated with this failure mechanism.

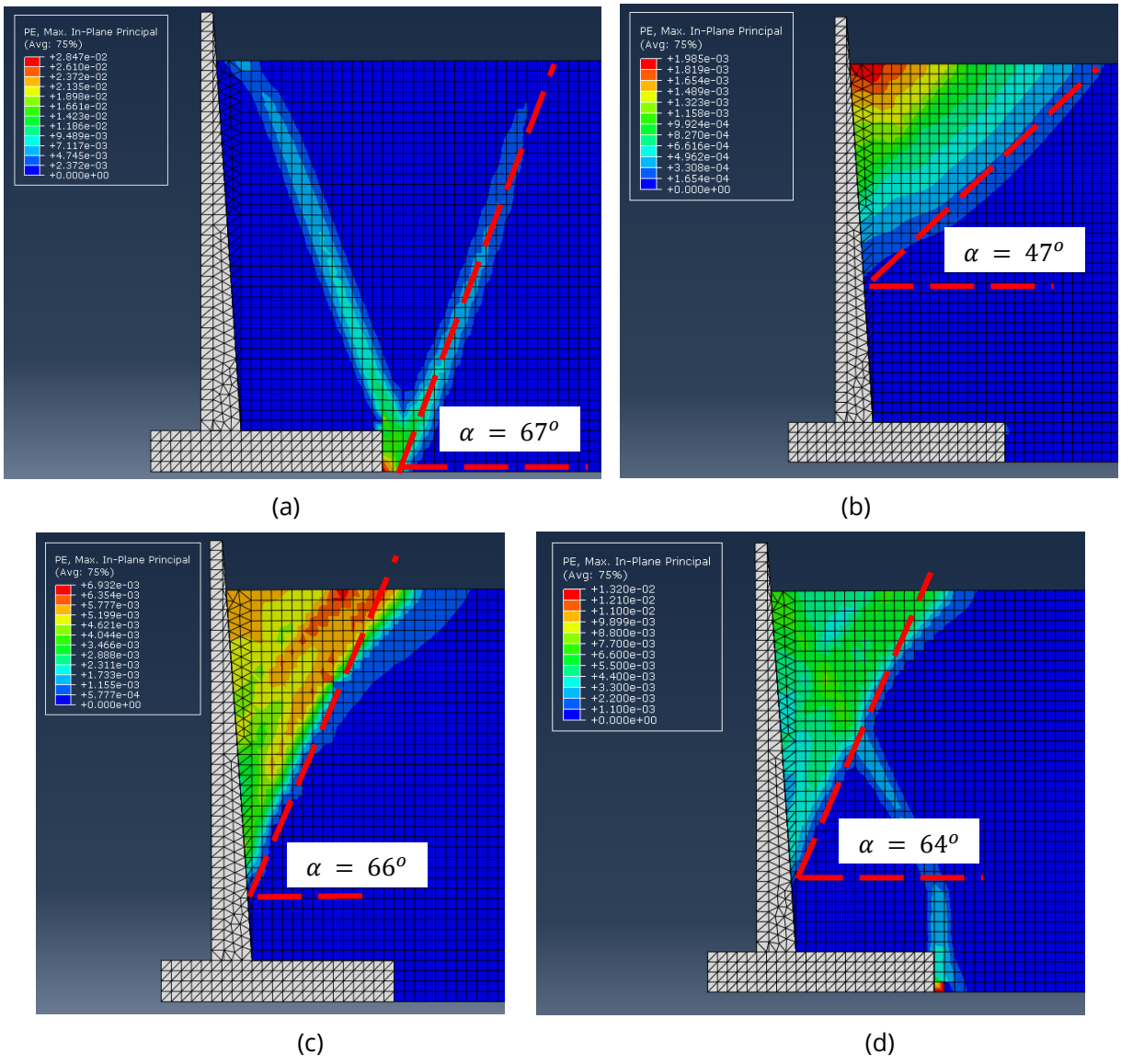

Figure 5-4. The plastic shear strain through the backfill: (a) Horizontal translation mode; (b,c) stem rotation mode; and (d) full rotation mode.

The results of the active failure wedge of the three modes of failure demonstrates that the critical active failure wedge corresponds to the first mode of failure (Horizontal translation mode), Figure 5-5 displays the angle of the active failure wedge (α) at different ϕ_{cs} varied from (50.5° to 65°), α varied from 67° to 69°.

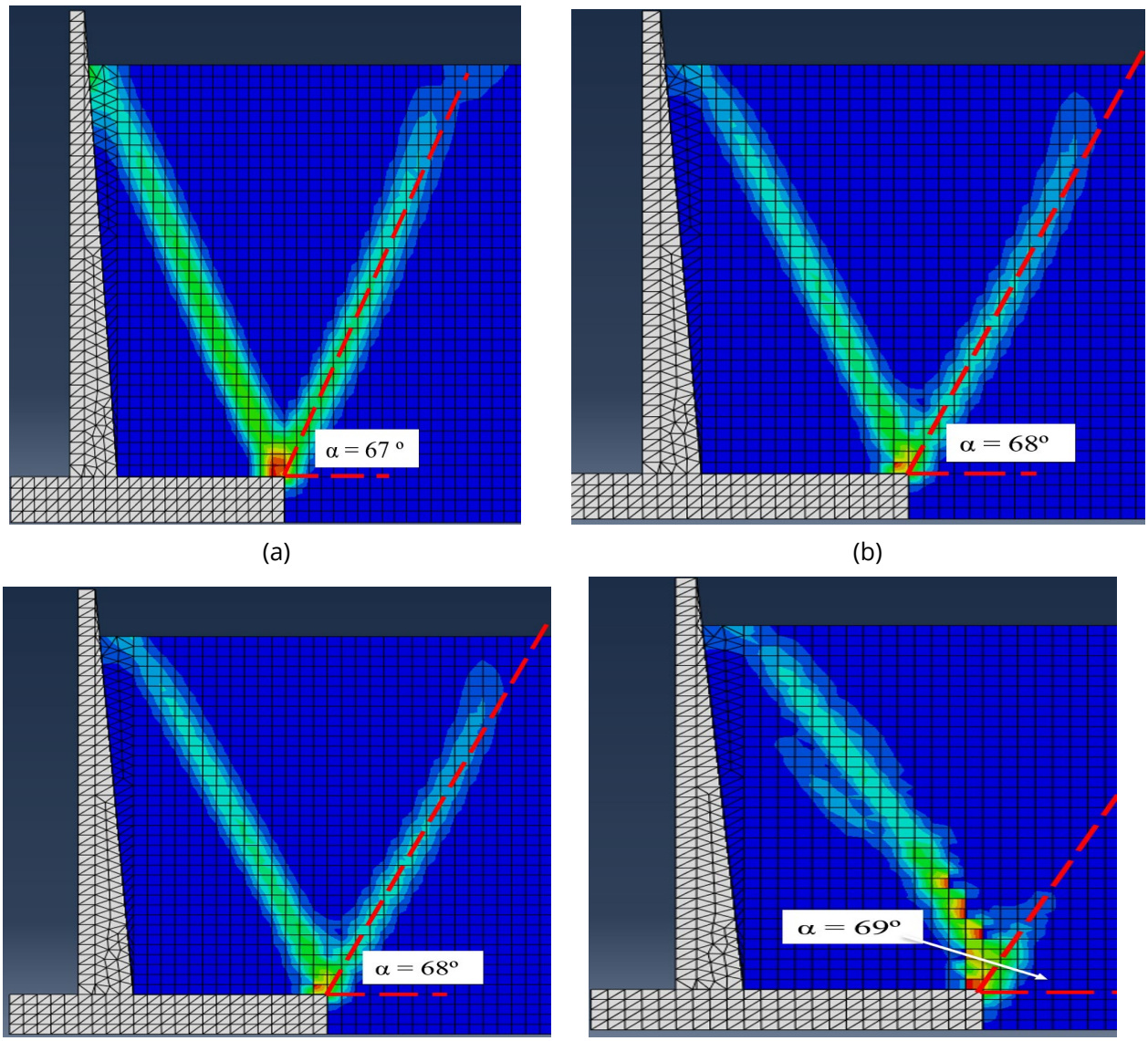

(a) (b)

(c) (d)

Figure 5-5. Failure surface with horizontal translation (sliding) modes of movement at different values of angle of internal friction (ϕ_{cs}): (a) $\phi_{cs} = 50.5^o$; (b) $\phi_{cs} = 55^o$; (c) $\phi_{cs} = 60^o$; and (d) $\phi_{cs} = 65^o$.

5.1.2 Lade's constitutive model upgraded by Alsaleh et al. (2006)

The constitutive model is based on the stress–strain formulation originally proposed by Lade and Kim (1988) for frictional granular materials. The model is founded on a multi-surface plasticity framework that uses the Lade–Duncan failure criterion, which represents the failure surface as a function of the first and third invariants of the stress tensor. This formulation captures

the nonlinear, pressure-dependent behavior of granular soils more effectively than classical Mohr–Coulomb models. The model was later extended by (Alsaleh et al. 2006; Alshibli et al. 2006) by implementing Cosserat theory which enables rotation degrees of freedom. When integrated into a Cosserat continuum framework, the model gains the ability to simulate strain localization, shear band formation, and micro-rotation effects, providing a more realistic representation of granular material behavior at both the macro- and micro-scales. Table 5.2 summarizes the model parameters that were determined by the results of LTX tests performed on A26 aggregate as mentioned in section 3.2 . Additional details regarding the determination of the model parameters can be found in (Alsaleh 2004)

Table 5-2. Constitutive Parameters for Lade's Model.

Parameter	Value	Parameter	Value
M_L	8.26	h	0.55
λ	0.32	α_o	0.75
m	0.70	C	6.60 x 10^{-4}
η_1	329.27	P	0.9538
ψ_2	-3.73	b	0.75
μ	2.0		

5.1.3 Model results

The results presented in Figure 5-6 demonstrate that the angle of the active failure wedge is approximately 65° which is consistent with the predictions of the classical Mohr–Coulomb constitutive model.

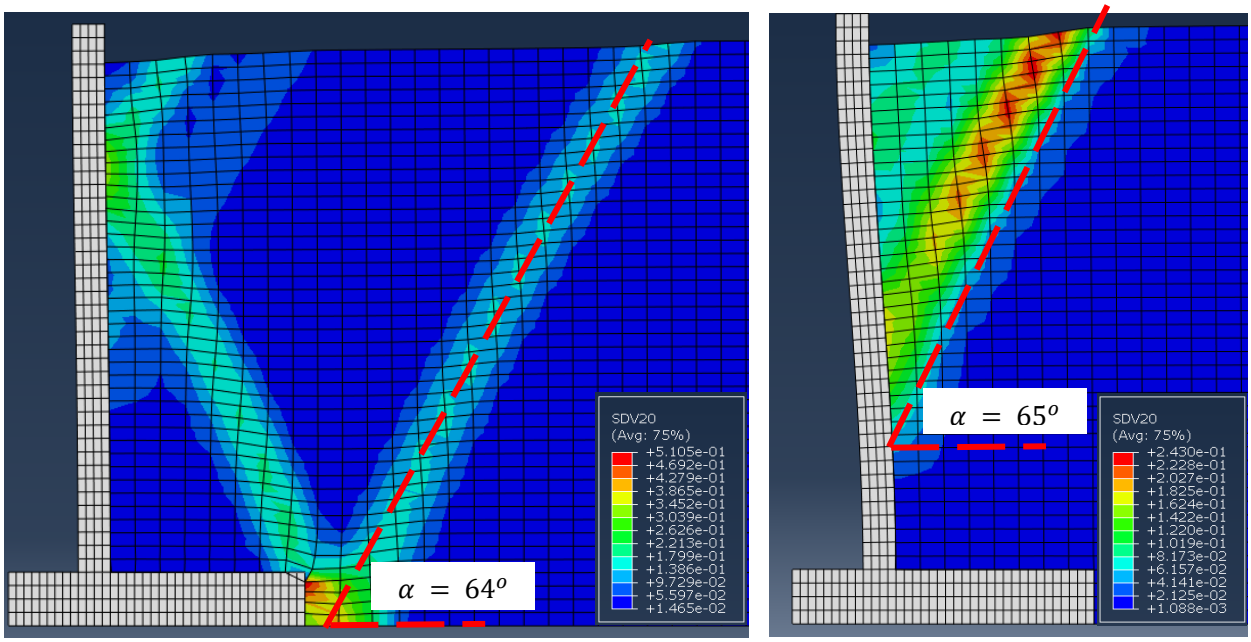

(a) (b)

Figure 5-6. Failure surface with a horizontal translation (sliding) mode of movement according to Alsaleh et al. (2006) constitutive model: (a) Horizontal translation mode; (b) stem rotation mode.

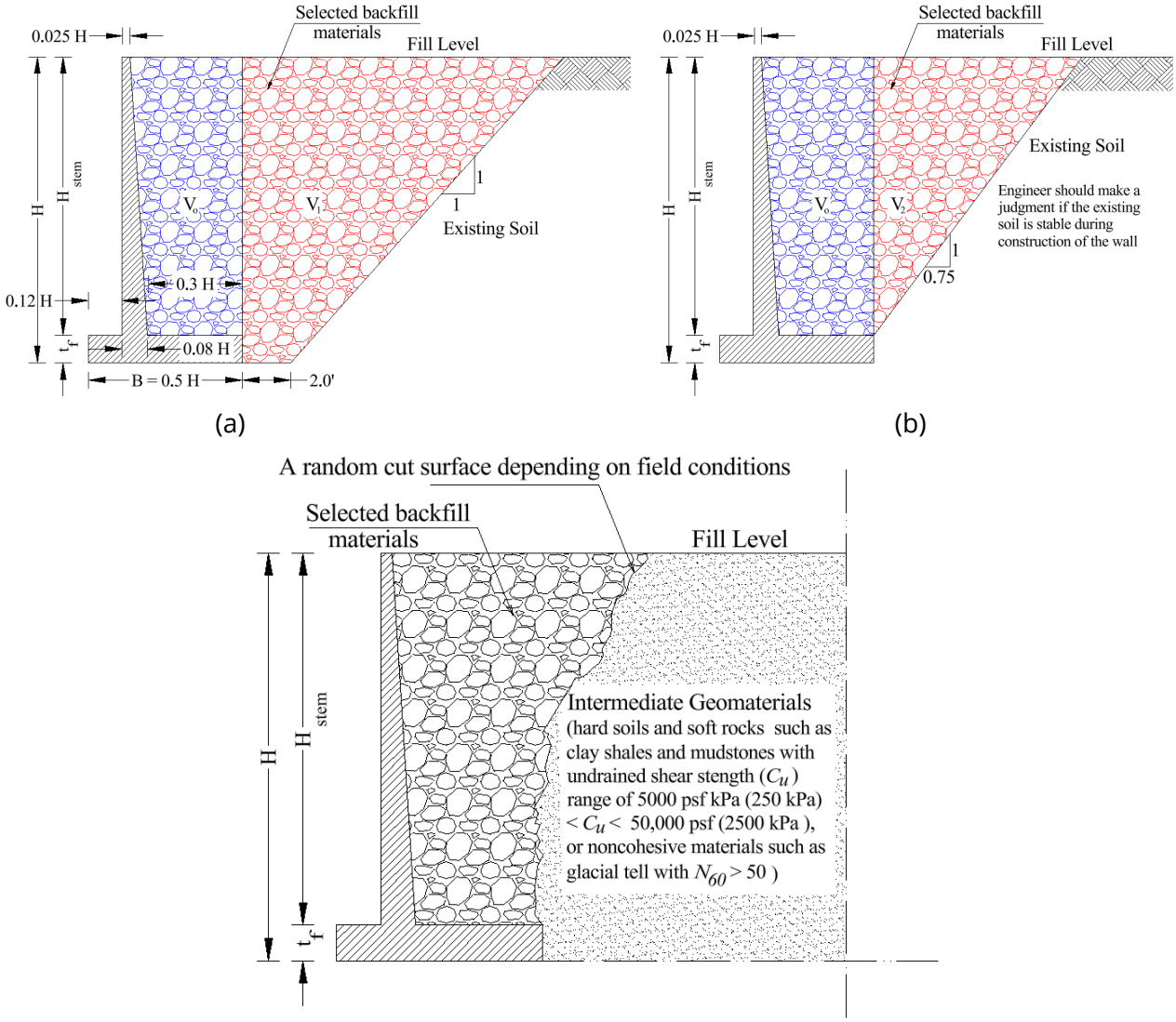

Figure 5-7. The backfill material behind the retaining wall according to (a) current guidelines; (b) new proposed guidelines; (c) the case of intermediate geomaterials.

5.2 Cost analysis for the new guidelines

The FE results demonstrate that the slope of the backfill materials according to the current guidelines (1:1) is very conservative, and that a steeper slope (0.75H:1V) will achieve a safe and economical design according to (Subpart P-Appendix B- (OSHA)) and soil type (A) (Subpart P-Appendix A- (OSHA)). According to the current guidelines (Figure 5-7(a)), the backfill starts 2.0 ft horizontally from the heel of the wall, then rises with a 1:1 slope until it reaches the ground surface. Assuming the ground surface is level, the volume of backfill material can be calculated according to Equations (5-1, 5-2, 5-3) as follows:

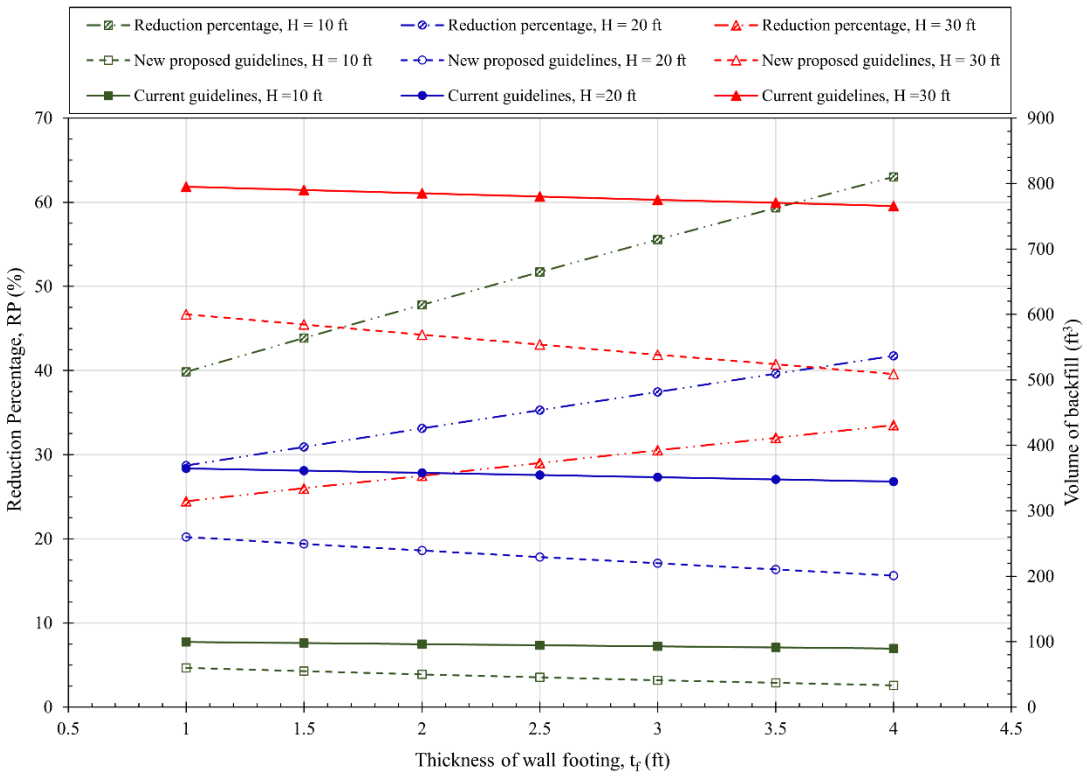

Figure 5-8. The volume of backfill materials and the reduction percentage at different wall heights.

$$V_{Current\ guiedlines} = V_o + V_1 \qquad (5-1)$$

$$V_o = \frac{1}{2}(0.08\ H - 0.025\ H)(H\ -\ t_f) + 0.3\ H\ (H\ -\ t_f) \qquad (5-2)$$

$$V_1 = \frac{1}{2}(\ H\ + 2)^2 - \ 2 \qquad (5-3)$$

Where V_o is the volume of backfill material resting on the wall heel, the footing dimensions are assumed as a percentage of the height of the retaining wall (H, Figure 5-7(a), base width = 0.5 H, toe projection = 0.12 H, heel projection = 0.30 H, stem thickness at the top = 0.025 H, stem thickness at bottom = 0.08 H), which approximately matches TDOT drawing, and t_f is the thickness of the base of the retaining wall. Figure 5-7(b) shows the proposed guidelines where the backfill material begins at the top of the retaining wall's heel and rises with a 0.75H:1V slope until it reaches the ground surface. Assuming the ground surface is level, the volume of backfill material can be calculated as follows:

$$V_{New\ proposed\ guiedlines} = V_o + V_2 \qquad (5-4)$$

$$V_2 = 0.375\ (\ H - \ t_f\ )^2 \qquad (5-5)$$

If geomaterials classified as intermediate geomaterials, which include hard soils and soft rocks such as clay shales and mudstones with undrained shear strength (C_u) in the range of of 5,000 psf (250 kPa) < C_u < 50,000 psf (2500 kPa), or noncohesive materials such as glacial till with N60 > 50, the geomaterial is strong and stable, and it is proposed that the design shown Figure

5-7(c) be adopted. The volumes of backfill material for different wall heights (H), and thickness of the base (t_f) calculated according to both the current guideliens and the newly proposed guidelines, are summarized in Figure 5-8 where the reduction percentage is calculated as:

$$Reduction\ percentage\ RP\% = \frac{V_{current\ guidelines} - V_{new\ proposed\ guidelines}}{V_{current\ guidelines}}\ X\ 100 \qquad (5-6)$$

Table 5-3 summarizes the volumes of backfill material for three different wall heights (H) and varying t_f, as calculated using both the current and the newly proposed guidelines. The results show that at H = 10 ft, the backfill volume is reduced by 39% to 63% depending on t_f. For H = 20 ft, the reduction ranges from 28% to 41% whereas at H = 30 ft, it ranges from 24% to 33%. Figure 5-8 provides a graphical comparison of the backfill volumes derived from both guidelines across different H and t_f.

Table 5-3. The volume of backfill materials and the reduction percentage at different H and t_f.

	t_f (ft)	V_o (ft^3)	V (New proposed guidelines) (ft^3)	V (Current guidelines) (ft^3)	RP (%)
H = 10 ft	1.0	29.48	59.85	99.48	39.83
	1.5	27.88	54.93	97.84	43.85
	2.0	26.20	50.20	96.20	47.82
	2.5	24.56	45.66	94.56	51.72
	3.0	22.93	41.30	92.93	55.56
	3.5	21.29	37.13	91.29	59.32
	4.0	19.65	33.15	89.65	63.02
H = 20 ft	1.0	124.45	259.83	364.45	28.71
	1.5	121.18	249.52	361.18	30.91
	2.0	117.90	239.40	357.90	33.11
	2.5	114.63	229.47	354.63	35.29
	3.0	111.35	219.73	351.35	37.46
	3.5	108.08	210.17	348.08	39.62
	4.0	104.80	200.80	344.80	41.76
H = 30 ft*	1.0	284.93	600.30	794.93	24.48
	1.5	280.01	584.61	790.01	26.00
	2.0	275.10	569.10	785.10	27.51
	2.5	270.19	553.78	780.19	29.02
	3.0	265.28	538.65	775.28	30.52
	3.5	260.36	523.71	770.36	32.02
	4.0	255.45	508.95	765.45	33.51

* The same slope 0.75:1 is assumed to be safe with H = 30 ft according to OSHA guiedlines (Subpart P-Appendix B- (OSHA)), Sloping or benching for excavations greater than 20 feet deep shall be designed by a registered professional engineer.

Chapter 6 Recommendations for Implementation

Following the investigation of the shear strength properties of the #57 aggregate employed as backfill behind the retaining wall, and after reviewing the Special Provisions for retaining walls (SP624), several gaps were identified in Section B of SP624: "Cast-In-Place (CIP) Concrete Cantilever and Counterfort Retaining Walls". New guidelines and provisions are proposed below. The updated provisions address compaction activities for these wall types, clearly defining compaction procedures and lift thicknesses for both loaded and unloaded zones. In addition, the team established recommended values for the critical-state friction angle and dilatancy angle of crushed limestone and river gravel as a function of wall height. Finally, new guidelines for estimating the required volume of backfill material behind the retaining wall are presented.

6.1 Backfill placement in lifts

6.1.1 Definition of Loaded and Unloaded Zones behind the Retaining Walls

Loaded Zone: The portion of the backfill that lies within the area influenced by roadway surcharge, structural footings, slabs, embankments, or any other sustained vertical or lateral loads. This zone experiences increased stresses due to the applied loads and typically requires materials with higher strength or stiffness to ensure stability and performance.

Unloaded Zone: The portion of the backfill that is not subjected to roadway surcharge, structural loads, or any other sustained vertical or lateral forces. This zone lies outside the primary influence area of footings, slabs, or external loading and therefore typically experiences only self-weight stresses.

6.1.2 Backfill Placement in Lifts

- Loaded Zone:
  - Backfill shall be placed in horizontal (level) lifts not exceeding 250 mm (10 in.) loose thickness.
  - Each lift shall be compacted to the specified density before placement of subsequent lifts.
  - Lift thickness may be reduced where restricted access or compaction equipment limitations require thinner layers (e.g., within 3 ft of the wall stem).
- Unloaded Zone:
  - Backfill may be placed in horizontal lifts not exceeding 500 mm (20 in.), loose thickness, provided that the material is free-draining and the required compaction is achieved.
  - The Engineer may require thinner lifts if density requirements are not met or if equipment is unable to achieve uniform compaction at the permitted thickness.
- General Requirement:
  - Lifts shall be level and uniform across the placement area.

- Sloped or wedge-shaped lifts will not be permitted, except where necessary to maintain positive drainage away from the wall.

6.1.3 Compaction of Backfill Materials

For backfill containing more than 30 percent retained on the ¾-inch sieve, the following compaction requirements shall apply:

- Zone within 3 ft (1.0 m) of wall stem:
  - Large vibratory rollers shall not be used within 3 ft of the wall stem to prevent excessive vibration, displacement, or overstressing of the wall stem panels and reinforcement.
  - Compaction in this zone shall be achieved using a light vibratory plate (200–400 lb) or a small rammer, with a minimum of two (2) passes over each lift.
- Zone beyond 3 ft (1.0 m) of wall stem:
  - Compaction shall be performed using a smooth-drum vibratory roller with an operating weight of 6–10 tons.
  - The roller shall operate in low-amplitude / high-frequency mode, at a travel speed not exceeding 2 mph (3 km/h).
  - A minimum of two (2) roller passes per lift shall be required to achieve the specified density.
- Lift Thickness:
  - Maximum loose lift thickness shall not exceed 12 in. (300 mm) for granular materials.
  - Thinner lifts may be required where equipment maneuverability is restricted.
  - Backfill shall be placed uniformly on both sides of structural elements to minimize unbalanced loading. For granular free-draining materials, water sprinkling may be required to mitigate segregation or dusting.

6.2 Shear strength of backfill materials

The required average and standard deviation values for the friction angle and dilatancy angle of the backfill material, based on the nature of the material and the wall height, are summarized in Table 6-1, and Table 6-2, respectively.

Table 6-1. Values of recommended friction angles for #57 aggregates.

Wall Height (ft)	Crushed limestone (#57 stone gradation)	River Gravel (#57 stone gradation)
< 10 ft	57.8° ± 2.1°	52.5° ± 1.7°
15 ft	55.3° ± 2.0°	50.5° ± 1.7°
20 ft	53.5° ± 2.0°	49.0° ± 1.6°
25 ft	52.2° ± 1.7°	48.0° ± 1.6°
30 ft	51.2° ± 1.7°	47.0° ± 1.6°

Table 6-2.Values of recommended dilatancy angles for #57 aggregates.

Wall Height (ft)	Crushed limestone (#57 stone gradation)	River Gravel (#57 stone gradation)
< 10 ft	11.6º ± 0.9º	13.3º ± 1.0º
15 ft	9.3º ± 0.8º	10.8º ± 0.5º
20 ft	8.0º ± 0.9º	9.8º ± 0.5º
25 ft	7.0º ± 0.9º	8.8º ± 0.5º
30 ft	6.3º ± 0.8º	7.8º ± 0.5º

6.3 Volume of backfill material behind the retaining walls

According to the new guidelines, the backfill material begins at the top of the retaining wall's heel and rises with a 0.75:1 slope until it reaches the ground surface (Figure 5-8 (b))**.** If geomaterials classified as intermediate geomaterials which include hard soils and soft rocks such as clay shales and mudstones with undrained shear strength (C_u) in the range of 5,000 psf (250 kPa) < C_u < 50,000 psf (2500 kPa), or noncohesive materials such as glacial till with N_{60} > 50, the geomaterial is strong and stable, and engineer may adopt the case shown in Figure 5-8 (c)

Chapter 7 List of References

AASHTO M43 (2021). " Standard Specification for Sizes of Aggregate for Road and Bridge Construction." American Association of State Highway and Transportation Officials, Washington, D.C.

Alsaleh, M. I. (2004). *Numerical modeling of strain localization in granular materials using Cosserat theory enhanced with microfabric properties*, Louisiana State University and Agricultural & Mechanical College.

Alsaleh, M. I., Voyiadjis, G. Z., and Alshibli, K. A. (2006). "Modelling strain localization in granular materials using micropolar theory: mathematical formulations." *International journal for numerical and analytical methods in geomechanics*, 30(15), 1501-1524.

Alshibli, K., and Roussel, L. (2006). "Experimental investigation of slip-stick behaviour in granular materials." *International journal for numerical and analytical methods in geomechanics*, 30(14), 1391-1407.

Alshibli, K. A., Alsaleh, M. I., and Voyiadjis, G. Z. (2006). "Modelling strain localization in granular materials using micropolar theory: Numerical implementation and verification." *International Journal for Numerical and Analytical Methods in Geomechanics*, 30(15), 1525-1544.

Alshibli, K. A., and Cil, M. B. (2018). "Influence of particle morphology on the friction and dilatancy of sand." *Journal of Geotechnical and Geoenvironmental Engineering*, 144(3), 04017118.

Alshibli, K. A., Druckrey, A. M., Al-Raoush, R. I., Weiskittel, T., and Lavrik, N. V. (2015). "Quantifying morphology of sands using 3D imaging." *Journal of Materials in Civil Engineering*, 27(10), 04014275.

ASTM 854 (2023). "Standard test methods for specific gravity of soil solids by the water displacement method." ASTM International West Conshohocken, PA.

ASTM 4253 (2006). *Standard test methods for maximum index density and unit weight of soils using a vibratory table*, ASTM international, West Conshohocken, PA.

ASTM C127 (2015). "Standard test method for relative density (specific gravity) and absorption of coarse aggregate." West Conshohocken, PA.

ASTM C136/C136M (2014). "C136/C136M." *Standard Test Method for Sieve Analysis of Fine and Coarse Aggregates, ASTM International, West Conshohocken, PA*, ASTM International, West Conshohocken, PA.

ASTM D4254 (2016). "Standard test methods for minimum index density and unit weight of soils and calculation of relative density." ASTM International, West Conshohocken, PA.

ASTM E1621 (2022). "Standard Guide for Elemental Analysis by Wavelength Dispersive X-Ray Fluorescence Spectrometry." ASTM International, West Conshohocken, PA.

Bolton, M. (1986). "The strength and dilatancy of sands." *Geotechnique*, 36(1), 65-78.

Bowles, J. E. (1988). *Foundation analysis and design*.

Chakraborty, T., and Salgado, R. (2010). "Dilatancy and shear strength of sand at low confining pressures." *Journal of geotechnical and geoenvironmental engineering*, 136(3), 527-532.

Cho, G.-C., Dodds, J., and Santamarina, J. C. (2006). "Particle shape effects on packing density, stiffness, and strength: natural and crushed sands." *Journal of geotechnical and geoenvironmental engineering*, 132(5), 591-602.

Coulomb, C. A. (1773). "Essai sur une application des regles de maximis et minimis a quelques problemes de statique relatifs a 1'architecture." *Mem. Div. Sav. Acad.*

Coyle, H., Bartoskewitz, R., Milberger, L., and Butler, H. (1974). "FIELD MEASUREMENTS OF LATERAL EARTH PRESSURES ON A CANTILEVER RETAINING WALL." *Transportation Research Record*(517).

Das, B. M. (2011). "Principles of foundation engineering, SI." *th edition*, 133.

Druckrey, A. M., Alshibli, K. A., and Al-Raoush, R. I. (2016). "3D characterization of sand particle-to-particle contact and morphology." *Computers and Geotechnics*, 74, 26-35.

Dubrova, G. (1963). "Interaction between soils and structures." *Rechnoy Transport*.

Fang, Y.-S., and Ishibashi, I. (1986). "Static earth pressures with various wall movements." *Journal of Geotechnical Engineering*, 112(3), 317-333.
Goel, S., and Patra, N. R. (2008). "Effect of arching on active earth pressure for rigid retaining walls considering translation mode." *International Journal of Geomechanics*, 8(2), 123-133.
Handy, R. L. (1985). "The arch in soil arching." *Journal of Geotechnical Engineering*, 111(3), 302-318.
Hasan, A., and Alshibli, K. A. (2010). "Discrete element modeling of strength properties of Johnson Space Center (JSC-1A) lunar regolith simulant." *Journal of Aerospace Engineering*, 23(3), 157-165.
Honkanadavar, N., and Sharma, K. (2014). "Testing and modeling the behavior of riverbed and blasted quarried rockfill materials." *International Journal of Geomechanics*, 14(6), 04014028.
Indraratna, B., Ionescu, D., and Christie, H. (1998). "Shear behavior of railway ballast based on large-scale triaxial tests." *Journal of geotechnical and geoenvironmental Engineering*, 124(5), 439-449.
Lade, P., and Kim, M. (1988). "Single hardening constitutive model for frictional materials II. Yield critirion and plastic work contours." *Computers and geotechnics*, 6(1), 13-29.
Lee, K. C. (2017). "Particle morphology and its influence on friction and dilatancy of sands." M.S., University of Tennessee, Knoxville, Knoxville, TN.
Matsuo, M., Kenmochi, S., and Yagi, H. (1978). "Experimental study on earth pressure of retaining wall by field tests." *Soils and Foundations*, 18(3), 27-41.
Nicks, J. (2013). "Friction Angles of Open-Graded Aggregates from Large-Scale Direct Shear Testing." Federal Highway Administration (FHWA), U.S. Department of Transportation, McLean, VA.
Nicks, J., Gebrenegus, T., and Adams, M. (2015). "Strength characterization of open-graded aggregates for structural backfills." United States. Federal Highway Administration. Office of Infrastructure ….
Nicks, J. E., Adams, M. T., Culbreth, N., and Gebrenegus, T. (2023). "Variability in the Engineering Properties of Open-Graded Aggregate Backfills: A Large-Scale Direct Shear Round-Robin Study."
Paik, K. H., and Salgado, R. (2003). "Estimation of active earth pressure against rigid retaining walls considering arching effects." *Geotechnique*, 53(7), 643-653.
Patel, S., and Deb, K. (2020). "Study of active earth pressure behind a vertical retaining wall subjected to rotation about the base." *International Journal of Geomechanics*, 20(4), 04020028.
Rankine, W. J. M. (1857). "II. On the stability of loose earth." *Philosophical transactions of the Royal Society of London*(147), 9-27.
Rothenburg, L., and Kruyt, N. P. (2004). "Critical state and evolution of coordination number in simulated granular materials." *International Journal of Solids and Structures*, 41(21), 5763-5774.
Schulze, L. W., Coyle, H. M., and Bartoskewitz, R. E. (1980). "Field measurements of earth pressure on a cantilever retaining wall." Texas A&M University.
Subpart P-Appendix A- (OSHA) "29 CFR Part 1926, Subpart P, Appendix A – Soil Classification." U.S. Department of Labor, Occupational Safety and Health Administration, Washington, D.C.
Subpart P-Appendix B- (OSHA) "29 CFR Part 1926, Subpart P, Appendix B – Sloping and Benching Requirements." U.S. Department of Labor, Occupational Safety and Health Administration, Washington, D.C.
Tatsuoka, F. (1987). "Discussion on strength and dilatancy of sand." *Géotechnique*, 37(2), 219-225.
Tennessee Department of Transportation (TDOT) "County Outline Maps." <https://www.tn.gov/tdot/about/county-outline-map.html>.
Terzaghi, K. (1936). *A fundamental fallacy in earth pressure computations*, Harvard University.
Thermo Scientific. 2022. PerGeos SoftwareThermo Fisher Scientific, Waltham, MA.
Varadarajan, A., Sharma, K., Venkatachalam, K., and Gupta, A. (2003). "Testing and modeling two rockfill materials." *Journal of geotechnical and geoenvironmental engineering*, 129(3), 206-218.
Wang, Y.-Z. (2000). "Distribution of earth pressure on a retaining wall." *Geotechnique*, 50(1), 83-88.
Wood, D. M. (1990). *Soil behaviour and critical state soil mechanics*, Cambridge university press.

Yamaguchi, Y., Satoh, H., Hayashi, N., and Yoshinaga, H. (2008). "Strength evaluation of rockfill materials considering confining pressure dependency." *Journal of Japan Society of Dam Engineers*, 18(3), 166-181.

Yap, S., Salman, F., and Shirazi, S. (2012). "Comparative study of different theories on active earth pressure." *Journal of Central South University*, 19, 2933-2939.

Chapter 8 Appendices

Appendix (A): Photos of Tested Open Graded #57 Aggregates (OGA)

(A01)

(A02)

(A03)

(A04)

(A05)

(A06)

(A07)

(A08)

(A09)

(A10)

(A11)

(A12)

(A13)

(A14)

(A15)

(A16)

(A17)

(A18)

(A19)

(A20)

(A21)

(A22)

(A23)

(A24)

(A25)

(A26)

Figure 8-1. Photos of tested #57 Aggregates.

Appendix (B): Grain size distribution curves of the tested OGA

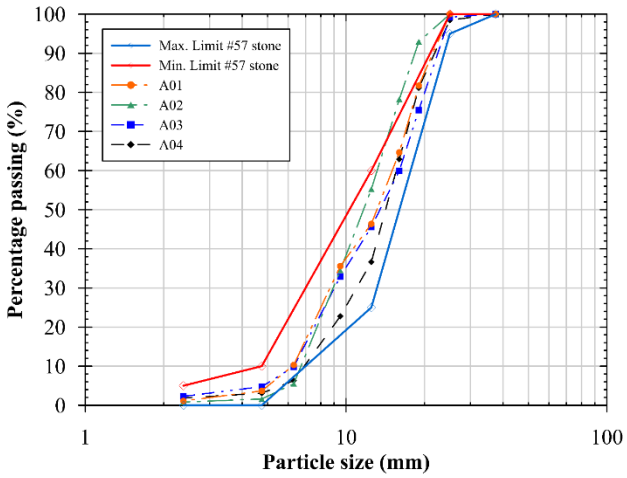

(A01-A02-A03-A04)

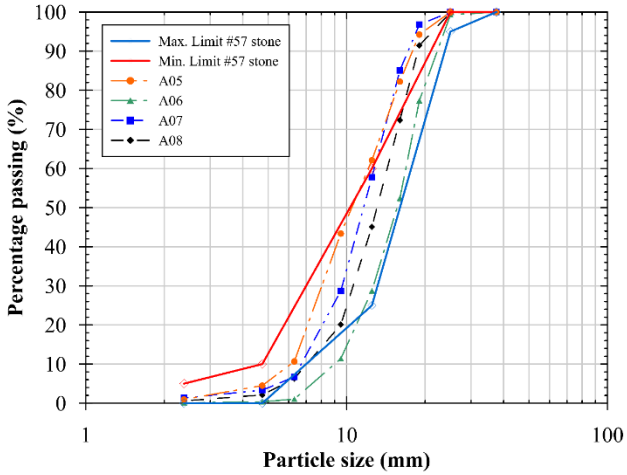

(A05-A06-A07-A08)

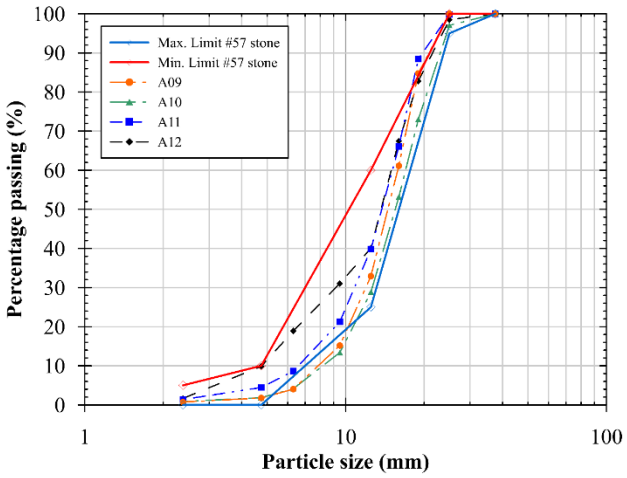

(A09-A10-A11-A12)

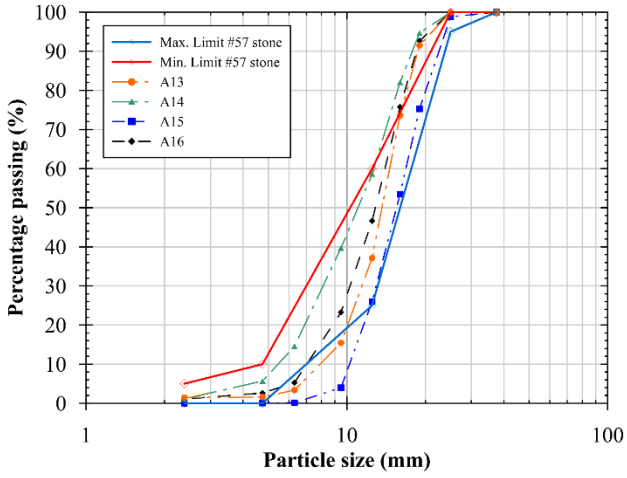

(A13-A14-A15-A16)

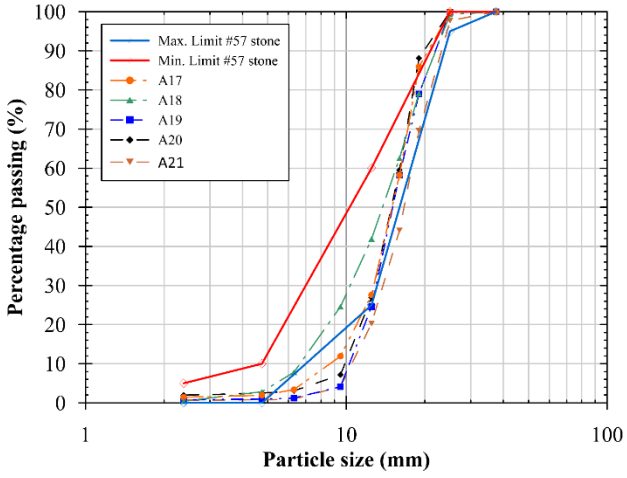

(A17-A18-A19-A20-21)

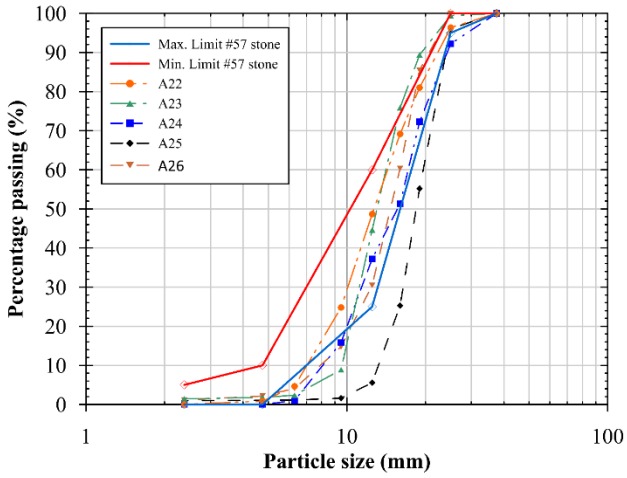

(22-A23-A24-A25-26)

Figure 8-2. Grain size distribution curves of OGA.

Appendix (C): Direct shear test results

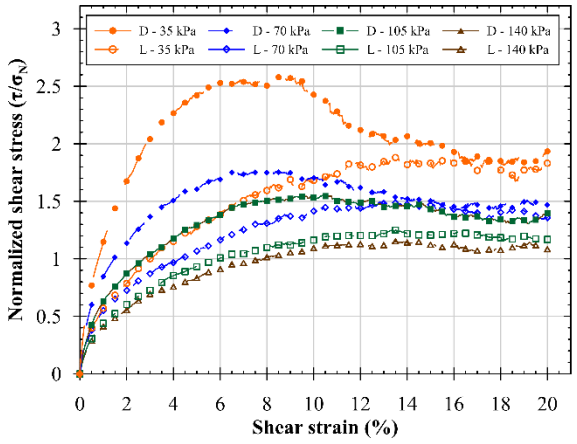

(A01 - a)

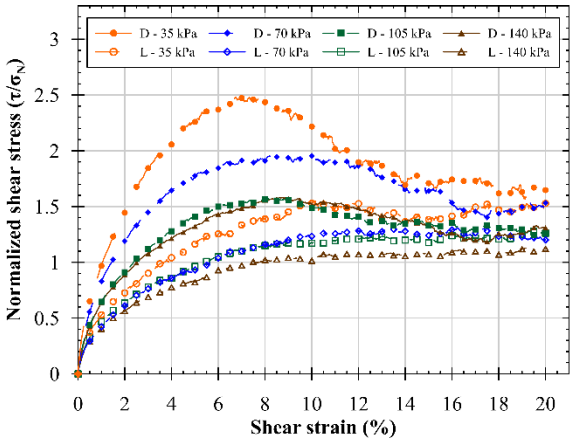

(A02 - a)

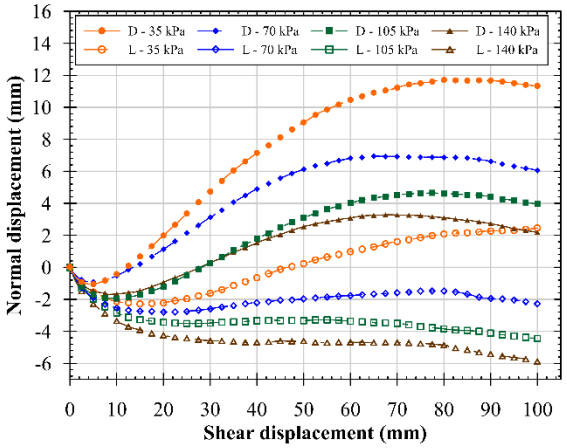

(A01 - b)

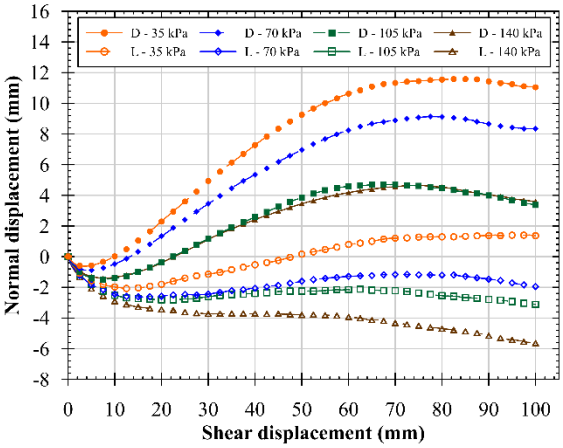

(A02 - b)

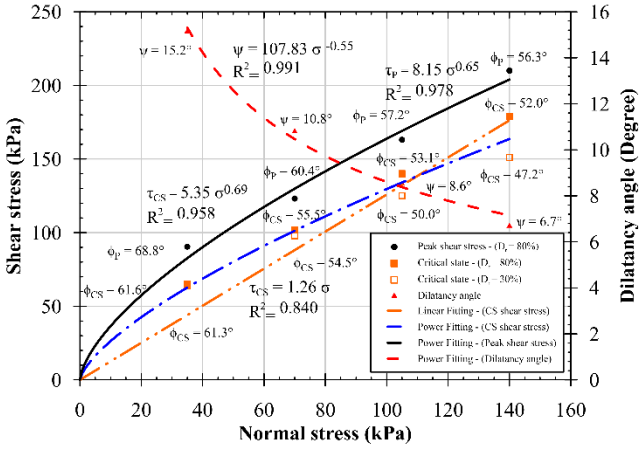

(A01 - c)

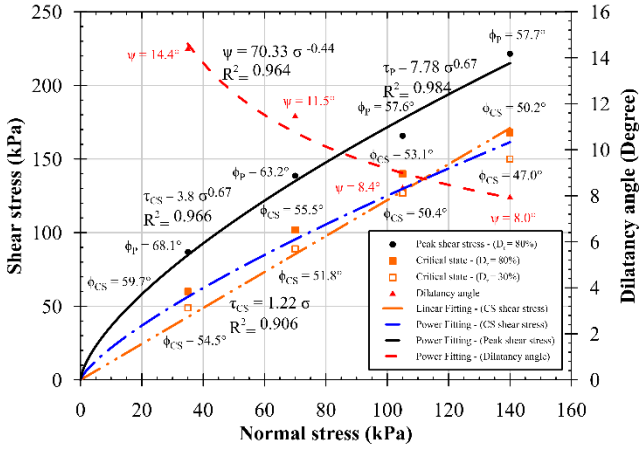

(A02- c)

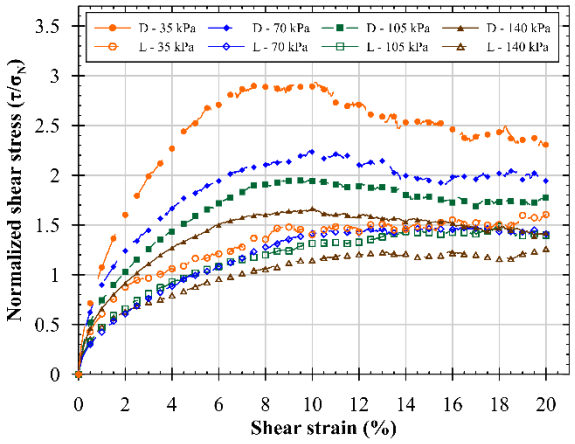

(A03 - a)

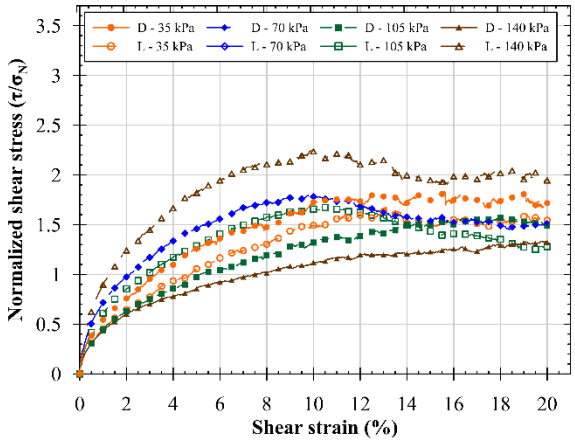

(A04 - a)

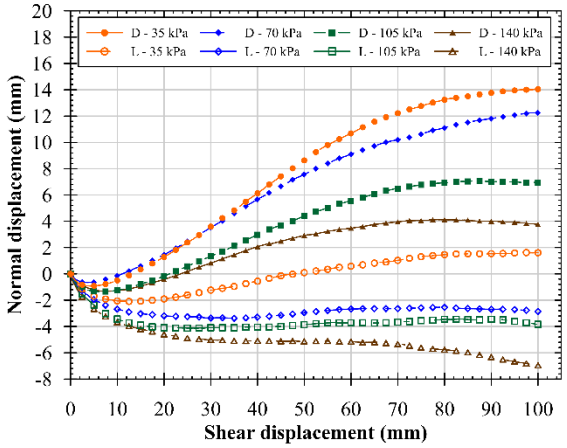

(A03 - b)

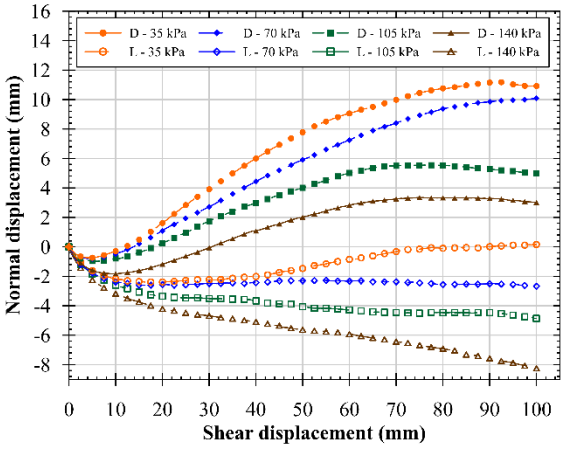

(A04 - b)

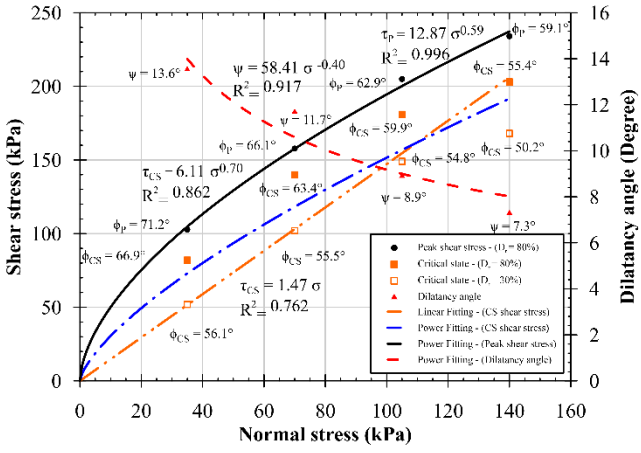

(A03 - c)

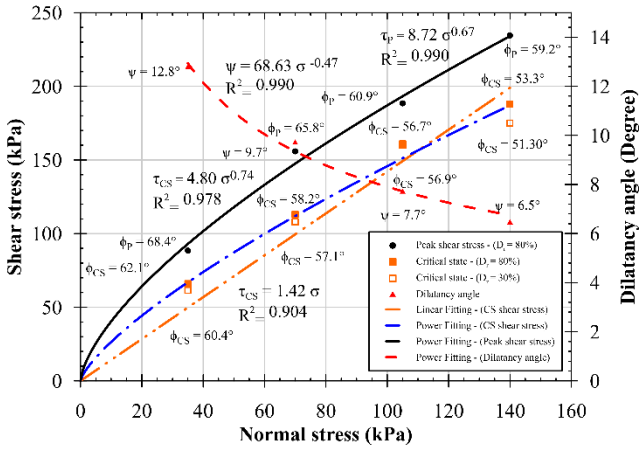

(A04- c)

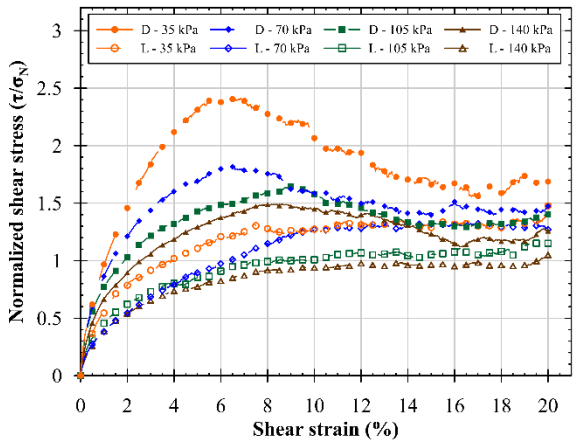

(A05 - a)

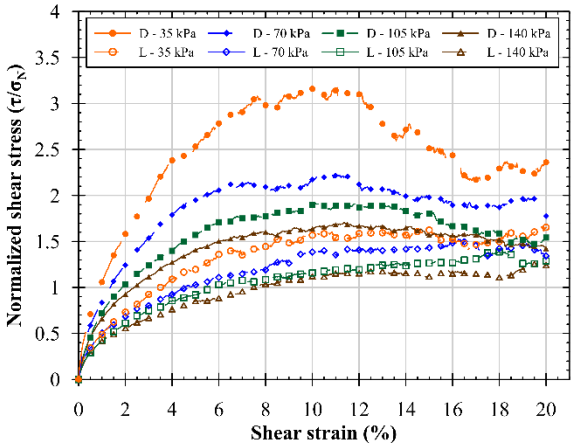

(A06 - a)

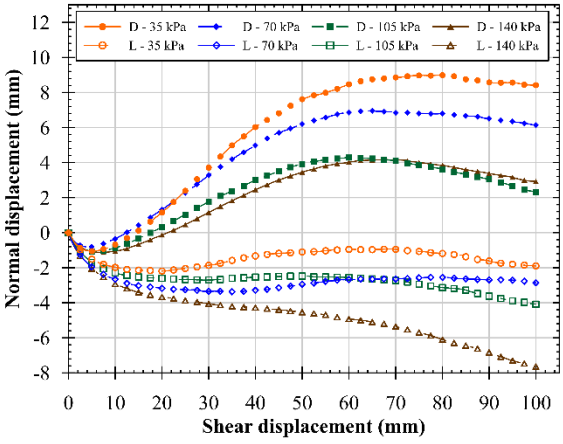

(A05 - b)

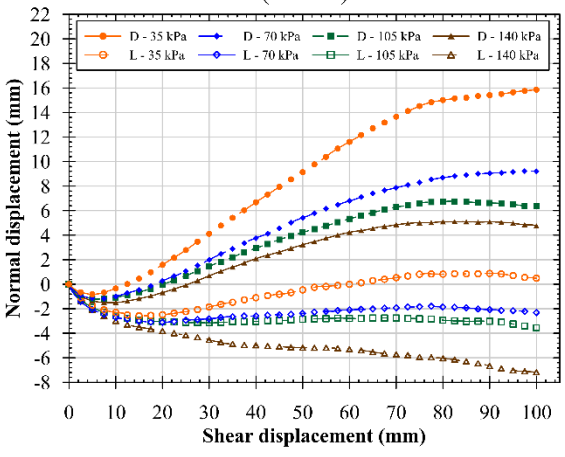

(A06 - b)

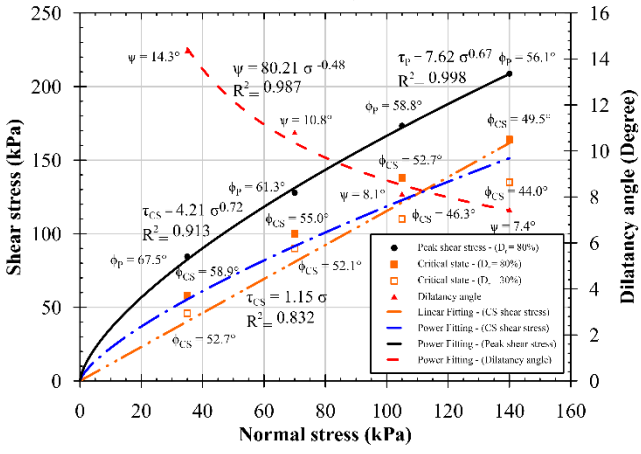

(A05 - c)

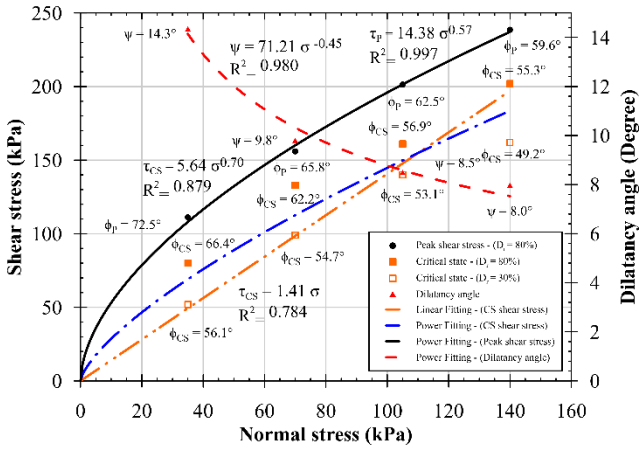

(A06- c)

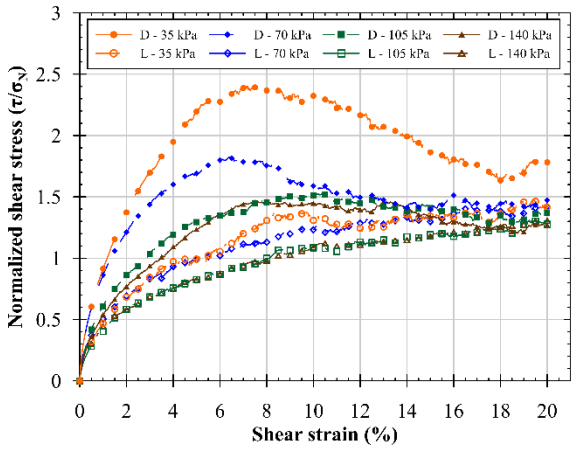

(A07 - a)

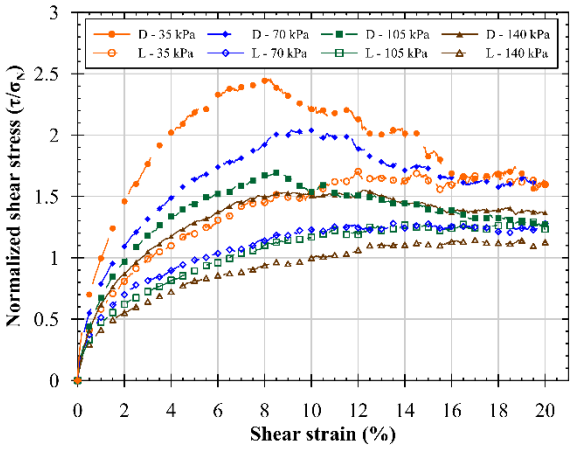

(A08 - a)

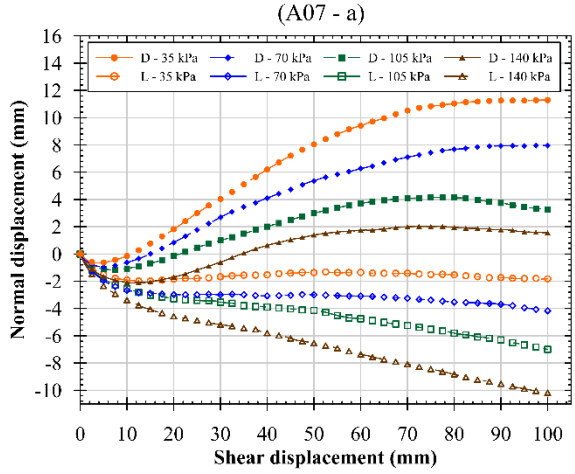

(A07 - b)

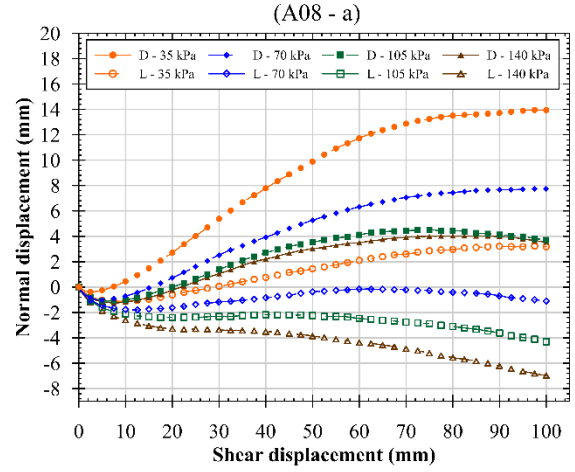

(A08 - b)

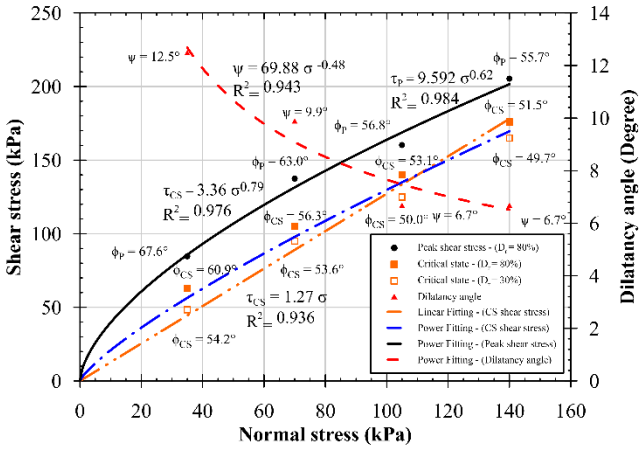

(A07 - c)

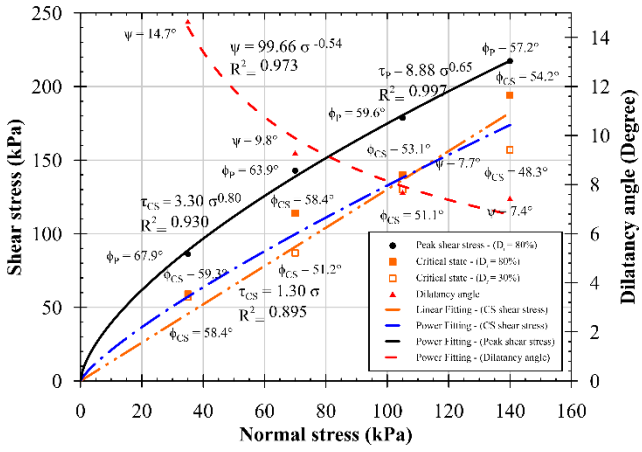

(A08- c)

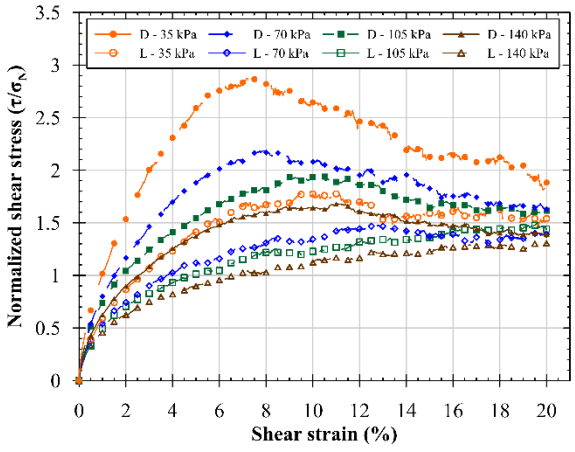

(A09 - a)

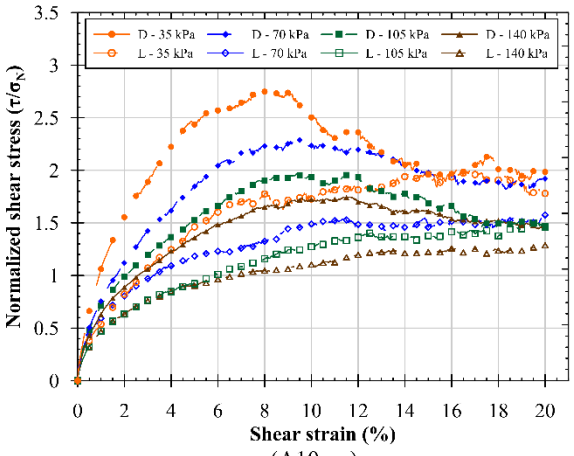

(A10 - a)

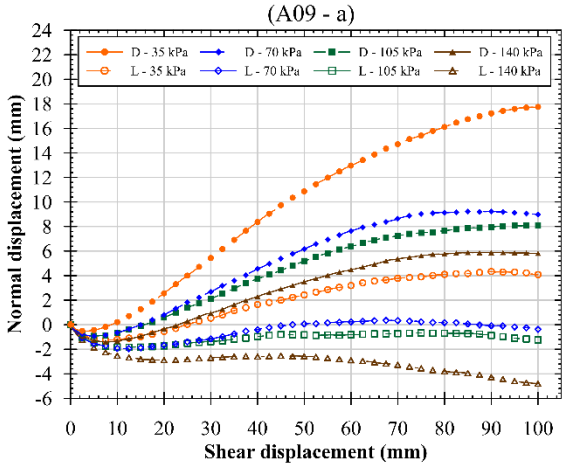

(A09 - b)

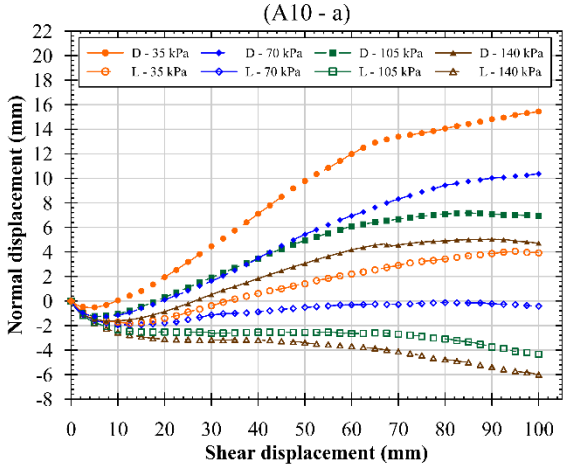

(A10 - b)

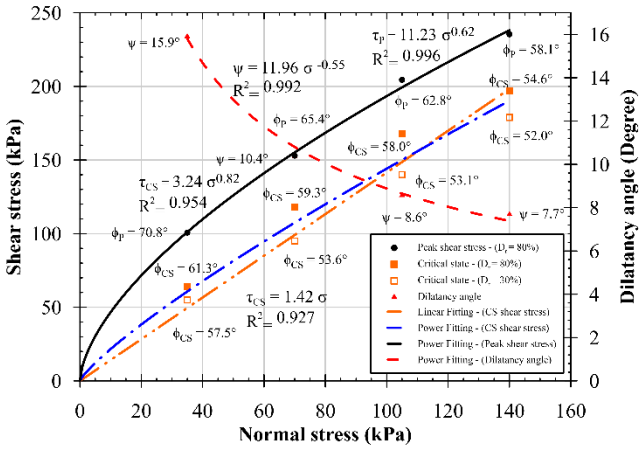

(A09 - c)

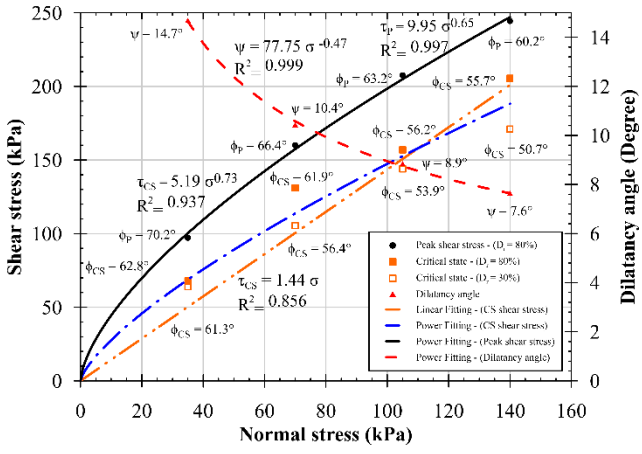

(A10- c)

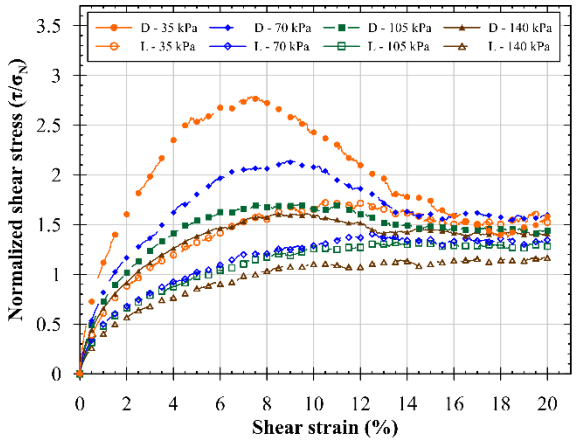

(A11 - a)

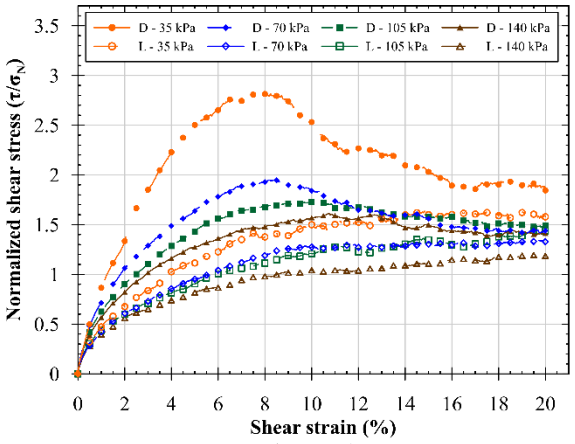

(A12 - a)

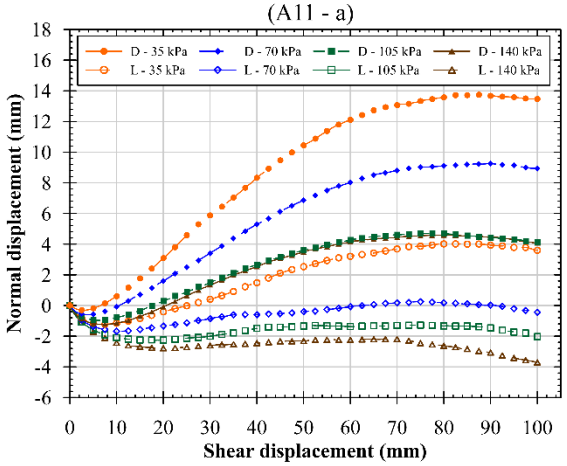

(A11 - b)

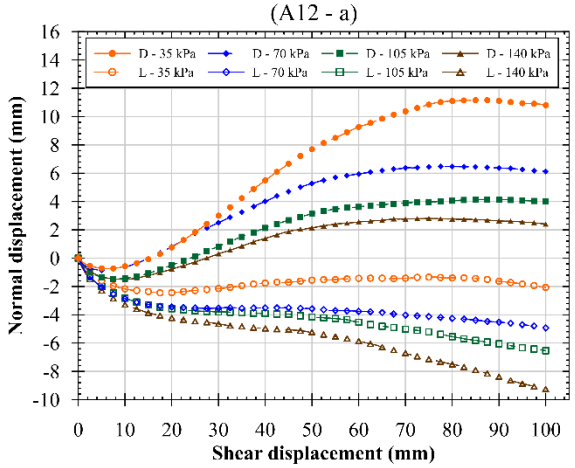

(A12 - b)

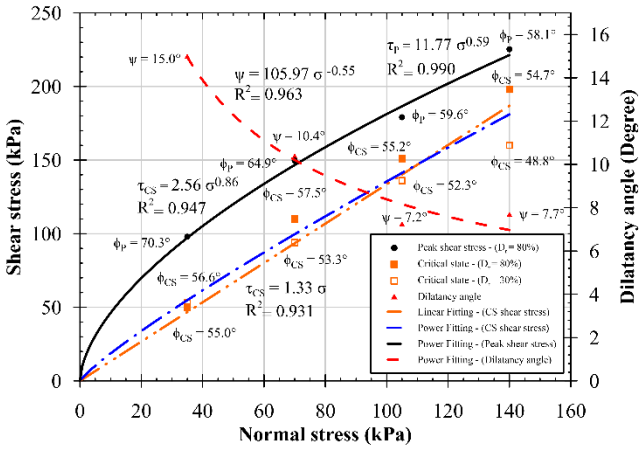

(A11 - c)

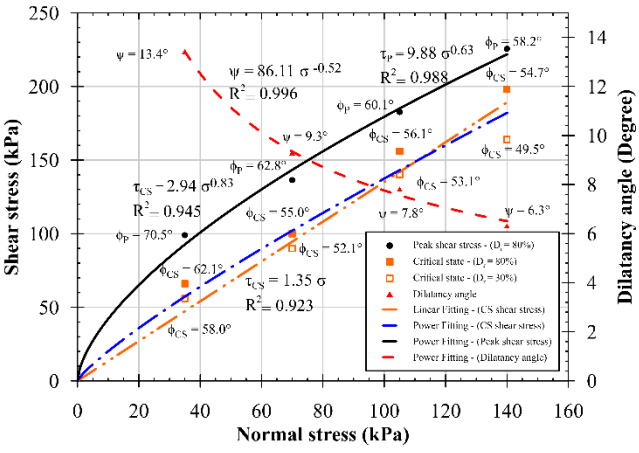

(A12- c)

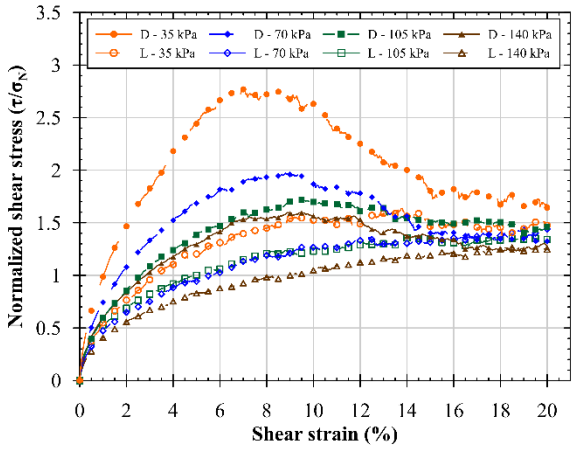

(A13 - a)

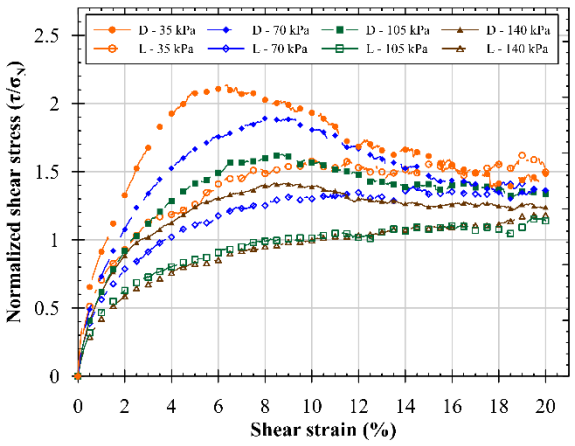

(A14 - a)

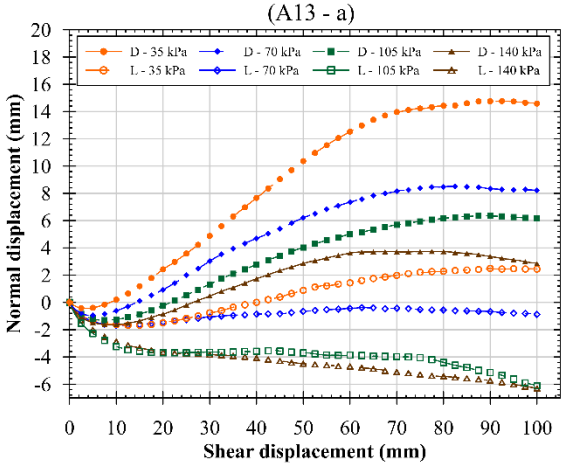

(A13 - b)

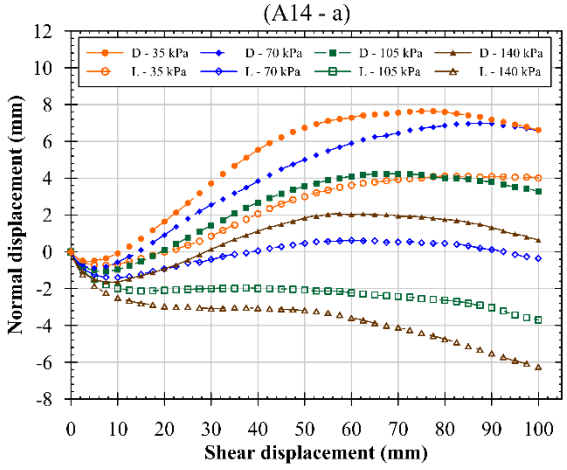

(A14 - b)

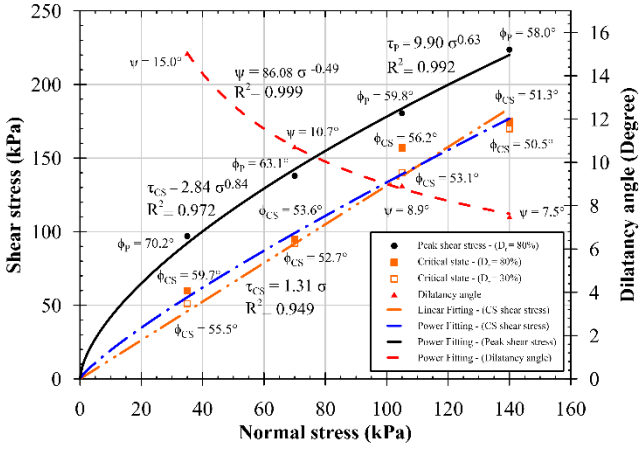

(A13 - c)

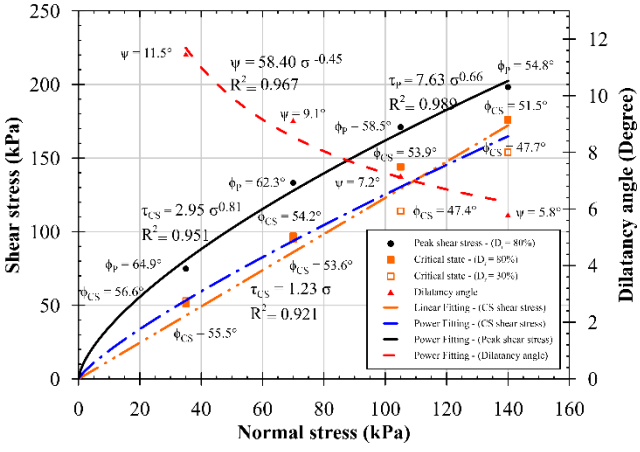

(A14- c)

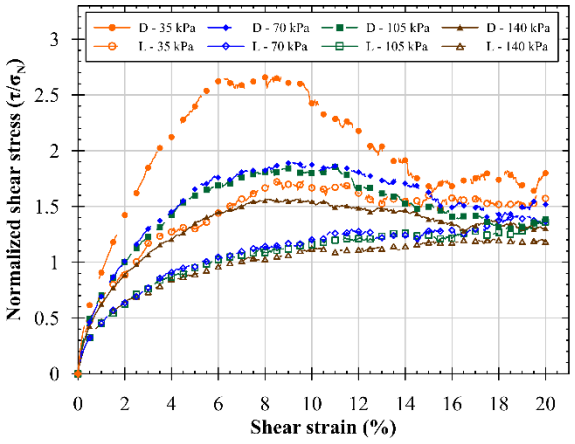

(A15 - a)

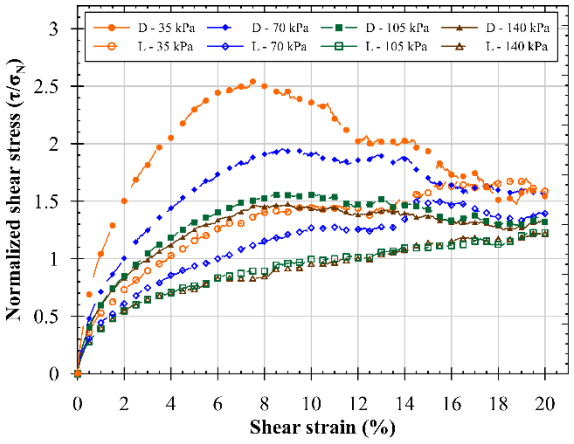

(A16 - a)

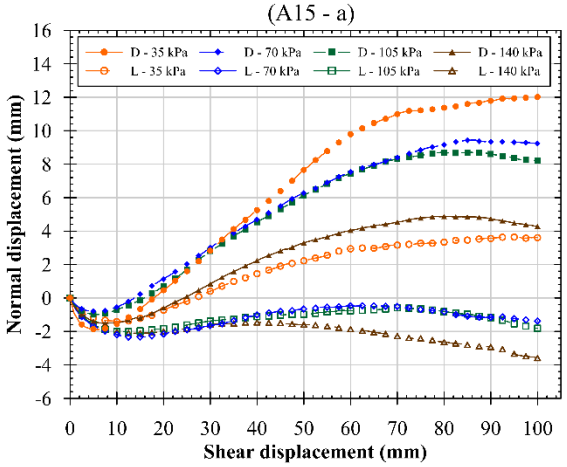

(A15 - b)

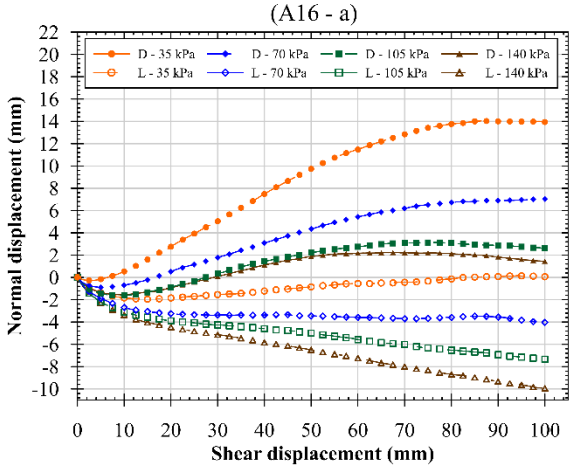

(A16 - b)

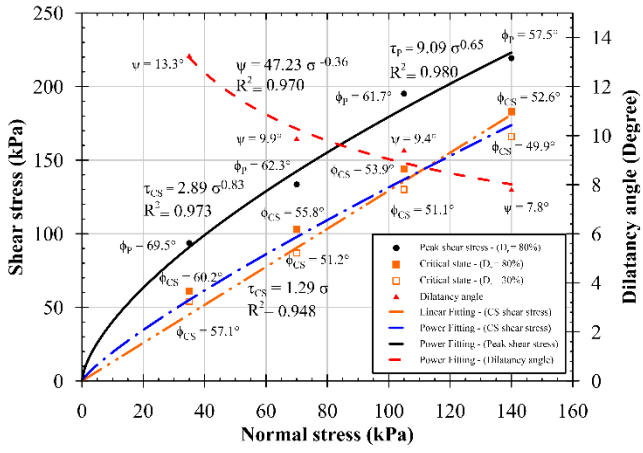

(A15 - c)

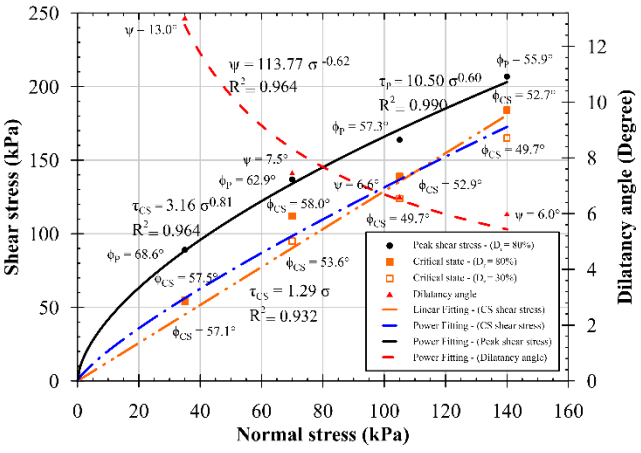

(A16- c)

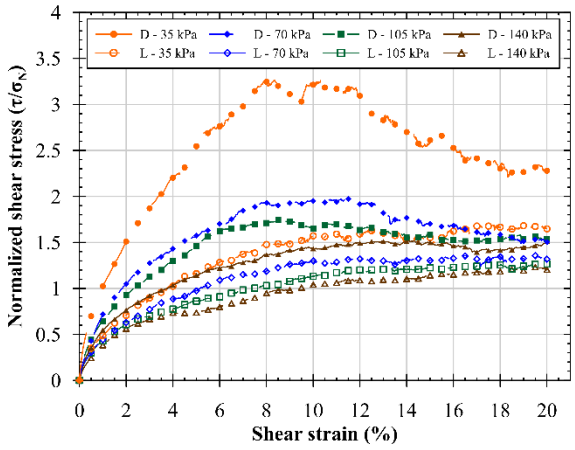

(A17 - a)

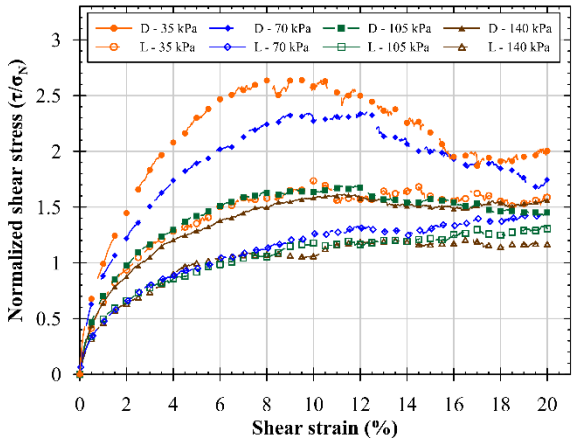

(A18 - a)

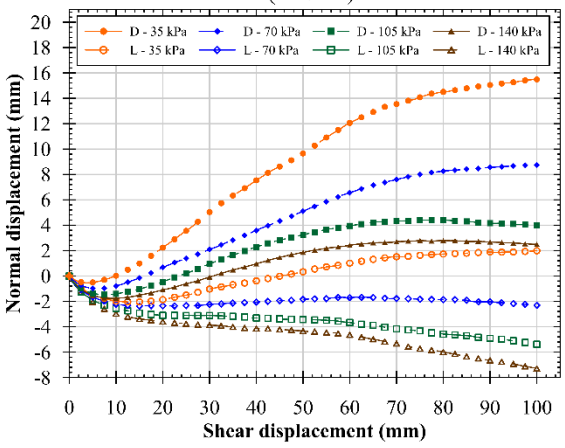

(A17 - b)

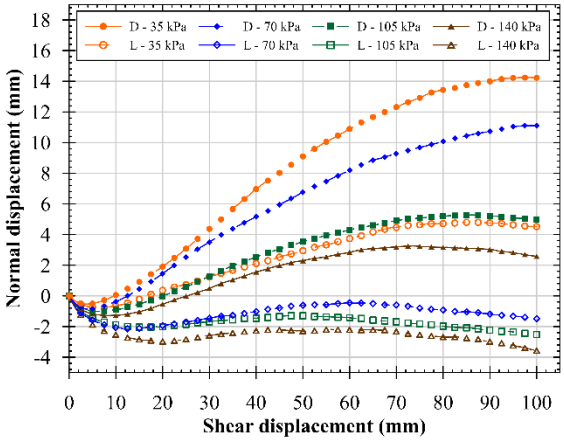

(A18 - b)

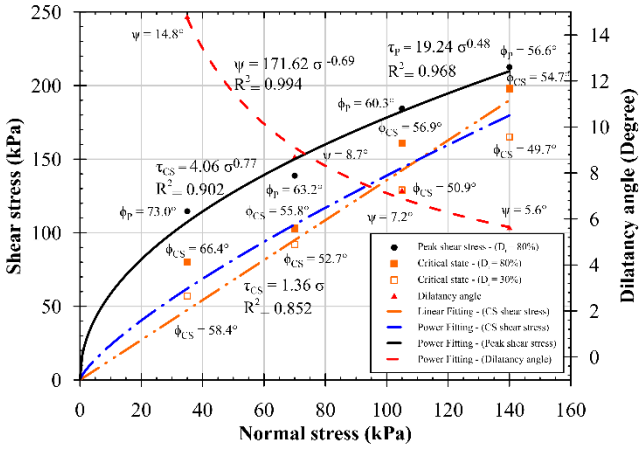

(A17 - c)

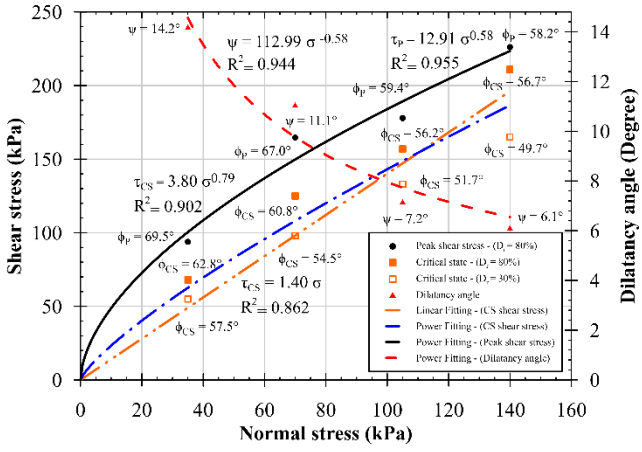

(A18- c)

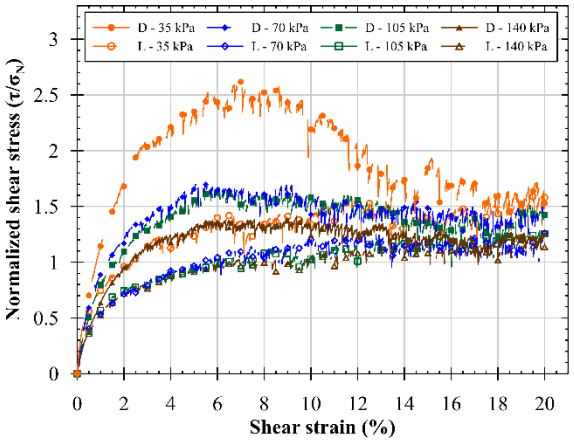

(A19 - a)

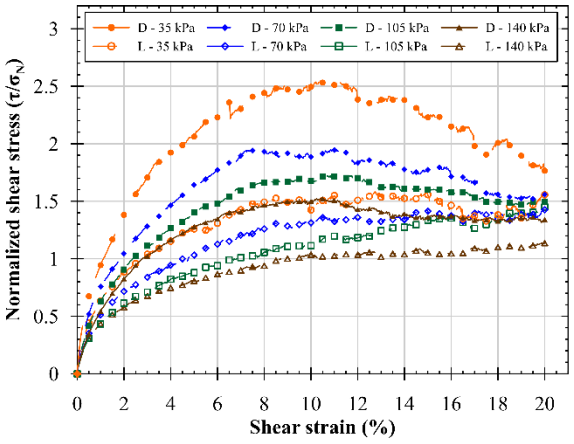

(A20 - a)

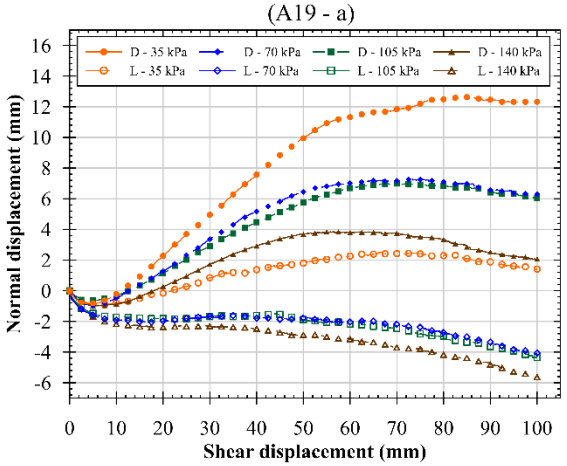

(A19 - b)

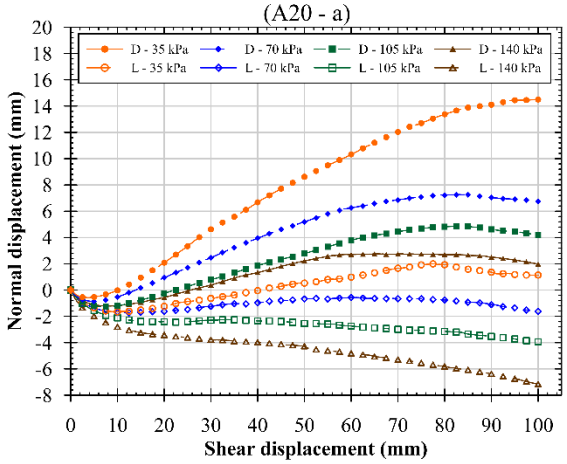

(A20 - b)

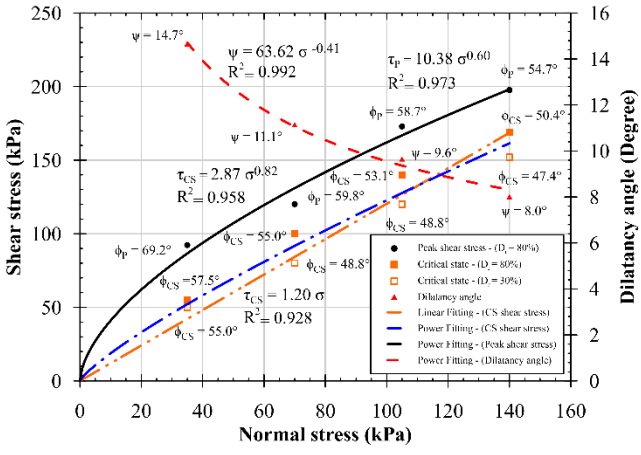

(A19 - c)

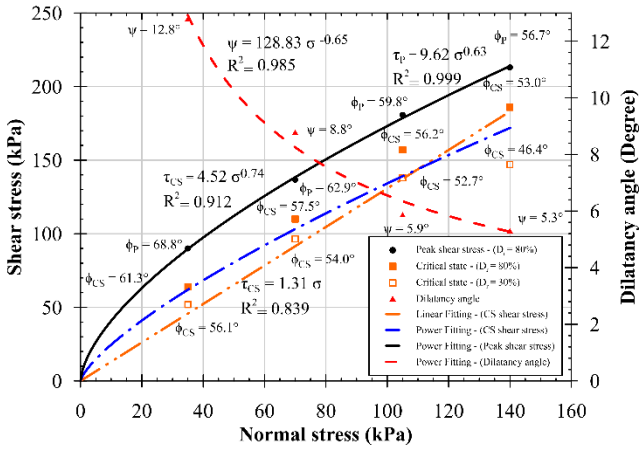

(A20- c)

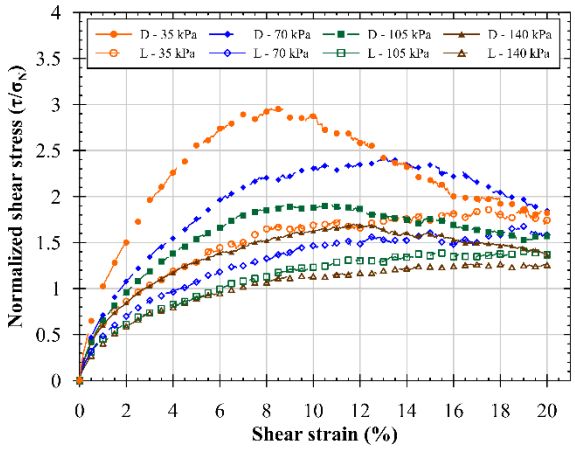

(A21 - a)

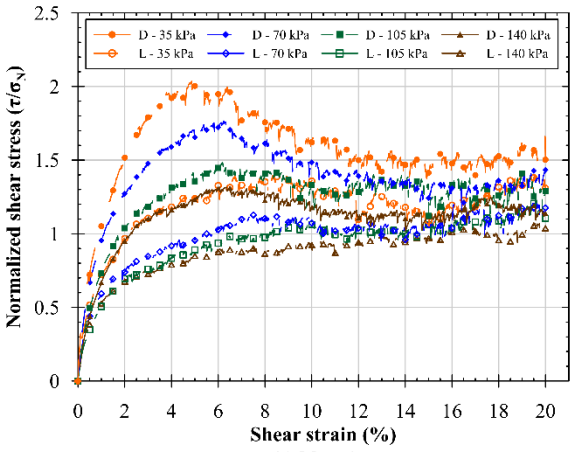

(A22 - a)

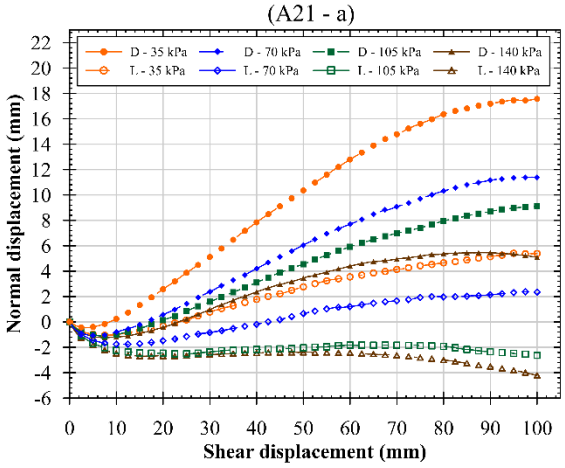

(A21 - b)

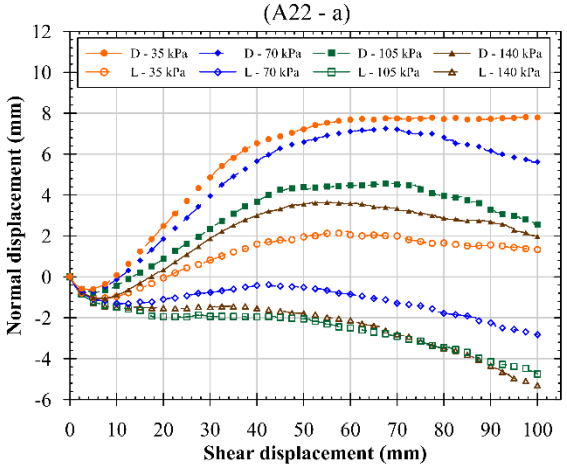

(A22 - b)

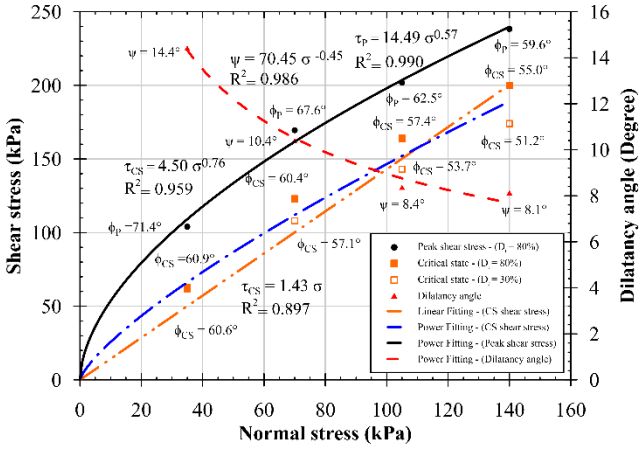

(A21 - c)

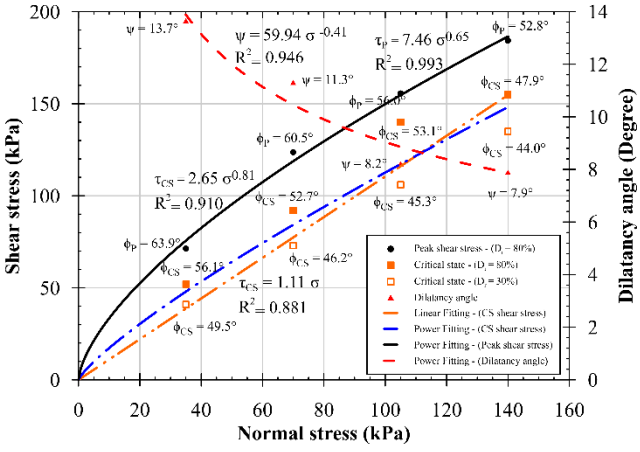

(A22- c)

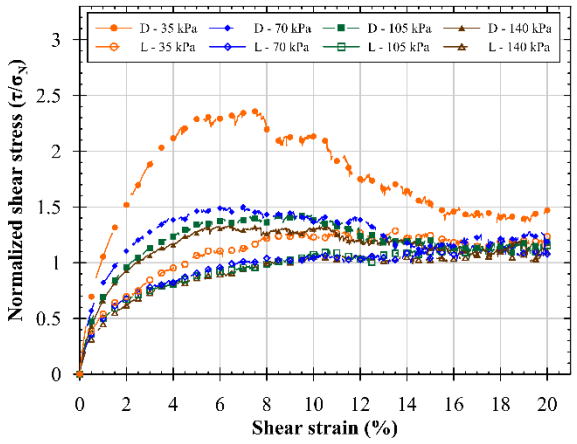

(A23 - a)

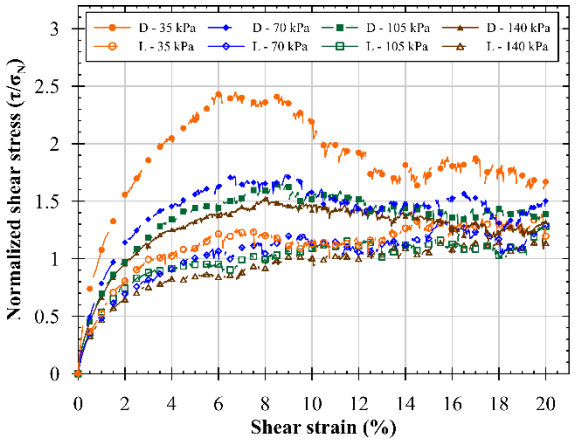

(A24 - a)

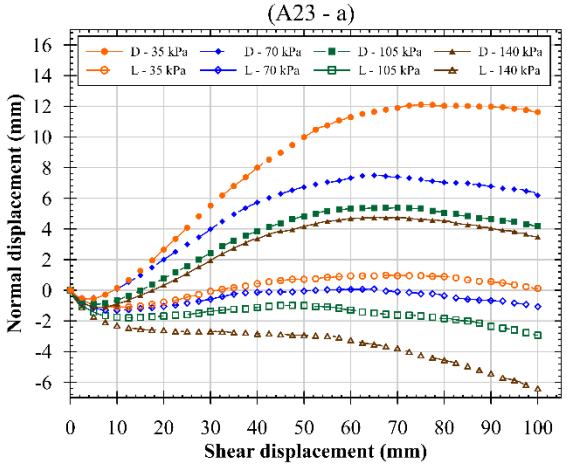

(A23 - b)

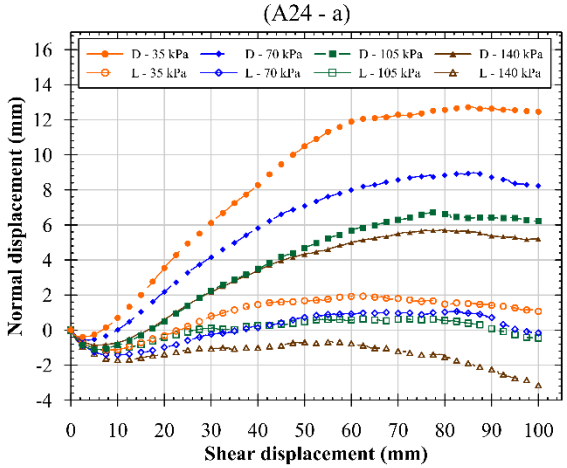

(A24 - b)

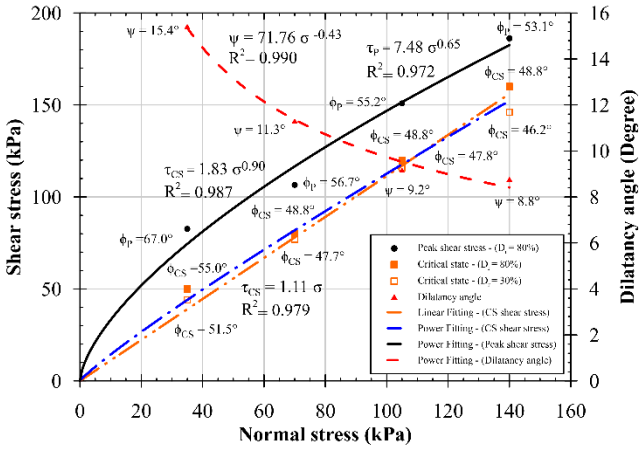

(A23 - c)

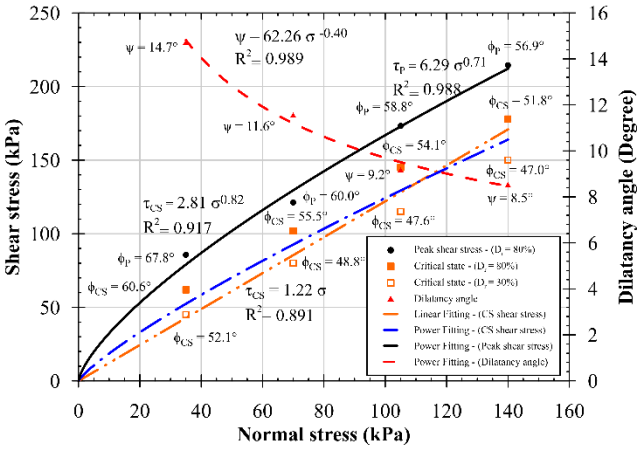

(A24- c)

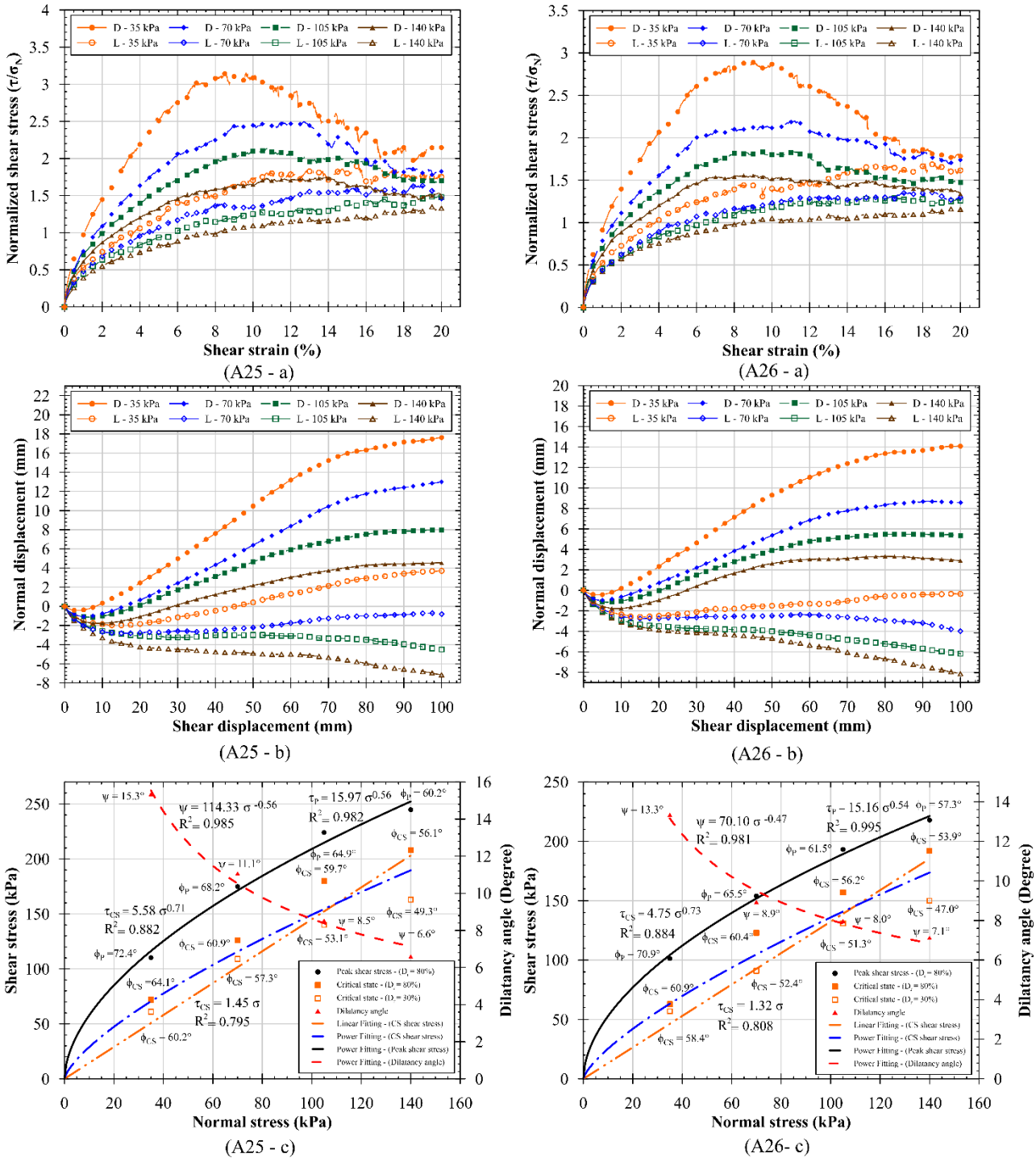

Figure 8-3. Results of the direct shear experiments.

Appendix (D): Morphology analysis of fine and coarse granular materials

Appendix (D-1): Particle size distribution of fine and coarse angular materials.

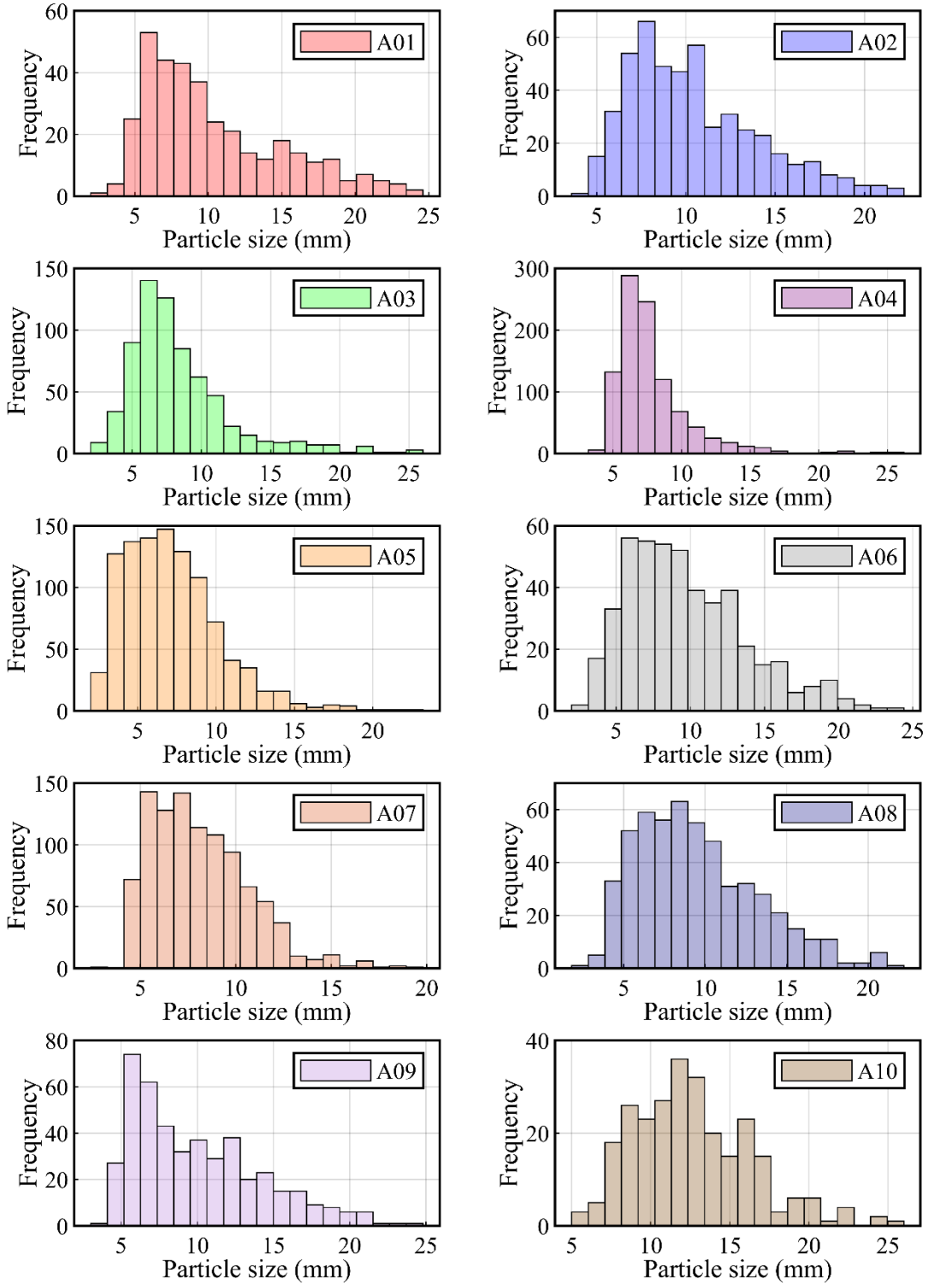

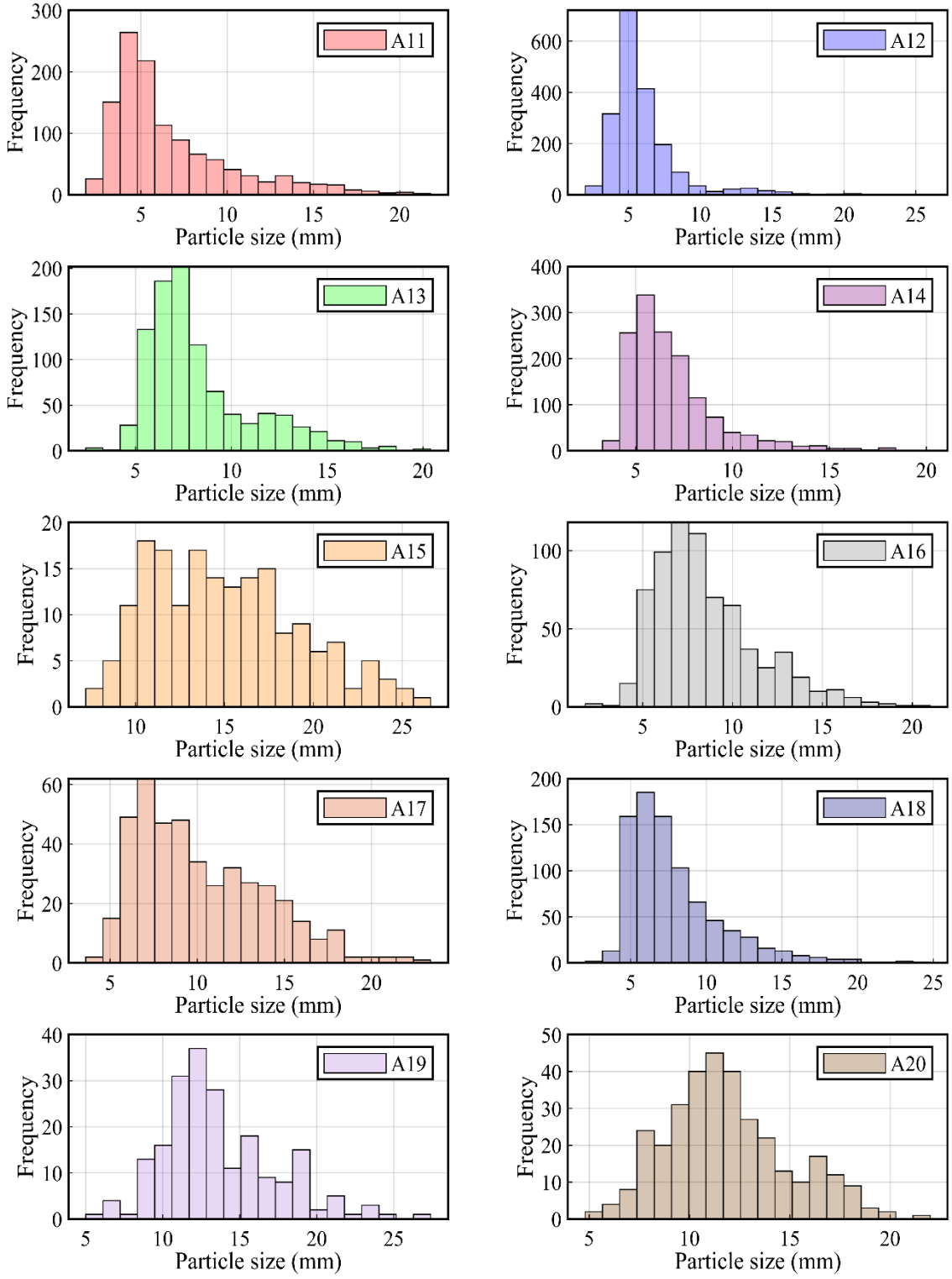
A11
A12
A13
A14
A15
A16
A17
A18
A19
A20
Frequency
Particle size (mm)

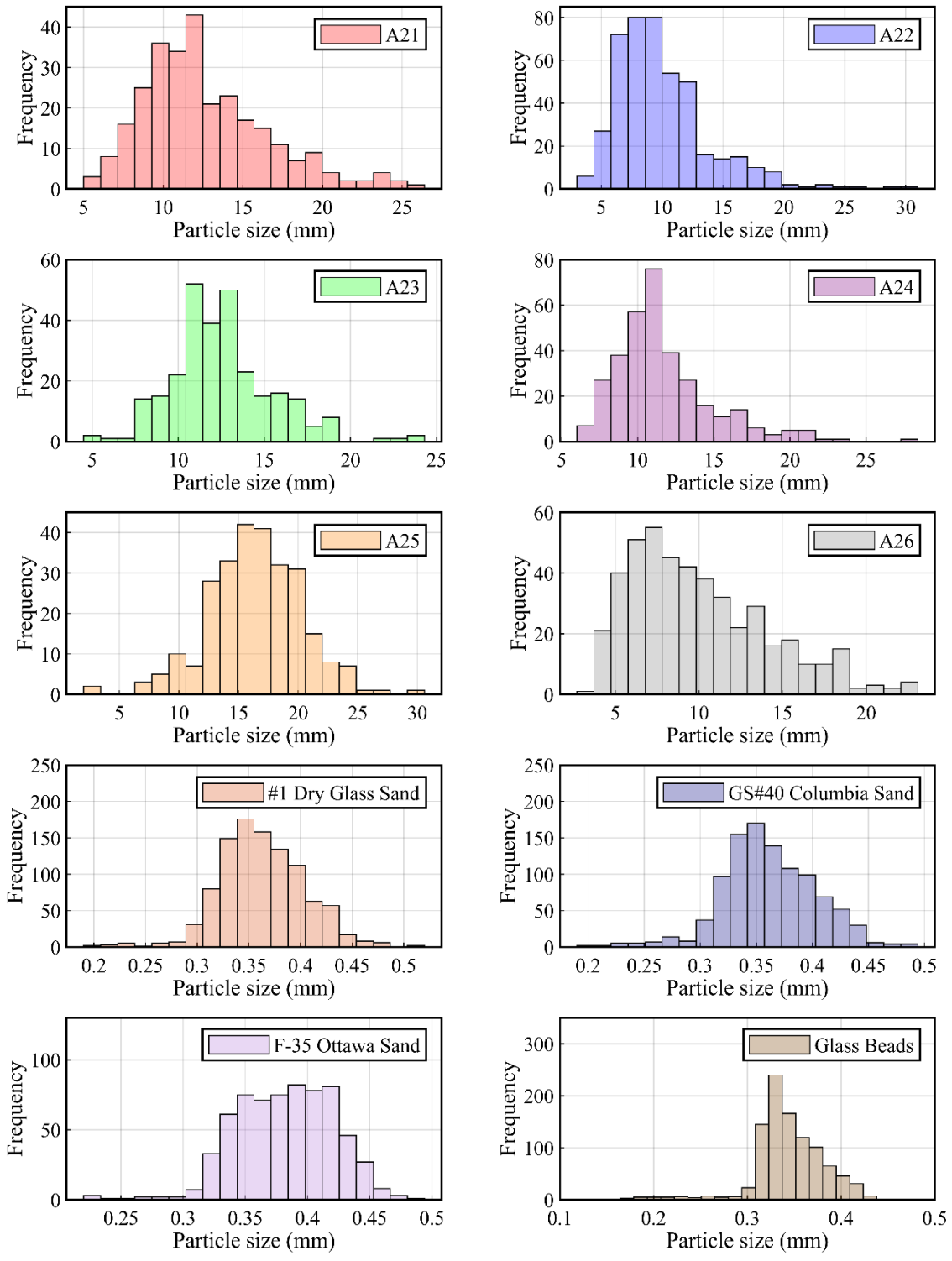

Figure 8-4. Particle size distribution of fine and coarse angular materials.

Appendix (D-2): Frequency distribution of Sphericity and the generalized extreme value (GEV) distribution of fine and coarse angular materials.

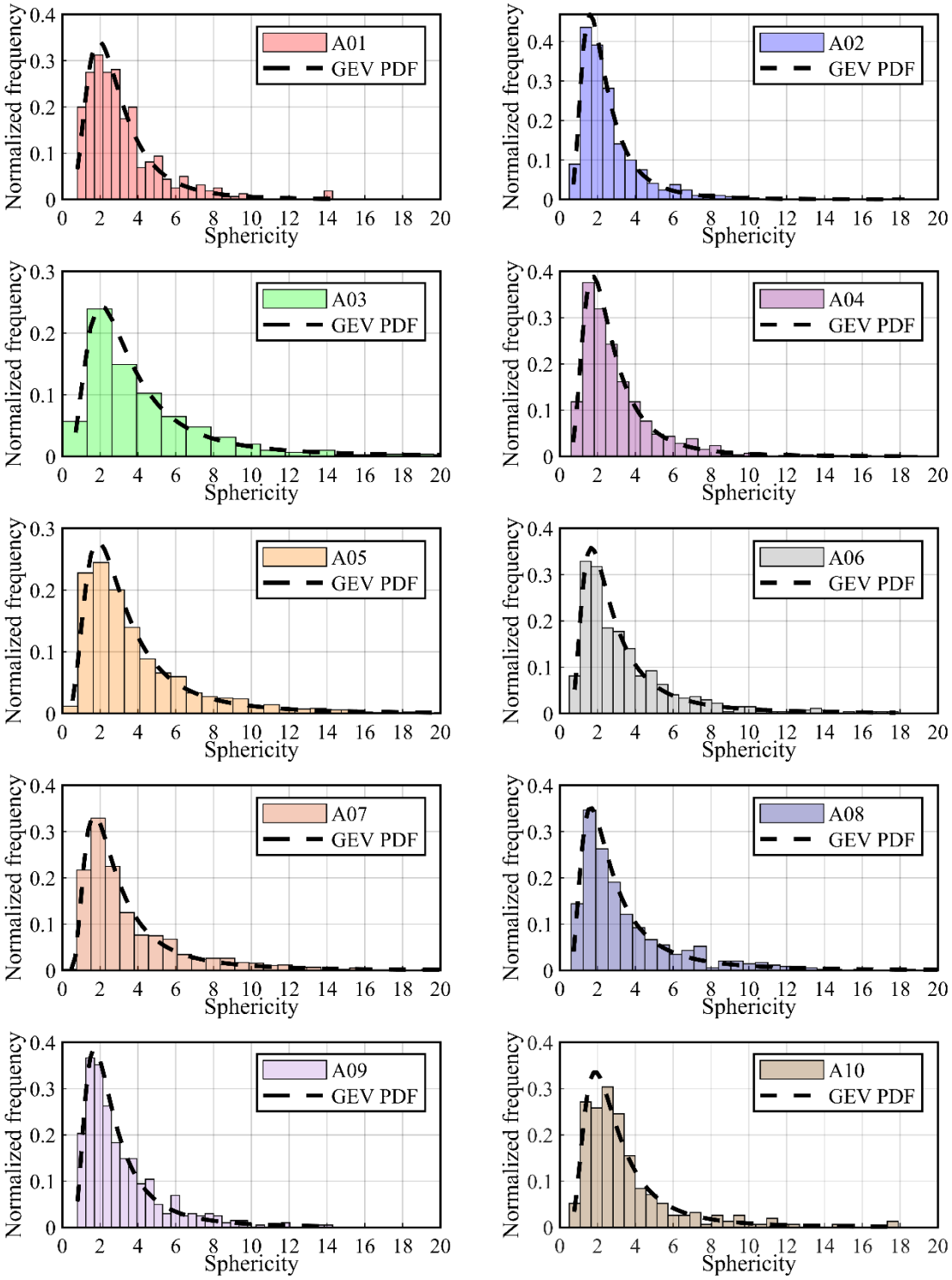

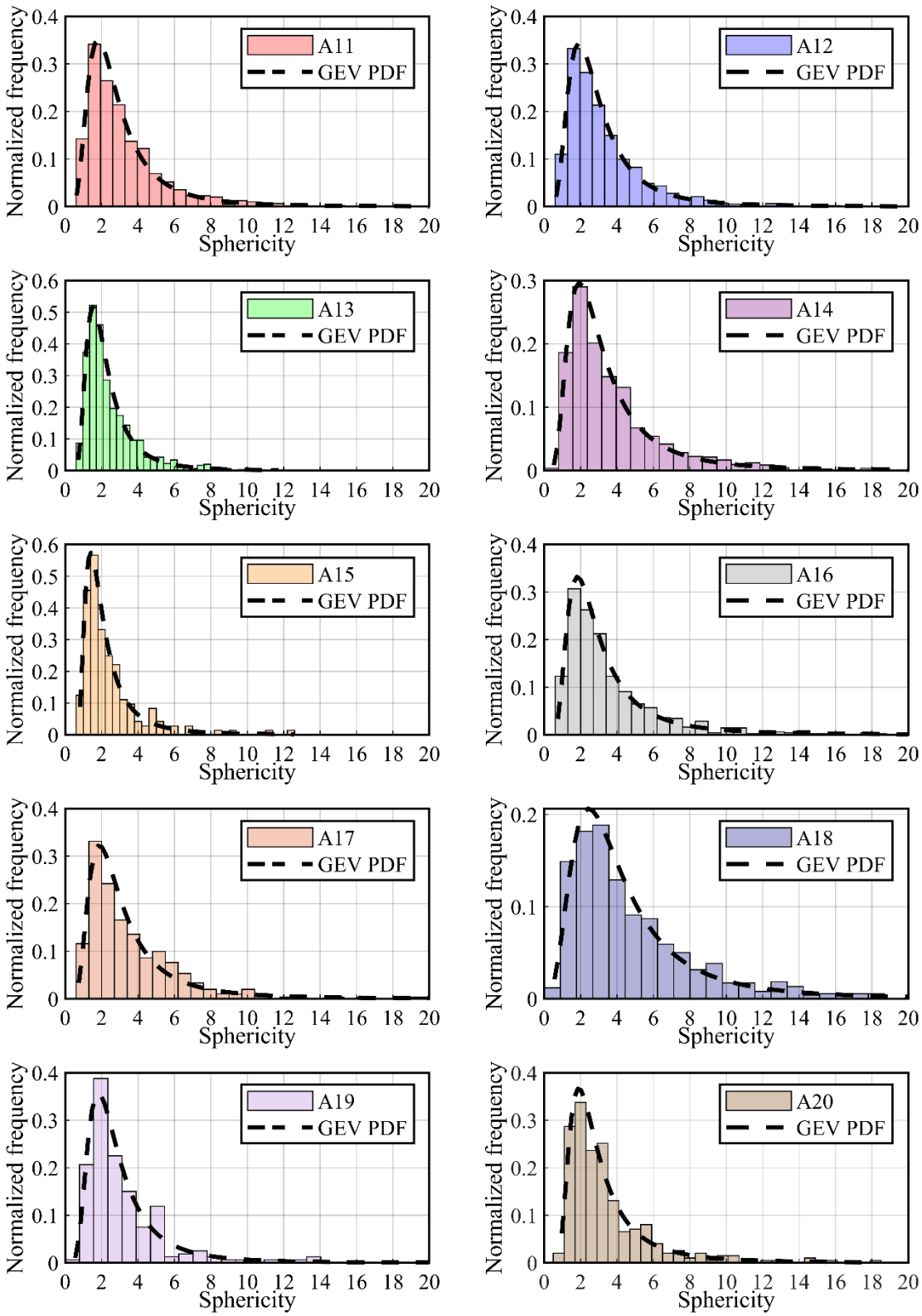
A11
GEV PDF
Normalized frequency
Sphericity
A12
GEV PDF
Normalized frequency
Sphericity
A13
GEV PDF
Normalized frequency
Sphericity
A14
GEV PDF
Normalized frequency
Sphericity
A15
GEV PDF
Normalized frequency
Sphericity
A16
GEV PDF
Normalized frequency
Sphericity
A17
GEV PDF
Normalized frequency
Sphericity
A18
GEV PDF
Normalized frequency
Sphericity
A19
GEV PDF
Normalized frequency
Sphericity
A20
GEV PDF
Normalized frequency
Sphericity

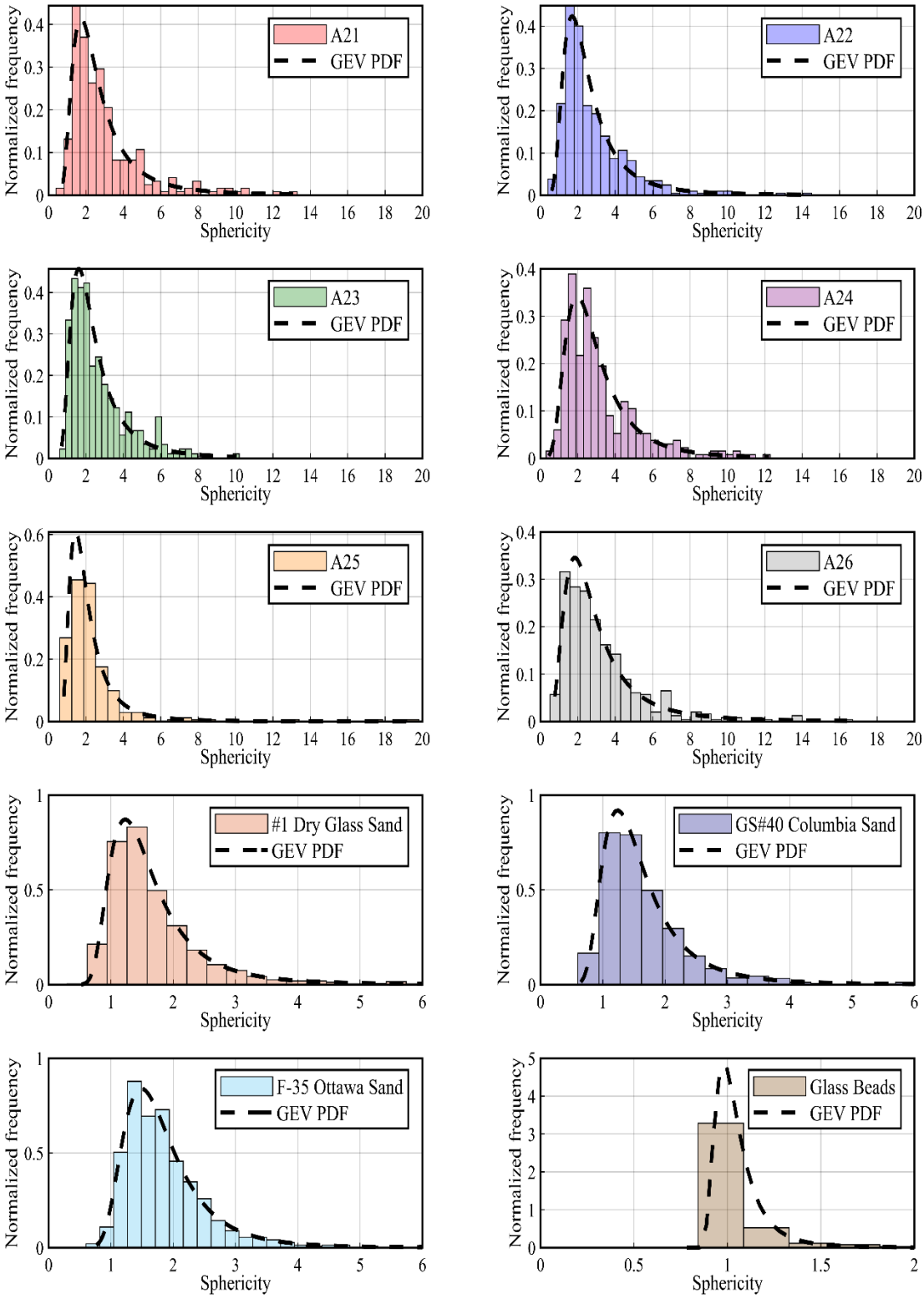

Figure 8-5. Frequency distribution of Sphericity and the generalized extreme value (GEV) distribution of fine and coarse angular materials.

Appendix (D-3): Frequency distribution of Roundness and the non-standardized Student's t-distribution of fine and coarse angular materials.

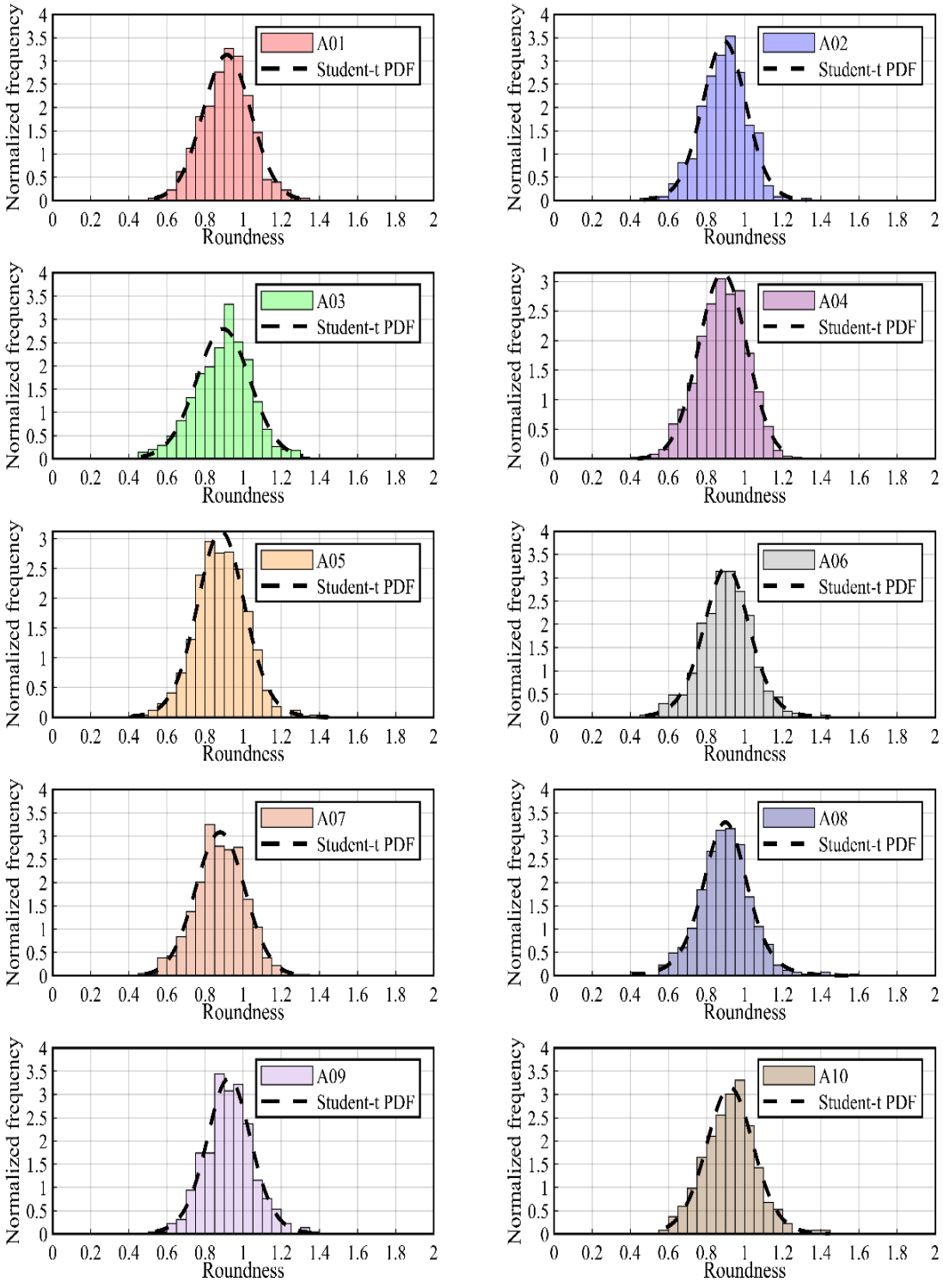

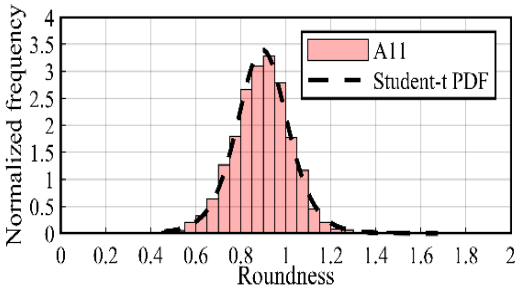
A11
Student-t PDF
Normalized frequency
Roundness

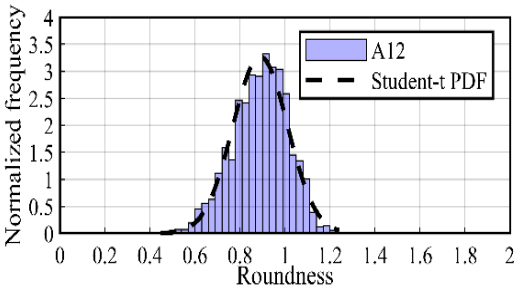
A12
Student-t PDF
Normalized frequency
Roundness

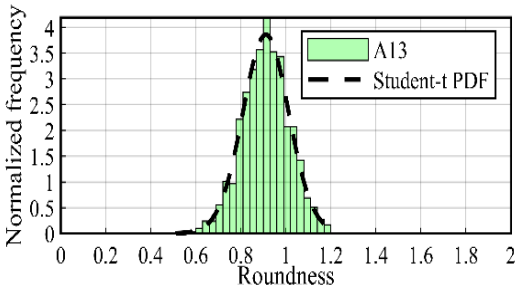
A13
Student-t PDF
Normalized frequency
Roundness

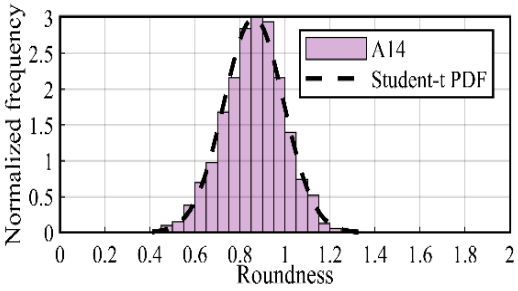
A14
Student-t PDF
Normalized frequency
Roundness

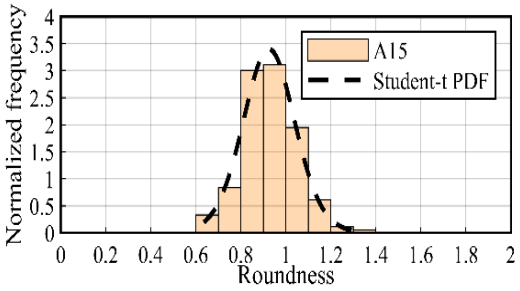
A15
Student-t PDF
Normalized frequency
Roundness

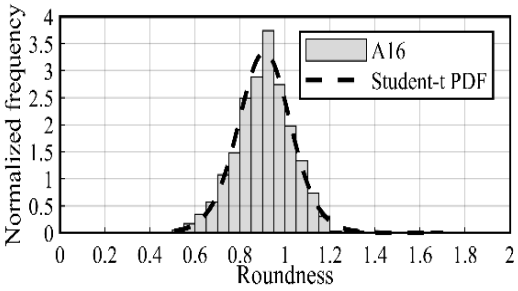
A16
Student-t PDF
Normalized frequency
Roundness

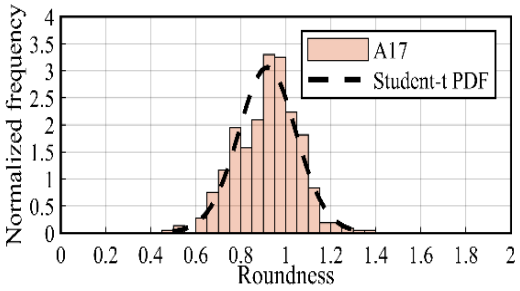
A17
Student-t PDF
Normalized frequency
Roundness

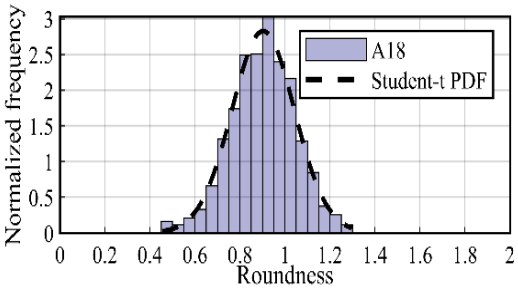
A18
Student-t PDF
Normalized frequency
Roundness

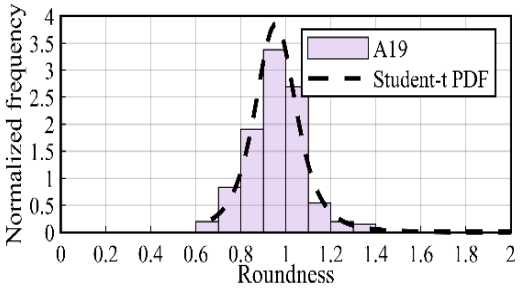
A19
Student-t PDF
Normalized frequency
Roundness

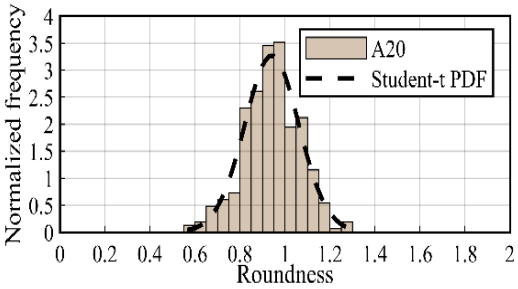
A20
Student-t PDF
Normalized frequency
Roundness

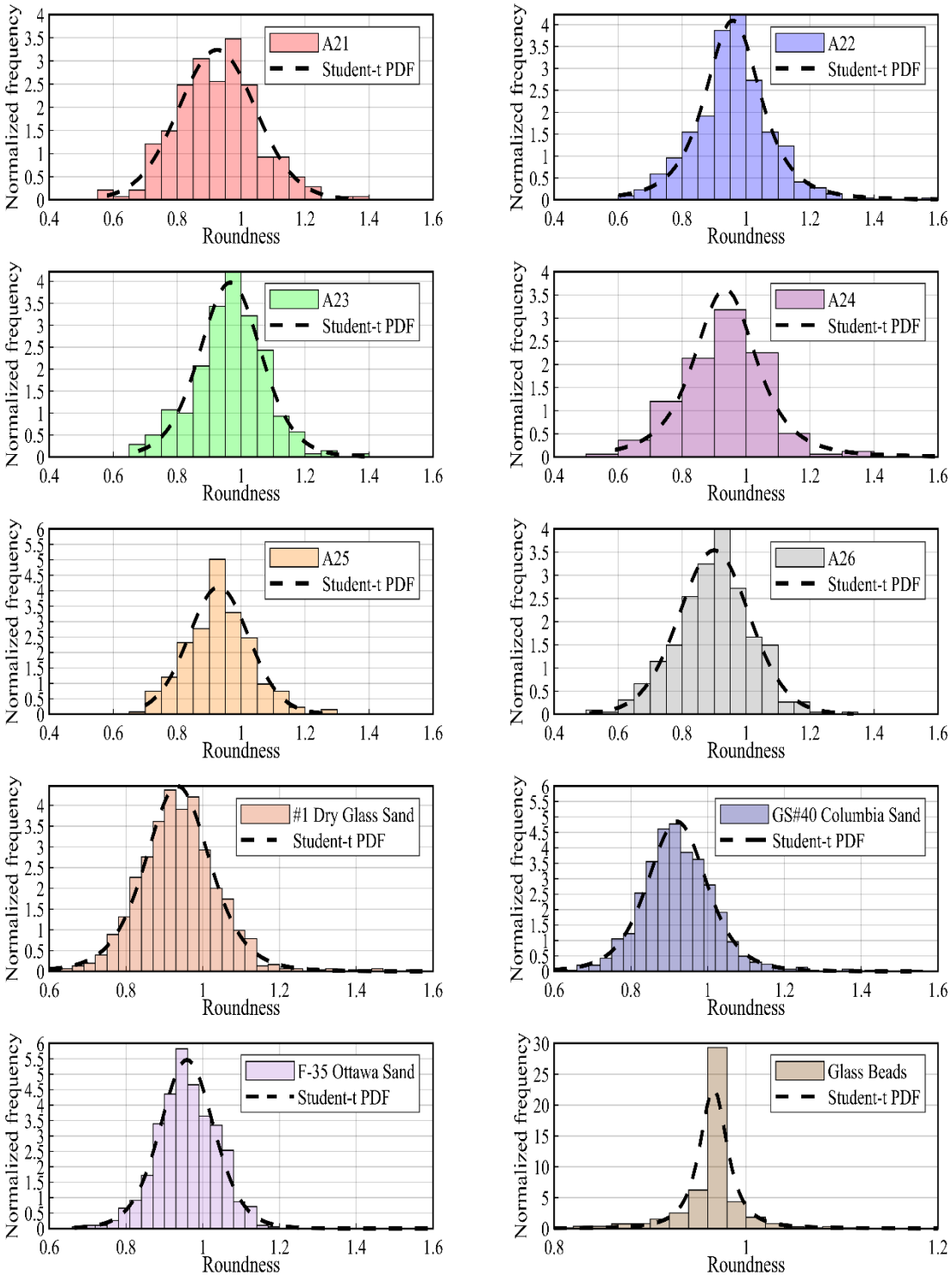

Figure 8-6. Frequency distribution of Roundness and the non-standardized Student's t-distribution of fine and coarse angular materials.

Appendix (D-4): Frequency distribution of Form and the Gamma distribution of fine and coarse angular materials.

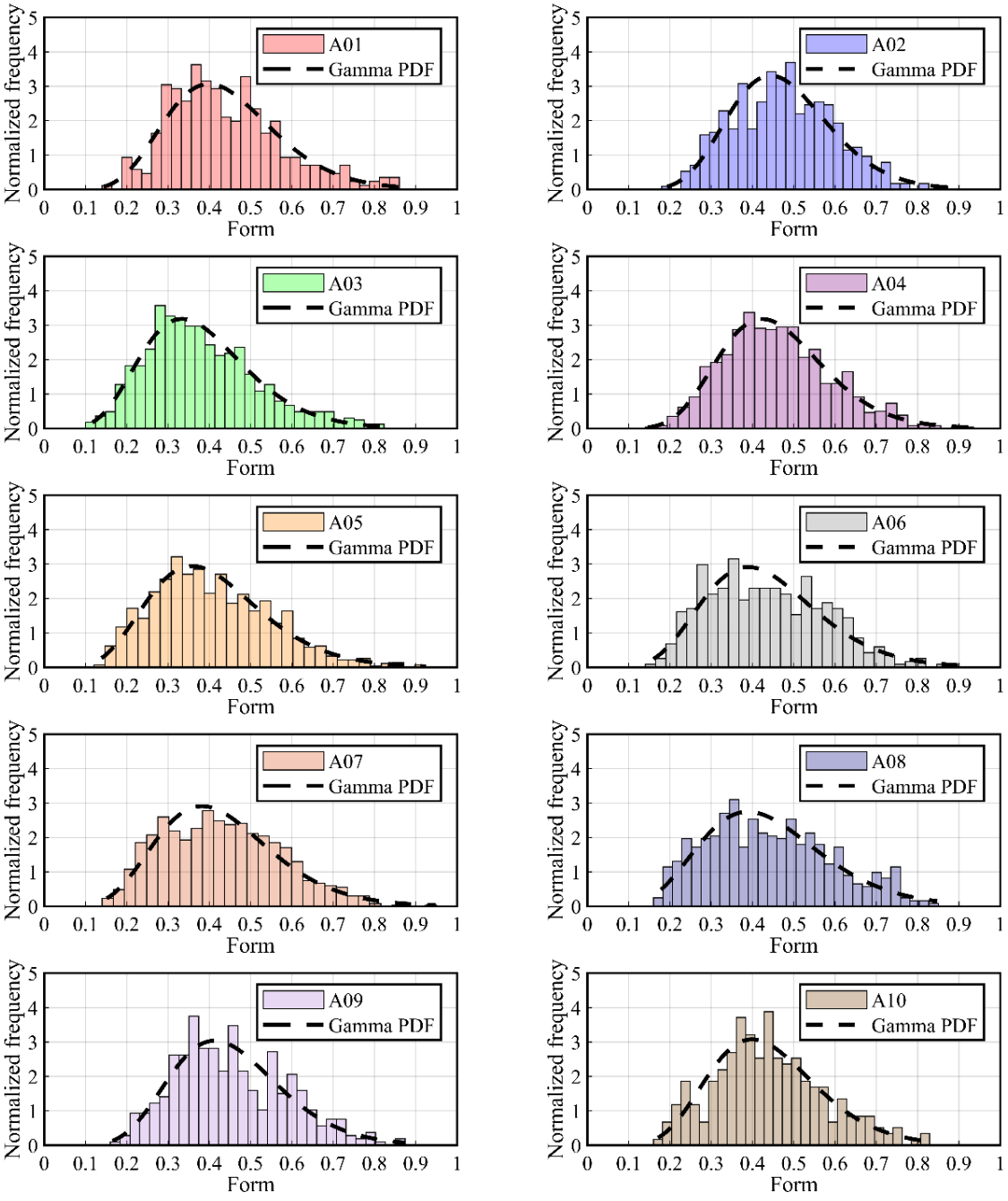

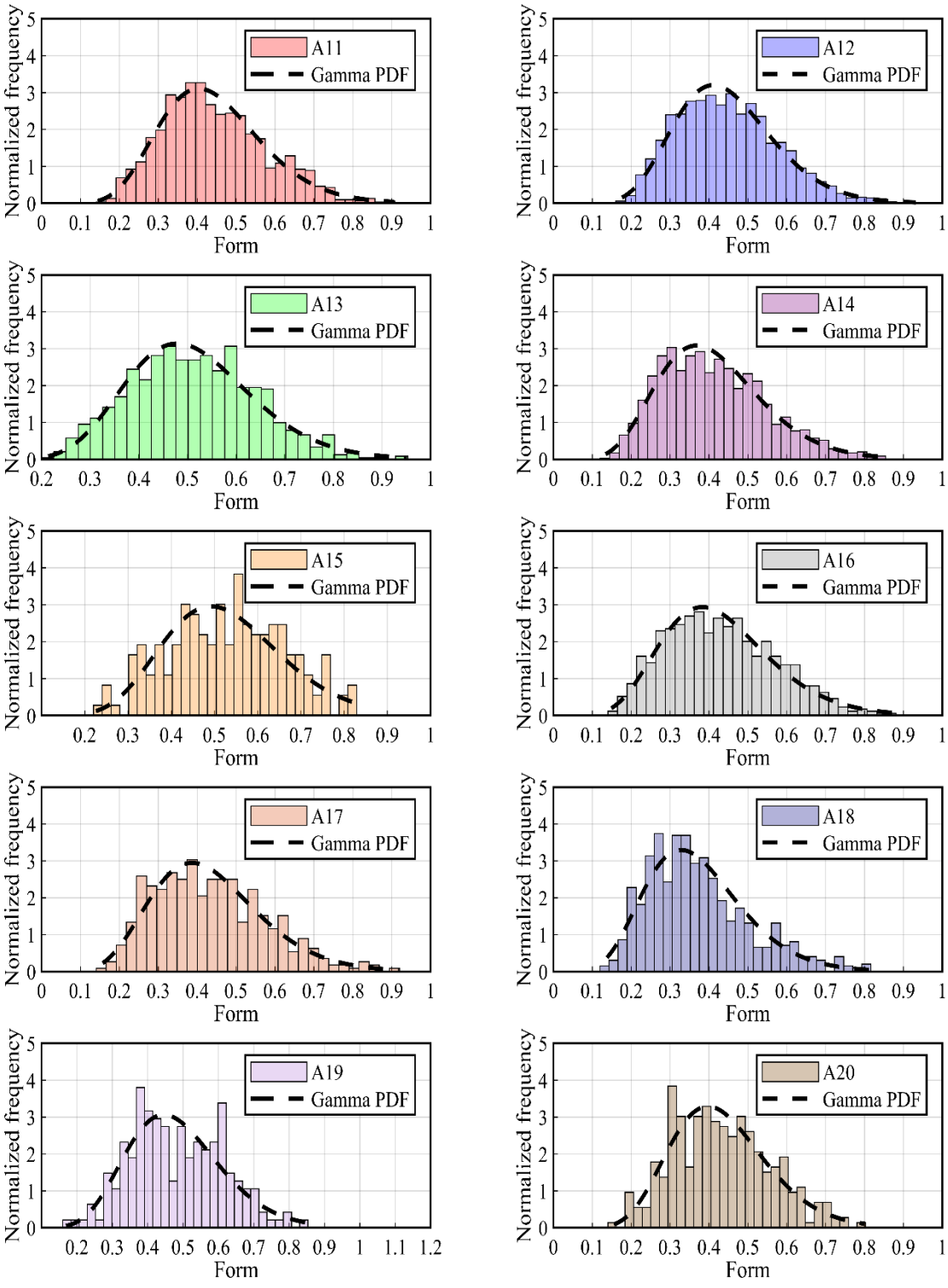
A11
Gamma PDF
Normalized frequency
Form
A12
Gamma PDF
Normalized frequency
Form
A13
Gamma PDF
Normalized frequency
Form
A14
Gamma PDF
Normalized frequency
Form
A15
Gamma PDF
Normalized frequency
Form
A16
Gamma PDF
Normalized frequency
Form
A17
Gamma PDF
Normalized frequency
Form
A18
Gamma PDF
Normalized frequency
Form
A19
Gamma PDF
Normalized frequency
Form
A20
Gamma PDF
Normalized frequency
Form

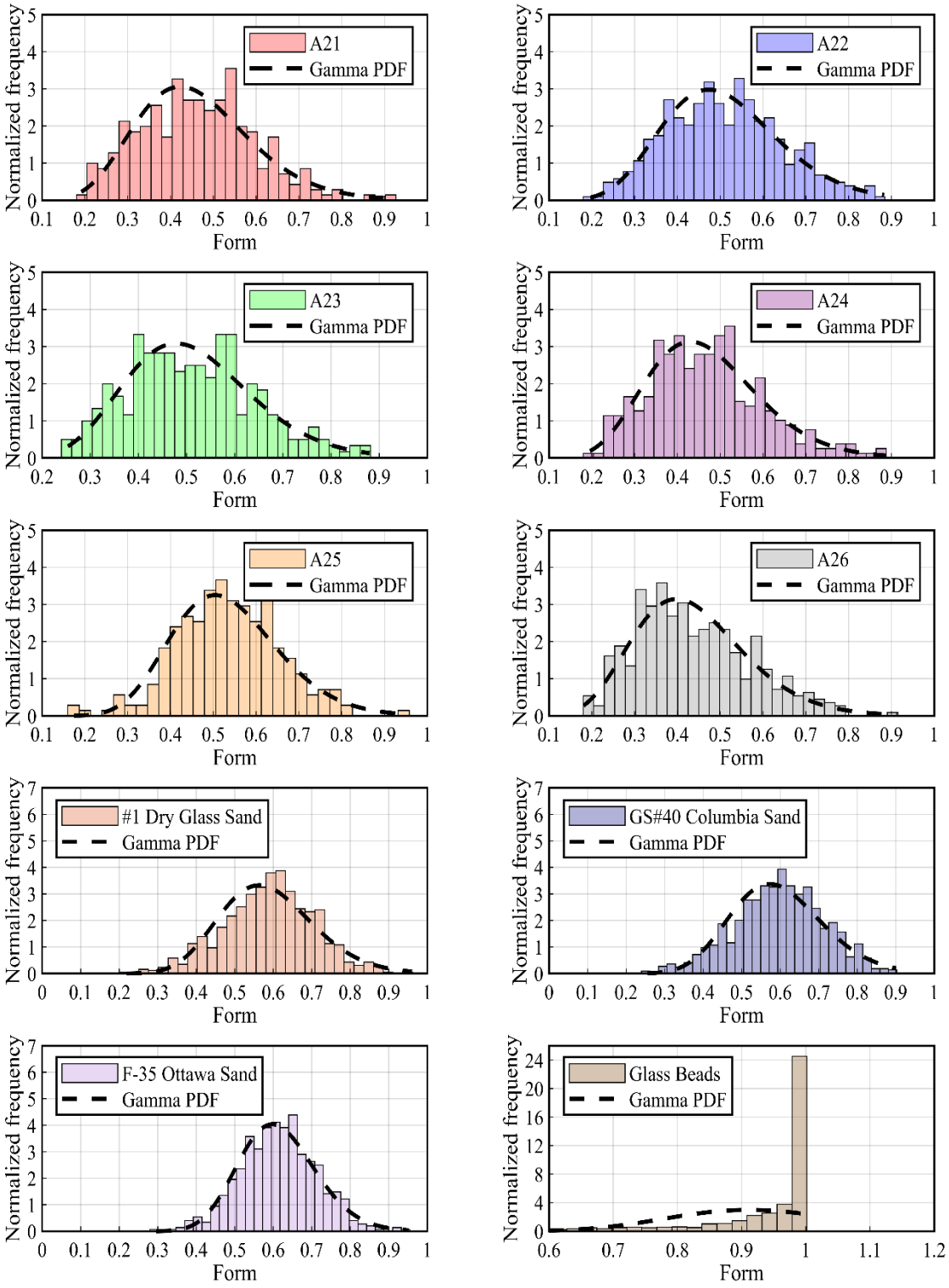

Figure 8-7. Frequency distribution of Form and the Gamma distribution of fine and coarse angular materials.

Appendix (E): Summary of measured ϕ_{cs}, ϕ_p, and ψ of OGA.

Material	γ_d (kN/m^3)	D_r	σ_N	ϕ_{cs}	ϕ_p	ψ
A01	15.97	0.80	35	61.6	68.8	15.2
			70	55.5	60.4	10.8
			105	53.1	57.2	8.6
			140	52.0	56.3	6.7
	14.93	0.30	35	61.3	N/A	N/A
			70	54.5	N/A	N/A
			105	50.0	N/A	N/A
			140	47.2	N/A	N/A
A02	16.27	0.80	35	59.7	68.1	14.4
			70	55.5	63.2	11.5
			105	53.1	57.6	8.4
			140	50.2	57.7	8.0
	15.10	0.30	35	54.5	N/A	N/A
			70	51.8	N/A	N/A
			105	50.4	N/A	N/A
			140	47.0	N/A	N/A
A03	16.55	0.80	35	66.9	71.2	13.6
			70	63.4	66.1	11.7
			105	59.9	62.9	8.9
			140	55.4	59.1	7.3
	15.36	0.30	35	56.1	N/A	N/A
			70	55.5	N/A	N/A
			105	54.8	N/A	N/A
			140	50.2	N/A	N/A
A04	15.96	0.80	35	62.1	68.4	12.8
			70	58.2	65.8	9.7
			105	56.9	60.9	7.7
			140	53.3	59.2	6.5
	14.64	0.30	35	60.4	N/A	N/A
			70	57.1	N/A	N/A
			105	56.7	N/A	N/A
			140	51.3	N/A	N/A

Material	γ_d (kN/m^3)	D_r	σ_N	ϕ_{cs}	ϕ_p	ψ
A05	16.55	0.80	35	58.9	67.5	14.3
			70	55.0	61.3	10.8
			105	52.7	58.8	8.1
			140	49.5	56.1	7.4
	15.24	0.30	35	52.7	N/A	N/A
			70	52.1	N/A	N/A
			105	46.3	N/A	N/A
			140	44.0	N/A	N/A
A06	15.85	0.80	35	66.4	72.5	14.3
			70	62.2	65.8	9.8
			105	56.9	62.5	8.5
			140	55.3	59.6	8.0
	14.52	0.30	35	56.1	N/A	N/A
			70	54.7	N/A	N/A
			105	53.1	N/A	N/A
			140	49.2	N/A	N/A
A07	15.47	0.80	35	60.9	67.6	12.5
			70	56.3	63.0	9.9
			105	53.1	56.8	6.7
			140	51.5	55.7	6.7
	14.23	0.30	35	54.2	N/A	N/A
			70	53.6	N/A	N/A
			105	50.0	N/A	N/A
			140	49.7	N/A	N/A
A08	15.81	0.80	35	59.3	67.9	14.7
			70	58.4	63.9	9.3
			105	53.1	59.6	7.7
			140	54.2	57.2	7.4
	14.62	0.30	35	58.4	N/A	N/A
			70	51.2	N/A	N/A
			105	51.1	N/A	N/A
			140	48.3	N/A	N/A

Material	γ_d (kN/m^3)	D_r	σ_N	ϕ_{cs}	ϕ_p	ψ
A09	15.48	0.80	35	61.3	70.8	15.9
			70	59.3	65.4	10.4
			105	58.0	62.8	8.6
			140	54.6	59.3	7.7
	14.39	0.30	35	57.5	N/A	N/A
			70	53.6	N/A	N/A
			105	53.1	N/A	N/A
			140	52.0	N/A	N/A
A10	15.20	0.80	35	62.8	70.2	14.7
			70	61.9	66.4	10.4
			105	56.2	63.2	8.9
			140	55.7	60.2	7.6
	14.26	0.30	35	61.3	N/A	N/A
			70	56.4	N/A	N/A
			105	53.9	N/A	N/A
			140	50.7	N/A	N/A
A11	15.54	0.80	35	55.0	70.3	15.0
			70	57.5	64.9	10.4
			105	55.2	59.6	7.2
			140	54.7	58.1	7.7
	14.37	0.30	35	56.6	N/A	N/A
			70	53.3	N/A	N/A
			105	52.3	N/A	N/A
			140	48.8	N/A	N/A
A12	16.49	0.80	35	62.1	70.5	13.4
			70	55.0	62.8	9.3
			105	56.1	60.1	7.8
			140	54.7	58.2	6.3
	15.14	0.30	35	58.0	N/A	N/A
			70	52.1	N/A	N/A
			105	53.1	N/A	N/A
			140	49.5	N/A	N/A

Material	γ_d (kN/m^3)	D_r	σ_N	ϕ_{cs}	ϕ_p	ψ
A13	15.41	0.80	35	59.7	70.2	15.0
			70	53.6	63.1	10.7
			105	56.2	59.8	8.9
			140	51.3	58.0	7.5
	14.35	0.30	35	55.5	N/A	N/A
			70	52.7	N/A	N/A
			105	53.1	N/A	N/A
			140	50.5	N/A	N/A
A14	16.13	0.80	35	55.5	64.9	11.5
			70	54.2	62.3	9.1
			105	53.9	58.5	7.2
			140	51.5	54.8	5.8
	14.88	0.30	35	56.6	N/A	N/A
			70	53.6	N/A	N/A
			105	47.4	N/A	N/A
			140	47.7	N/A	N/A
A15	15.87	0.80	35	60.2	69.5	13.3
			70	55.8	62.3	9.9
			105	53.9	61.7	9.4
			140	52.6	57.5	7.8
	14.85	0.30	35	57.1	N/A	N/A
			70	51.2	N/A	N/A
			105	51.1	N/A	N/A
			140	49.9	N/A	N/A
A16	14.99	0.80	35	57.5	68.6	13.0
			70	58.0	62.9	7.5
			105	52.9	57.3	6.6
			140	52.7	55.9	6.0
	13.82	0.30	35	57.1	N/A	N/A
			70	53.6	N/A	N/A
			105	49.7	N/A	N/A
			140	49.7	N/A	N/A

Material	γ_d (kN/m^3)	D_r	σ_N	ϕ_{cs}	ϕ_p	ψ
A17	14.69	0.80	35	66.4	73.0	14.8
			70	55.8	63.2	8.7
			105	56.9	60.3	7.2
			140	54.7	56.6	5.6
	13.63	0.30	35	58.4	N/A	N/A
			70	52.7	N/A	N/A
			105	50.9	N/A	N/A
			140	49.7	N/A	N/A
A18	14.69	0.80	35	62.8	69.5	14.2
			70	60.8	67.0	11.1
			105	56.2	59.4	7.2
			140	56.4	58.2	6.1
	13.41	0.30	35	57.5	N/A	N/A
			70	54.5	N/A	N/A
			105	51.7	N/A	N/A
			140	49.7	N/A	N/A
A19	14.08	0.80	35	57.5	69.2	14.7
			70	55.0	59.8	11.1
			105	53.1	58.7	9.6
			140	50.4	54.7	8.0
	13.23	0.30	35	55.0	N/A	N/A
			70	48.8	N/A	N/A
			105	48.8	N/A	N/A
			140	47.4	N/A	N/A
A20	15.31	0.80	35	61.3	68.8	12.8
			70	57.5	62.9	8.8
			105	56.2	59.8	5.9
			140	53.0	56.7	5.3
	14.09	0.30	35	56.1	N/A	N/A
			70	54.0	N/A	N/A
			105	52.7	N/A	N/A
			140	46.4	N/A	N/A

Material	γ_d (kN/m^3)	D_r	σ_N	ϕ_{cs}	ϕ_p	ψ
A21	14.92	0.80	35	60.9	71.4	14.4
			70	60.4	67.6	10.4
			105	57.4	62.5	8.4
			140	55.0	59.6	8.1
	13.86	0.30	35	60.6	N/A	N/A
			70	57.1	N/A	N/A
			105	53.7	N/A	N/A
			140	51.2	N/A	N/A
A22	15.03	0.80	35	56.1	63.9	13.7
			70	52.7	60.5	11.3
			105	53.1	56.0	8.2
			140	47.9	52.8	7.9
	14.21	0.30	35	49.5	N/A	N/A
			70	46.2	N/A	N/A
			105	45.3	N/A	N/A
			140	44.0	N/A	N/A
A23	14.01	0.80	35	55.0	67.0	15.4
			70	48.8	56.7	11.3
			105	48.8	55.2	9.2
			140	48.8	53.1	8.8
	12.98	0.30	35	51.5	N/A	N/A
			70	47.7	N/A	N/A
			105	47.8	N/A	N/A
			140	46.2	N/A	N/A
A24	14.65	0.80	35	60.6	67.8	14.7
			70	55.5	60.0	11.6
			105	54.1	58.8	9.2
			140	51.8	56.9	8.5
	13.88	0.30	35	52.1	N/A	N/A
			70	48.8	N/A	N/A
			105	47.6	N/A	N/A
			140	47.0	N/A	N/A

Material	γ_d (kN/m^3)	D_r	σ_N	ϕ_{cs}	ϕ_p	ψ
A25	15.18	0.80	35	64.1	72.4	15.3
			70	60.9	68.2	11.1
			105	59.7	64.9	8.5
			140	56.1	60.2	6.6
	14.12	0.30	35	60.2	N/A	N/A
			70	57.3	N/A	N/A
			105	53.1	N/A	N/A
			140	49.3	N/A	N/A
A26	15.54	0.80	35	60.9	70.9	13.3
			70	60.4	65.5	8.9
			105	56.2	61.5	8.0
			140	53.9	57.3	7.1
	14.39	0.30	35	58.4	N/A	N/A
			70	52.4	N/A	N/A
			105	51.3	N/A	N/A
			140	47.0	N/A	N/A

Appendix (F): Summary of measured ϕ_{cs}, ϕ_p, and ψ of fine granular materials (Lee 2017).

Material	γ_d (kN/m^3)	D_r	σ_N	ϕ_{cs}	ϕ_p	ψ
#1 Dry Glass Sand	13.50	0.07	15	36.0	N/A	2.3
	13.55	0.09	50	36.3	N/A	2.3
	13.51	0.07	100	34.2	N/A	1.8
	13.55	0.09	400	31.2	N/A	1.8
	14.62	0.53	15	31.5	32.5	11.5
	14.57	0.51	50	31.3	32.5	10.0
	14.60	0.52	100	29.1	31.8	9.1
	14.64	0.54	400	28.7	30.9	8.4
	15.65	0.89	15	36.5	41.6	18.1
	15.74	0.92	50	36.0	39.9	16.6
	15.73	0.92	100	35.0	38.0	16.0
	15.70	0.91	400	30.2	38.5	15.4
GS#40 Columbia Sand	13.52	0.08	15	35.2	N/A	1.7
	13.55	0.09	50	34.0	N/A	1.6
	13.56	0.10	100	33.6	N/A	1.5
	13.52	0.08	400	31.7	N/A	1.0
	14.74	0.60	15	34.4	34.9	11.4
	14.72	0.60	50	33.1	33.5	9.5
	14.75	0.61	100	30.6	32.0	9.4
	14.72	0.60	400	28.9	32.8	8.8
	15.65	0.94	15	36.8	42.2	17.3
	15.66	0.95	50	33.8	42.2	16.6
	15.67	0.95	100	32.2	37.8	16.6
	15.66	0.95	400	31.3	37.7	16.0

Material	γ_d (kN/m^3)	D_r	σ_N	ϕ_{cs}	ϕ_p	ψ
F-35 Ottawa Sand	15.00	0.11	15	34.7	N/A	2.8
	15.00	0.11	50	32.6	N/A	2.9
	15.01	0.12	100	32.6	N/A	2.3
	14.99	0.11	400	30.9	N/A	2.3
	16.10	0.55	15	32.9	32.9	13.4
	16.09	0.54	50	31.0	33.4	12.2
	16.07	0.54	100	30.0	32.5	11.1
	16.11	0.55	400	28.1	32.2	8.8
	17.23	0.93	15	36.1	40.0	19.1
	17.25	0.94	50	32.8	39.8	19.6
	17.19	0.92	100	29.4	38.0	18.9
	17.22	0.93	400	29.2	38.2	17.5
Glass Beads	14.53	0.34	15	26.9	N/A	3.6
	14.47	0.31	50	25.9	N/A	2.8
	14.51	0.33	100	23.5	N/A	2.1
	14.50	0.32	400	23.4	N/A	2.2
	15.17	0.65	15	25.0	25.0	12.9
	15.22	0.67	50	23.8	26.6	10.8
	15.16	0.64	100	22.1	26.1	10.6
	15.17	0.65	400	21.6	26.2	8.6
	15.89	0.96	15	26.0	32.9	19.3
	15.91	0.97	50	25.6	32.9	18.6
	15.83	0.94	100	24.7	32.8	17.7
	15.82	0.93	400	24.5	32.2	15.1